Imaging magnesium-based implants and their biological surroundings

Dissertation

to obtain the academic degree

DOCTOR OF ENGINEERING (DR.-ING.)

from Christian-Albrechts-Universität zu Kiel

submitted by

JONATHAN W. ESPIRITU
of Glendale, United States of America

November 2024

Doctoral Researcher	Jonathan W. Espiritu
Supervisor	Prof. Dr. Regine Willumeit-Römer
Reviewer	Prof. Dr. Jan-Bernd Hoevener
Date of Oral Examination	April 16, 2025

"Luck is what happens when preparation meets opportunity." – Seneca

Abstract

The increasing prevalence of bone-related injuries and the ageing geriatric population continue to drive the orthopaedic implant market. This cumulative thesis presents three interconnected investigations that address critical aspects of biodegradable magnesium (Mg)-based orthopaedic implants: their impact on bone remodelling, magnetic resonance imaging (MRI) artefacts, and radio-frequency (RF)-induced heating. Additionally, a comprehensive literature review is presented on the behaviour of Mg-based alloys in MRI. These investigations contribute to our understanding of the behaviour and implications of Mg-based implants in clinical practice.

The first study explores the relationship between biodegradable implant materials and bone health, focusing on the lacuno-canalicular network (LCN) and its integral role in bone remodelling. The influence of plasma electrolytic oxidation (PEO) surface treatment on LCN morphology around WE43 screws implanted into sheep bone is investigated. Synchrotron-based transmission X-ray microscopy is utilised to characterise LCN differences between untreated and PEO-treated implants. Findings indicate that PEO-coated WE43 screws induce healthier lacunar shapes within the LCN, while uncoated materials promote a more connected LCN, potentially better prepared for bone trauma.

The second investigation addresses the issue of image artefacts caused by Mg-based implants in MRI. The study involves *in vitro*, *ex vivo*, and clinical assessments of Mg-based implants for various magnetic field strengths, with a focus on quantifying metallic artefact behaviour. Results demonstrate that as the Mg-based implant degrades, metallic artefact production decreases, particularly when the imaging plane is perpendicular to the implant axis. Compared to titanium equivalents, Mg-based implants consistently produce lower metallic artefacts, supporting their potential for post-operative MRI monitoring.

The final investigation explores the effect of the degradation layer on RF-induced heating of Mg-based orthopaedic implants. WE43 compression screws were subjected to *in vitro* degradation, and temperature measurements were used to quantify implant heating during MRI. Results indicate that the highest risk of implant RF heating occurs before degradation, with heating decreasing as the degradation layer forms. Importantly, no statistical differences in heating are observed between non-degraded WE43 material and commercial titanium equivalents. The findings highlight the need for industry standards to consider biodegradable materials in MRI safety assessments.

In conclusion, this cumulative thesis provides a comprehensive exploration of Mg-based orthopaedic implants, encompassing their influence on bone remodelling, MRI image quality, and patient safety. The results advance our knowledge of these implants' behaviour and their potential for enhancing patient care in orthopaedic surgery, imaging, and post-operative monitoring.

Zusammenfassung

Die zunehmende Prävalenz von Knochenverletzungen, sowie die zunehmend älter werdende Bevölkerung treiben weiterhin den Markt für orthopädische Implantate an.

Diese Studie präsentiert drei miteinander verbundene Untersuchungen, welche sich mit kritischen Aspekten von biologisch abbaubaren, magnesiumbasierten orthopädischen Implantaten befasst:

Die möglichen Auswirkungen der Implantate auf die Knochenremodellierung, die Artefakte in der Magnetresonanztomographie (MRT) und zuletzt die induzierte Erwärmung durch Hochfrequenz des MRT.

Zusätzlich wurde eine umfassende Literaturübersicht über das Verhalten von Mg-basierten Legierungen in der MRT vorgestellt. Diese Untersuchungen tragen zu unserem Verständnis des Verhaltens, sowie der Auswirkungen von Mg-basierten Implantaten in der klinischen Praxis bei.

Die erste Studie untersuchte die Beziehung zwischen biologisch abbaubaren Implantatmaterialien und der Knochengesundheit. Hierbei lag der Fokus auf dem lakuno-kanalikulären Netzwerk (LCN) und seiner integralen Rolle bei der Knochenumbildung. Es wurden die Auswirkungen der Plasmabehandlung durch elektrolytische Oxidation (PEO) auf die Morphologie des LCN in Schafknochen implantierter WE43-Schrauben untersucht. Zur Charakterisierung der LCN-Unterschiede zwischen unbehandelten und PEO-behandelten Implantaten wurde synchrotronbasierte Röntgenmikroskopie eingesetzt. Die Ergebnisse deuten darauf hin, dass PEO-beschichtete WE43-Schrauben gesündere lakunare Formen innerhalb des LCN induzieren, während unbeschichtete Materialien ein stärker vernetztes LCN fördern, das möglicherweise besser auf Knochenverletzungen vorbereitet ist.

Die zweite Untersuchung befasste sich mit dem Problem von MRT-Artefakten, die durch Mg-basierte Implantate verursacht werden. Die Studie beinhaltet in vitro, ex vivo und klinische Bewertungen von Mg-basierten Implantaten für verschiedene Magnetfeldstärken, wobei der Fokus auf der Quantifizierung des metallischen Artefaktverhaltens lag. Die Ergebnisse zeigten, dass mit dem Abbau des Mg-basierten Implantats die Produktion von metallischen Artefakten abnahm, insbesondere wenn die Bildebene senkrecht zur Implantatachse lag. Im Vergleich zu Titanäquivalenten erzeugen Mg-basierte Implantate durchweg geringere metallische Artefakte, was ihr Potenzial für die postoperative MRT-Überwachung unterstützt.

Die abschließende Untersuchung analysierte den Einfluss der Abbauschicht auf die durch Hochfrequenz induzierte Erwärmung von Mg-basierten orthopädischen Implantaten. WE43-Kompressionsschrauben wurden einer in vitro Degradation unterzogen und Temperaturmessungen wurden verwendet um die Implantaterwärmung während des MRTs zu untersuchen. Das höchste Risiko einer Implantaterwärmung durch Hochfrequenz trat vor der Degradation auf, wobei die Erwärmung abnahm, als sich die Abbauschicht bildete. Wichtig ist, dass keine statistischen Unter-

schiede in der Erwärmung zwischen nicht abgebautem WE43-Material und kommerziellen Titanäquivalenten beobachtet wurden. Die Ergebnisse unterstreichen die Notwendigkeit, dass Industrienormen biologisch abbaubarer Materialien in MRT-Sicherheitsbewertungen zu berücksichtigen sind.

Zusammenfassend bietet diese Studie eine umfassende Untersuchung von Mg-basierten orthopädischen Implantaten, einschließlich ihrer Auswirkungen auf die Knochenumbildung, die MRT-Bildqualität und die Patientensicherheit. Die Ergebnisse erweitern unser Wissen über das Verhalten dieser Implantate und ihr Potenzial zur Verbesserung der Patientenversorgung in der orthopädischen Chirurgie, Bildgebung und postoperativen Überwachung.

Contents

List of Figures

Chapter 1

Introduction

In the realm of modern medicine, the development and implementation of orthopaedic implants have marked significant milestones in enhancing the quality of life for individuals suffering from musculoskeletal disorders and injuries [1]. These remarkable innovations have not only alleviated pain but have also restored mobility and functionality, allowing patients to regain their independence and lead fulfilling lives. In the pursuit of continually improving these life-changing interventions, the intersection of biomaterials science, medical imaging technologies, and translational research has emerged for groundbreaking advancements [2]. This dissertation examines the intricacies of orthopaedic implants, with a particular focus on magnesium (Mg)-based implants, their surface modifications, and the pivotal role played by medical imaging technologies in their development and evaluation. In this introductory chapter, we will lay the foundation for the forthcoming chapters, offering preliminary insights into the various aspects of biomaterials, Mg, bone biology, and medical imaging techniques that collectively contribute to the paradigm shift in orthopaedic implant technology.

Orthopaedic implants have revolutionised the treatment of a wide range of musculoskeletal conditions, from fractures and degenerative joint diseases to complex deformities. These implants, ranging from metallic plates [3] and screws [4] to artificial joints [5] and spinal implants [6], have not only improved patient outcomes, but have also extended the potential for active and pain-free living. However, the need for better surgical outcomes, reduced complications, and increased patient satisfaction continues to drive research in this field.

In recent years, a novel class of orthopaedic implants based on Mg-based alloys has emerged, promising to be a step change in treatment [7]. Unlike traditional implants that are permanent fixtures in the body, Mg-based implants have the remarkable property of biodegradability, gradually dissolving over time, being replaced with regenerated tissue [8]. This property holds great promise for minimising long-term complications and avoiding the need for secondary implant removal surgeries.

The successful development and evaluation of orthopaedic implants heavily rely on advanced medical imaging technologies. X-ray imaging provides essential insights into implant positioning and structural integrity, while magnetic resonance imaging (MRI) offers a more nuanced understanding of bone morphology and soft tissue responses. In the chapters to come, we conduct a comprehensive investigation into the applications and advancements in these imaging modalities, hinting at their indispensable role in medical implant evaluation.

Bridging the gap between laboratory research and clinical application is a pivotal step in the evolution of orthopaedic implants. Translational research encompasses the entire journey, from conceptualisation and preclinical testing to regulatory approvals and widespread clinical use. This dissertation will explore the translational aspects of medical device development, providing insight on the processes involved in bringing innovative implant technologies from bench to bedside.

Within the framework of this dissertation, a range of imaging technologies are systematically employed to examine the interplay between bone and implants, alongside the translational aspects pertinent to the advancement of medical device development. Chapter 3 establishes the theoretical foundation, describing the role of Mg as a biomaterial and key aspects of bone biology. Furthermore, we explore the domain of imaging techniques, offering an in-depth exploration in Chapter 4. Additionally, Chapter 5 presents an exhaustive literature review specifically focusing on Mg-based implants within the context of MRI.

Subsequently, this dissertation sequentially presents the publications from the research undertaken during this doctoral investigation. These publications are organised to delineate a coherent trajectory, commencing from fundamental investigations conducted at the "scientific bench-side" and culminating in experiments aimed at facilitating the clinical integration of medical devices. Chapter 6, for instance, employs innovative imaging techniques to investigate bone remodelling surrounding both uncoated and surface-treated WE43 implants. As we traverse from experimental science toward patient-centred care, Chapter 7 evaluates the behaviour of implant materials within the realm of MRI—a domain where the quality of MR images is profoundly influenced by the interaction of implant materials. Transitioning towards the domain of clinical utility, Chapter 8 in Part II provides valuable insights into ensuring patient safety during post-operative care.

Lastly, a comprehensive synthesis of all findings is offered. The findings are accompanied by a forward-looking perspective on the future developments pertaining to Mg-based implants and the continued utilisation of advanced imaging technologies in this field of research. Through the exploration of these chapters, we aim to illuminate the evolving landscape of orthopaedic implants and contribute to the collective endeavour of enhancing the quality of life for countless patients worldwide.

Chapter 2

Motivation and Objectives

In this dissertation, advanced imaging methodologies are utilised to investigate the intricacies associated with the examination of biodegradable materials in the context of fundamental bench-side research, aimed at addressing the challenges encountered when transitioning a medical device from laboratory settings to clinical applications. Moreover, the utilisation of plasma electrolytic oxidation (PEO) surface treatments has been demonstrated to mitigate the rapid degradation tendencies exhibited by magnesium (Mg) through the inhibition of corrosion rates. It is noteworthy, however, that there is currently little documented research pertaining to the impact of biodegradable materials on the lacunar-canaliculi network (LCN) within bone, particularly when employing non-destructive three-dimensional (3D) imaging techniques such as synchrotron radiation-based transmission X-ray microscopy (TXM).

Additionally, the utilisation of Mg-based implants introduces certain challenges in the realm of magnetic resonance imaging (MRI), including the generation of image artefacts and the potential elevation of local tissue temperatures. Nevertheless, it is imperative to acknowledge that the influence of Mg degradation on image quality, specifically in terms of metallic artefacts in MRI examinations and the induction of local tissue heating, remains an under-explored area.

Consequently, the primary objective of this dissertation is to harness cutting-edge imaging technologies to gain insight into the biological environment surrounding Mg-based implants. Furthermore, it seeks to evaluate these materials in accordance with prevailing industry standards, with the ultimate goal of enhancing the performance of future medical devices. To this end, the research aims to address the following key questions:

1. What is the influence of PEO-coated Mg-based screws on the surrounding bone structure, utilising synchrotron radiation-based TXM?

2. Is it possible to quantify the production of metallic artefacts by Mg-based implants during MRI procedures? How does the performance of Mg-based implants compare to their titanium counterparts in this context?

3. How does the degradation layer of Mg-based implants influence the RF-induced heating profiles of the implant during MRI examinations?

Having explored the motivations behind this research, we now turn our attention to the foundational context that inform the dissertation.

Chapter 3

Background Part I: Magnesium and Bone

This chapter serves as an introduction to biomaterials, describing biodegradable materials, with a special focus on Mg. We discuss material surface treatments and their pivotal role in enhancing the biocompatibility and performance of biomaterials. Moreover, this chapter offers a basic understanding of bone biology as it interfaces with the world of biomaterials. The synergy between these topics serves as a foundational framework for our subsequent discussions, fostering insights into the development, applications, and advancements of biomaterial science and its implications in the field of biomedical engineering and healthcare.

3.1 Biomaterials

A biomaterial is any none-drug substance, synthetic or natural, that can be used as a system or part of a system to treat, augment, or replace a tissue, organ, or function of the human body [9]. To maintain patient safety, it is necessary to assess the biocompatibility of the implant or biomaterial. Biocompatibility is the ability of a material to perform with an appropriate host response in a specific application [10]. It involves the effects of the material on the host and the effects of the host on the material.

In terms of the effects of implants on hosts, responses can be observed at the local and systemic level. Locally, blood-material interactions (protein adsorption, coagulation, fibrinolysis, etc.) [11], infection [12], carcinogenesis, [13], embolisation [14], and hypersensitivity [15] may occur. While the biomaterial may impact the physiological environment of the human body, the human body itself may affect the biomaterial simultaneously. Physical and mechanical effects in the form of abrasive wear [16] and fatigue [17] are applied by physical activity of the host. Biological effects such as enzymatic degradation [18] and calcification [19] from tissues also occur. These responses need to be analysed to ensure the absence of carcinogenicity, immunogenicity, toxicity, and teratogenicity.

Popular biomaterials used today include ceramics, cobalt-chromium alloys, stainless steel, titanium alloys, and polymers [20, 21]. Medical implants made of these materials have been applied in the neural [22], sensory, and spinal environments of the human body [23]. Moreover, biomaterials are utilised in organ stimulation devices [24], cosmetics industry [25], and dental applications [26].

Biomaterials can be separated into the following categories: bioinert and bioactive. Bioinert materials resist the adhesion of proteins and cells (such as contact lenses). In contrast, bioactive materials promote the adhesion of proteins and cells. Biomaterials can similarly be classified depending on the carbon content of the material as organic or inorganic. Moreover, materials can be classified as metals, ceramics, polymers, and composites (Figure 3.1).

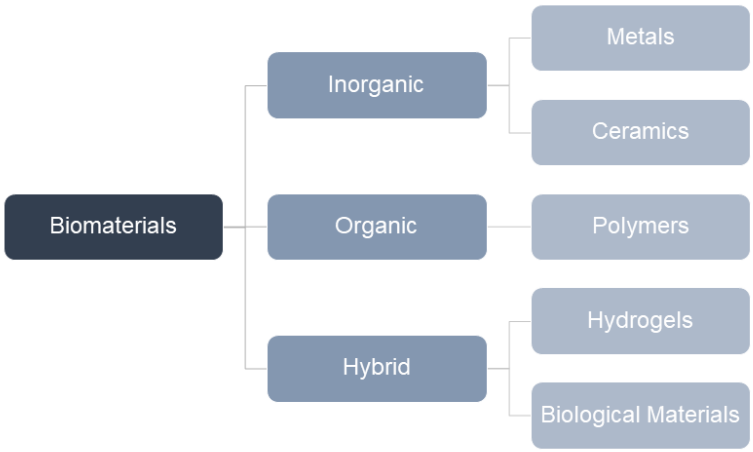

Figure 3.1: Breakdown chart of biomaterial classification.

3.2 Biodegradable Materials

Permanent metallic implants such as stainless steel, cobalt-chromium, and titanium are frequently removed after healing of the injury to prevent various side effects: bone resorption caused by stress shielding [27] and microbial implant infections [28]. Additionally, permanent implants fail to adapt to rapid growth in children and adolescents. The requirement of secondary removal surgeries due to potential mechanical implant failure, rejection, migration, or other complications do not only increase infection risk but also brings upon substantial costs to patients and hospitals. To solve this, biodegradable materials provide an alternative solution to permanent implants.

Biodegradable materials must not only meet general biomaterial requirements but must also meet requirements based on degradation capability. An ideal biodegradable material will meet the requirements of a biomaterial and absorb appropriately into the body once function is no longer required. For example: a vascular stent requires to be active for approximately six to twelve months to ensure arterial vessel remodelling [29], while an orthopaedic screw used to treat a fracture requires approximately 18 days for bone healing to begin [30]. Consequently, controlling the degradation rate is one of the largest issues faced when creating these materials.

Examples of biodegradable materials currently researched for load-bearing applications include organic polymers, iron, and zinc-based materials [31]. Though organic polymers have an adjustable degradation speed and inherent flexible characteristics, they have shown to cause inflammatory responses [32] and are too weak for weight-bearing applications. Additionally, imaging issues arise since pure polymers

are X-ray transparent, making it difficult for viewing. Iron-based materials maintain higher strength than polymers. However, iron-based implant materials degrade too slowly, requiring a longer duration for complete absorption [33]. The degradation time of iron-based implants with a diameter of 5 mm have been reported to take up to 5 years for complete resorption [34]. Negative biological effects such as the accumulation of inflammatory iron hydroxide particles have been found in various tissues [35]. Zinc-based materials have shown to have non-inflammatory effects but have overly slow degradation periods and sub-optimal strength [36]. One material gaining interest for orthopaedic applications is Mg.

3.2.1 Magnesium

Already found in abundance in the body, Mg serves as a co-factor in over 300 enzyme systems that regulate various biochemical reactions. A few reactions in which Mg facilitates is the regulation of blood pressure and glucose control, muscle and nerve function, and protein synthesis [37, 38, 39]. Additionally, Mg is required for energy production within the body. Mg promotes bone structural development and is required for DNA and RNA synthesis. At the cellular level, Mg is needed in the active transport of calcium and potassium ions across the cell membrane. The transport of these ions is important to nerve impulse conduction, muscle contraction, and maintaining normal hearth rhythm [38]. Approximately 25 grams of Mg can be found in the adult body, 50 to 60 % of which is stored in bones [40]. The majority of the remainder is found in soft tissue, while less than 1 % (0.75-0.95 mmol/L) of Mg is stored in our blood [41]. Mg homeostasis is mainly controlled by the kidney, excreting about 120 mg of Mg via urine daily [38]. Urinary output is increased when Mg levels in the blood are high [37]. With Mg being a vital element used in our body, how can we utilise it as a biomaterial?

The use of Mg as a biomaterial dates back to the 19th century when Dr. Edward C. Huse applied pure Mg as wire ligatures in three patient surgeries [42]. In 1878, Huse successfully prevented vessel bleeding during a radial artery and varicocele surgeries using Mg threading. The physician observed that Mg degraded slower *in vivo* than *in vitro* and was dependent on wire size. Soon after, Austrian physician Erwin Payr began implementing Mg-based implants in various clinical applications in 1892 [43]. From his work, Payr suggested that corrosion of the material was caused by water content found in tissue, salts found in blood, and chemical cell processes. This work was then extended into further animal and clinical investigations by the Belgian orthopaedist Albin Lambotte starting in 1906 [44]. From this point onward, Mg alloys were introduced into orthopaedic and traumatic surgery due to their good biocompatibility [43]. However, growth in the research and application of Mg began to slow when rapid degradation and large amounts of hydrogen accumulation in tissue began to be noticed.

In terms of reactivity with the human body, Mg demonstrates high biocompatibility. The effect of Mg^{2+} ion concentration on stem cells must be considered when evaluating Mg-based alloys for bone implant applications. Osteoblasts, which differentiate from stem cells, serve as the building blocks for new bone formation. A Mg^{2+} ion deficiency has been associated with altered osteoblast functions resulting in deficient bone formation [45]. With the aid of imaging technologies, successful bone development around Mg implants have been determined in many animal experiments.

Osseous formation has been exhibited around the implantation of a pure Mg pin into the distal femur of rats as described by Zhang et al. [46]. In terms of human applications, Yang et al. investigated the indirect effects of Mg-based alloys on human bone marrow-derived stromal cells. Results from their study revealed that concentrations of Mg less than 10 mM did not inhibit the viability and osteogenic differentiation of the stromal cells [47].

However, there are certain disadvantages of Mg that must be addressed to successfully implement the material in practice. Three main drawbacks of Mg include low elastic modulus, rapid degradation, and high hydrogen evolution [48]. The relatively lower elastic modulus of Mg compared to traditional materials may be beneficial in preventing stress shielding [49] but may result in potential mechanical distortion under high loads [50]. Rapid degradation of the implant may release Mg-alloy components such as Zn [51] at a fast rate that may be poisonous at large amounts. Moreover, the rapid degradation of Mg implants results in a loss of mechanical integrity as well [52]. Accumulation of gas or solid corrosion products may exert pressure on surrounding tissue and ultimately result in implant failure prior to proper healing time [53]. Unfortunately, this corrosion is inherent to Mg and deems to be one of the most difficult challenges.

The corrosive behaviour of Mg in an aqueous environment like the human body is an electrochemical process. With a negative equilibrium potential E_0 of -2.36 V at 25° C, Mg is generally one of the most reactive structural materials [54, 55]. The corrosion behaviour of Mg is attributed by the high specific dissolution behaviour and microelectroplating due to the presence of cathodically acting local impurities and secondary phases [54, 56, 57]. In ambient exposure conditions, a 10 nm MgO layer is formed on the surface within seconds of open-air exposure [58]. Once humidity is introduced, the oxide layer transforms into $Mg(OH)_2$ which is poorly soluble in water [59]. In the presence of water, a 20-40 nm thick layer of MgO and a 1.8-2.2 µm layer of $Mg(OH)_2$ has been reported [60, 61]. Although insoluble (at certain pH levels), these layers do not offer protection from further corrosion caused by solutions containing anions (in particular Cl^-, Br^-, ClO_4^-, SO_4^{2-}, and CO_3^{2-}), nitrates, and phosphates [62, 63]. Solutions composed of anions disturb the oxide phases of the layers and begin to locally degrade the passivating film/layer. For example, when the chloride concentration in an electrolyte surpasses 30 mmol/L, then $MgCl_2$ forms from the $Mg(OH)_2$ layer [64]. As corrosion persists, the pH level near the surface increases, which aids in apatite formation when immersed in simulated body fluids [65]. The overall basic corrosion process in water can be described by the following reactions [66, 67]:

$$2H^+ + 2e^- \rightarrow H_2 \qquad \text{Cathodic partial} \qquad (3.1)$$

$$2Mg \rightarrow 2Mg^+ + 2e^- \qquad \text{Anodic partial} \qquad (3.2)$$

$$2Mg^+ + 2H_2O \rightarrow 2Mg^{2+} + 2OH^- + H_2 \qquad \text{Chemical reaction} \qquad (3.3)$$

$$2Mg + 2H^+ + 2H_2O \rightarrow 2Mg^{2+} + 2OH^- + 2H_2 \qquad \text{Overall reaction} \qquad (3.4)$$

$$Mg^{2+} + 2OH^- \leftrightarrow Mg(OH)_2 \qquad \text{Product formation} \qquad (3.5)$$

As Mg corrodes, hydrogen is produced by the electrochemical process, which can be seen in Equation 3.1. This cathodic partial reaction occurs to balance the dissolution of the Mg metal or formation of Mg ions during the anodic partial reaction

of Equation 3.2. The highly reactive Mg overall undergoes the chemical reaction of Equation 3.3. It should be noted that the impedance measured mass loss or calculated release of hydrogen turns out to be lower than their actual amounts due to corrosion processes taking place on the film's covered and uncovered surfaces occurring simultaneously [68]. The discrepancy between the measured mass loss and theoretical amounts are also attributed by the surface alteration caused by physical measurements [69]. Combining the electrochemical reactions of Equation 3.1 and 3.2 with the chemical reaction of Equation 3.3, leads to the overall reaction of Equation 3.4. Furthermore, $Mg(OH)_2$ formation occurs as a product of the overall reaction in Equation 3.5 [55].

Several factors play a role in influencing the overall degradation of Mg-based implants. These factors include implant geometry, microstructure, loading and stress, and the exposure environment, each of which has been extensively investigated for its impact on degradation behaviour. Implant geometry, for instance, has been established as a determinant of degradation rates. Notably, both larger implants and those with a higher surface area have been empirically linked to an increased degradation rate, as corroborated by previous research findings [70].

Additionally, the microstructure of the Mg-based alloy utilised in implants has been examined for its influence on degradation kinetics. Research has consistently demonstrated that finer grain sizes within the material tend to enhance corrosion resistance, whereas implants with larger grain sizes may accelerate degradation, marking the significance of microstructural control in implant design and development [71]. Furthermore, the mechanical loading and stress experienced by Mg implants must also be taken into account as they have been shown to exert an accelerating effect on degradation processes [72]. Moreover, the exposure environment in which the implant resides plays a pivotal role in degradation kinetics. Factors including pH, temperature [73], the presence of specific ions [74], and oxygen concentration [75] have all been acknowledged as influential parameters that can modulate corrosion rates. Physiological conditions including these factors can vary within the body, affecting degradation behaviour.

Mechanically, Mg possesses a lower Young's modulus [76] and overall strength when compared to other commercial implant materials such as titanium [77] and steel [78]. However, Mg and Mg-alloys have closer mechanical properties to that of natural bone, which can be seen in Figure 3.2 [79, 80, 81, 82]. In general, a biodegradable material must maintain mechanical integrity as bone healing persists and is resorbed when the additional support is no longer required. Finding the correct balance and timing of mechanical stability and resorption further challenges researchers to tailor Mg-based materials.

To address the innate corrosion and mechanical challenges of Mg, production methods and alloys have been developed to improve the properties of the material. High purity Mg has been achieved through production methods to reduce impurities shown to increase degradation [83]. Alloying elements have been introduced to improve corrosion resistance and mechanical capabilities. Frequently utilised alloying elements for Mg alloys for implants are listed in Table 3.1 [84, 85].

Two main alloy systems have caught the attention of researchers in terms of alloy families that generally satisfy the requirements for a biodegradable material: the AZ series and the WE series. The most common, the AZ series, consists of Mg with trace amounts of Al and Zn. The inclusion of Al and Zn have demonstrated to

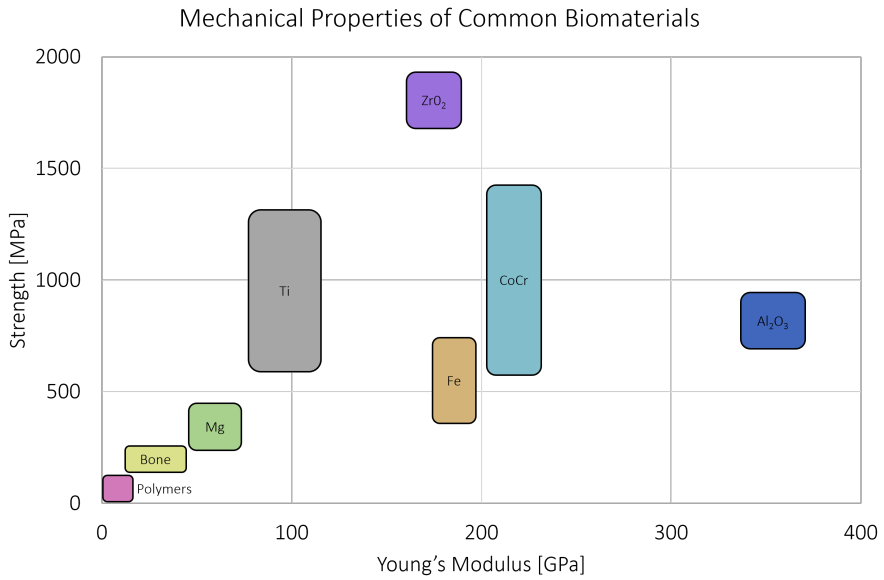

Figure 3.2: Strength and Young's modulus of commonly used biomaterials.

increase corrosion resistance and tolerance against impurity elements such as nickel and iron, respectively [86]. One issue arises with the AZ series when exposed to high temperatures, typically required for material strengthening. Alloys of this nature begin to mechanically deteriorate above temperatures over 120 °C [87]. Additionally, AZ series show relatively low toughness and ductility [88]. To address the shortcomings of the AZ series, the WE series includes rare earth elements. The series usually utilises minor alloying elements such as neodymium, zinc, and zirconium. The inclusion of these elements creates more thermally stable precipitates [87]. More importantly, the WE series have shown to maintain better creep resistance, ductility, strength, and corrosion resistance [89]. Although AZ series have demonstrated to have lower corrosion rates than WE series [90], WE series have demonstrated to promote superior biocompatibility in terms of genetic stability [91]. For these reasons, the remainder of this work investigates properties surrounding WE43.

Alloying Element	Description
Aluminium (Al)	Al exhibits high solubility in alloys, enhancing grain refinement by up to 5% and boosting alloy strength. Nevertheless, its poor biocompatibility has hindered further Mg alloy exploration. Elevated Al levels have been linked to dementia [92] and Alzheimer's disease due to high brain concentrations [93].
Calcium (Ca)	Ca is the body's most abundant mineral, with 99.5% residing in bones to maintain their mass. Ca levels are controlled by the skeletal, renal, and intestinal systems. It acts as a grain-refining agent, enhancing mechanical and corrosion properties in alloys. Yet, higher Ca content in Mg alloys leads to reduced elongation and tensile strength. Notably, Mg-Ca alloys exhibit no toxic effects after degradation [94].
Manganese (Mn)	Mn is crucial for lipid, amino acid, and carbohydrate metabolism. It also contributes to immune function, bone growth, and blood clotting. When added to alloys with Al, Mn boosts corrosion resistance while preserving mechanical strength [95]. It reduces grain size by up to 0.4 wt%, but due to cytotoxicity observed in *in vivo* studies, Mg-Mn alloys are limited to less than 1 wt% in biomedical applications [96].
Gadolinium (Gd)	Gd, a rare earth element, enhances Mg alloys, increasing corrosion resistance [97]. Tensile strength and elongation in Mg-Gd improve when Gd content remains below 6% [98].
Strontium (Sr)	Sr enhances bone mass and reduces fractures in osteoporotic care. It refines grain size, promotes bone growth, and slows corrosion. Adding small amounts of Sr increases strength [97] with no cytotoxic effects [99].
Yttrium (Y)	Y, a rare earth element, significantly refines grains and enhances tensile strength. Increased Y content improves creep and corrosion resistance [100]. Mg-Y generally exhibits good biocompatibility, but high Y concentrations in the liver and gallbladder can lead to blood toxicity [101].
Zinc (Zn)	Zn is essential for the human body, found in bones and muscles, with potential nervous system accumulation. It's a crucial trace element for the immune system, dampening hydrogen gas production and aiding in bone healing [48]. Zn enhances tensile strength and hardness. Mg-Zn alloys have been shown not to cause toxicity in the liver, spleen, and heart during in vivo studies [102].
Zirconium (Zr)	Zr is a key grain refiner and, when combined with Sr, enhances compressive strength, bone formation, and biocompatibility [103]. Adding small amounts of Zr to Mg boosts corrosion resistance, metal strength, and ductility. Zr also demonstrates excellent biocompatibility and osseointegration [104].

Table 3.1: Common elements utilised in Mg-based alloys.

3.3 Coating Technologies and Surface Modifications

To further tailor the degradation capabilities of Mg-based alloys, surface treatments have been developed to counteract the fast corrosion nature of Mg as an alternative to alloying and processing adjustments. A key challenge which hinders the use of Mg-based implants in clinical application is their inherent rapid corrosion in bodily fluids. As previously mentioned, generation of hydrogen gas due to rapid corrosion is formed at a rate too quickly for local tissue to absorb. Approximately 1 gram of pure Mg produces 1 litre of hydrogen gas [105]. This buildup of gas and uncontrolled degradation hence compromises the implant's integrity and the overall healing of the fracture site. Therefore, coating technologies (or surface treatments) have been developed to increase the corrosion resistance of Mg-based materials to address this issue [106]. Uniformity, proper adherence, biocompatibility, and biodegradability are requirements for a surface treatment or coating to be effective.

Coatings and surface treatments have been investigated as preventative measures against severe corrosion intrinsic to Mg-based alloys [107, 108]. Two main coating preparations with the aim to increase corrosion resistance are highlighted: conversion coatings and deposited coatings. Conversion coatings consist of chemical or electrochemical reactions between the base material and the external environment. In comparison, deposited coatings are coatings situated on the external of the substrate. Depending on the coating preparation, an associated coating formation technique must be employed.

One surface treatment, plasma electrolytic oxidation (PEO) is widely used due to its ability to form porous, thin coatings in addition to high adhesion strength. Also referred to as micro-arc oxidation, PEO is the most commercially available route in the development of coatings for Mg-based alloys. The process involves subjecting a metal substrate to an electrolytic bath while applying a high voltage, which leads to the formation of a plasma discharge on the surface causing localised melting and oxidation of the metal, resulting in the formation of a porous oxide layer [109].

PEO has successfully reduced corrosion rates in the past [110, 111, 112]. In particular, PEO-coated WE43 materials have demonstrated to react less severely when compared to non-coated counterparts [113]. *In vivo* investigations have revealed that not only PEO-coated WE43 maintained lower corrosion rates, but also demonstrated increased bone density and bone-implant contact area around implantation sites in the frontal bone of adult miniature pigs [114]. In terms of cytocompatibility, WE43 material treated with PEO has exhibited excellent capabilities [115]. Hartjen *et al.* introduced primary human lymphocytes to their investigation to assess the immunological response of coated and uncoated WE43. After three days of incubation, 90 % of the lymphocytes associated with the untreated WE43 were no longer viable. In contrast, more than 80 % of cells were still active after incubation with the PEO-coated material. In addition, an investigation led by Rendenbach *et al.* exhibited the slowing of corrosion and improved osseointegration for PEO-coated implants [116].

3.4 Bone Biology

To better assess the biocompatibility of an implant, or more specifically, the osseointegration capabilities of an implant, it is vital to consider the environment in which the implants are being applied to, the skeletal system of the human body. The human skeleton aids in a variety of roles required for our everyday living. The main functions of the skeleton are to provide body support, protection of organs, locomotion, storage of nutrients and energy, and to house haemopoeisis processes. Besides cartilage, joints, ligaments, and tendons, bone is a key component of the skeleton. Bones are the framework of the body and are distinct due to their hard yet elastic properties. By weight, approximately 35 % of the bone matrix is comprised of organic material (collagen) with the remainder being inorganic mineral (hydroxyapatite). A hierarchical illustration of bone composition and structure is described in Figure 3.3 [117].

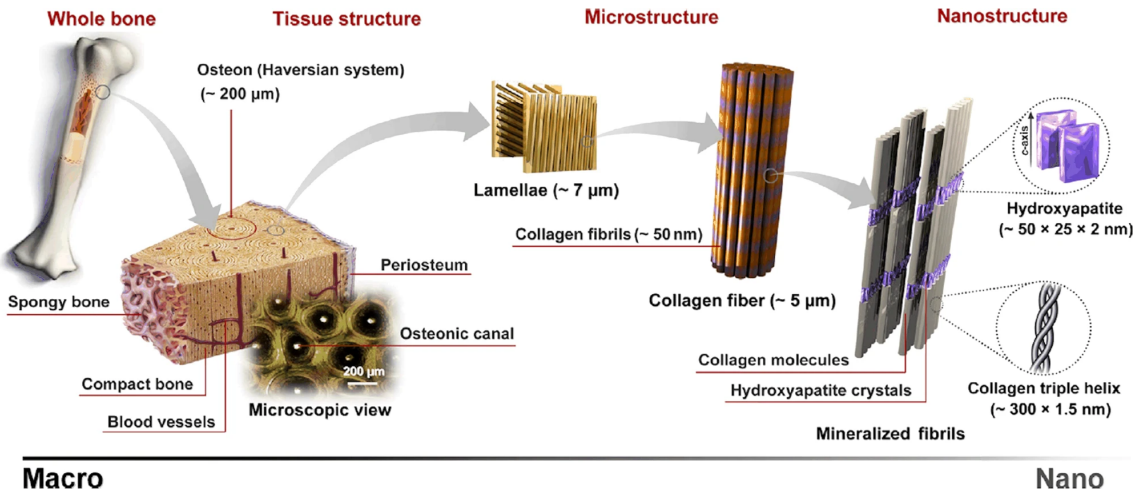

Figure 3.3: Hierarchical structure of bones from the macro- to nanoscale. The health and functionality of bones are fundamentally dependent on the structure and composition of bone tissue across various scales. (Available under the Creative Commons Attribution 4.0 International license)

Biological differences between using human bone and animal bone in medical research are substantial, primarily due to variations in anatomy, physiology, and bone properties. Animal bones, such as those from rabbits, pigs, sheep, and rodents, offer controlled experimental settings which partialy replicates human physiology [118]. Rabbits, with larger bones, are often employed in orthopaedic and dental research, while pigs provide bone structures more akin to humans, making them ideal for orthopaedic and dental studies. Sheep are frequently used for studies involving bone grafts and tissue engineering due to their bone size and physiological characteristics. Though relevant for biocompatability testing of materials, rodents like mice and rats are valuable for genetic studies but have limited translational relevance due to their smaller size and distinct bone architecture.

The processes of bone formation (osteogenesis), and bone healing which encompasses bone remodelling, are intricate biological processes crucial for maintaining skeletal integrity. Osteogenesis comprises two principal mechanisms, namely intramembranous ossification and endochondral ossification. Intramembranous ossification entails the differentiation of mesenchymal stem cells into osteoblasts, which

directly contribute to bone formation. In contrast, endochondral ossification involves the initial formation of a cartilaginous template that subsequently undergoes replacement by bone tissue, orchestrated by the mineral-depositing activities of osteoblasts. These processes of bone formation are highly regulated and finely tuned, ensuring the continuous growth and renewal of the skeleton throughout an individual's life.

Conversely, bone healing, an essential aspect of musculoskeletal physiology, represents a dynamic sequence of events set into motion in response to injuries or fractures. It commences with the formation of a haematoma at the injury site, followed by an inflammatory response that orchestrates the recruitment of specialised cells, including osteoprogenitor cells and chondrocytes. These cellular participants, guided by mechanical forces and signalling molecules, aim at restoring the compromised bone or cartilage. This process encompasses key stages, including the formation of a callus, a temporary structural reinforcement, followed by a phase of remodelling, ultimately culminating in the complete restoration of the bone's structural and functional integrity. It is crucial to highlight that the speed and efficacy of bone healing are contingent upon a multitude of factors, such as the precise location and severity of the injury, the age and overall health status of the patient, and the local micro-environment. An interplay of cellular responses and molecular signalling pathways orchestrates the healing process, ensuring the adaptation of bone to its changing mechanical requirements and repair of any structural damage incurred.

In addition to these fundamental aspects, the classification of bone based on its level of maturity is a pivotal consideration in the study of skeletal biology. This classification delineates bone into two distinct categories: immature, often referred to as woven bone, and mature, known as lamellar bone. Immature bone, being the initial form to develop during embryogenesis and following fractures, is characterised by the presence of irregularly oriented collagen fibres, rendering it mechanically weaker. In contrast, mature bone exhibits a regularity in the arrangement of collagen fibres, conferring heightened mechanical strength and integrity.

Furthermore, mature bone differentiates into two primary structural types: compact bone and cancellous bone. Compact bone, predominantly situated in the outer layers of bones, assumes a dense and solid configuration, thus endowing it with superior load-bearing capacity. On the other hand, cancellous bone, predominantly located within the interior of bones, features a porous, lattice-like architecture that facilitates metabolic processes, including bone remodelling and mineral homeostasis.

The prominent constituents among bone cells, osteocytes, contribute to bone remodelling and repair. Osteocytes, in their capacity as main regulators of bone homeostasis, play a fundamental role in orchestrating the balance between bone resorption and formation. They exert their influence through the secretion of critical signalling molecules such as RANKL [119], which serves as a potent regulator of bone resorption, and WNT1 [120], a key factor responsible for governing bone formation. This duality of action supports the versatility of osteocytes in the dynamic maintenance of skeletal integrity.

To execute their functions, osteocytes are positioned within the bone matrix, residing in specialised cavities known as lacunae. These lacunae are interconnected by a network of dendritic channels referred to as canaliculi, which permit the exchange of signalling molecules, nutrients, and waste products among osteocytes and with their surrounding micro-environment. Recent investigations have also shed light on the significance of canalicular junctions, which are presumed to play a substantial

role in the processes governed by the lacuno-canalicular network (LCN) [121]. The LCN serves as the structural backbone housing and interconnecting osteocytes, facilitating their essential communication and coordination in the orchestration of bone remodelling and repair processes (Figure 3.4).

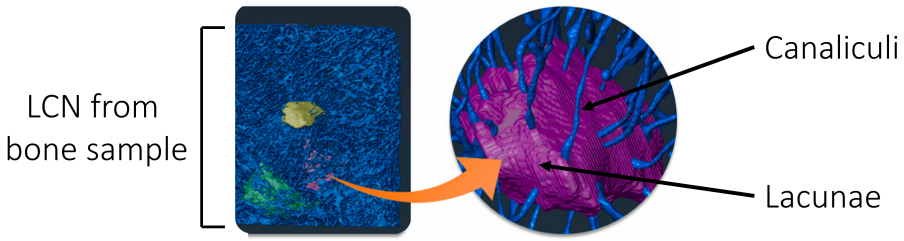

Figure 3.4: 3D renderings of the LCN in sheep bone highlighting lacunae (yellow, green, and pink colours are for visualisation purposes only) and the canaliculi (light blue).

The LCN provides a framework in which osteocytes can exchange nutrients, amplify biochemical signals, and interact with other bone cells [122]. To initiate bone remodelling, osteocytes in the LCN generate signals in response to mechanical stimuli or shear stress due to extracellular fluid flow. Local osteocytes transduce bone tissue deformations into signals which are then transmitted and amplified by the LCN, triggering the recruitment of osteoblasts and osteoclast precursor cells [123]. In addition to these mechanosensory properties of osteocytes, the extracellular fluid encapsulated in the LCN allows for mineral exchange with the extracellular matrix [124].

To further analyse the structures of the LCN and the overall interaction of biodegradable materials with the bone and the surrounding environment, biomedical imaging technologies are necessary.

Chapter 4

Background Part II: Imaging Technologies

Within the framework of this chapter, we explore advanced medical imaging technologies, with a particular emphasis on the fundamental principles and image formation mechanisms of X-ray imaging and magnetic resonance imaging (MRI). This chapter further explores synchrotron radiation-based imaging techniques, offering insights into their cutting-edge applications. Additionally, we investigate the challenges posed by metallic implants within medical imaging and their implications. The information presented in this chapter will serve as a starting point for later discussion of clinical applications, technological advancements, and the impact of these imaging technologies in the realm of medical diagnostics and healthcare.

4.1 X-ray Imaging

X-ray imaging can be traced back to the late 19th century. In 1895, German physicist Wilhelm Röntgen noticed a fluorescent screen glowing as he was investigating the radiation of a cathode-ray tube [125]. Röntgen concluded that the fluorescent screen was being illuminated by the tube via a new type of ray, which were temporarily named X-rays [126]. These rays described by Röntgen were capable of penetrating tissue and creating an image on photographic plates, which revolutionised medical imaging. X-ray imaging is a medical imaging technique that utilises X-rays, a form of high-energy electromagnetic radiation, to create detailed images of the internal structures of the human body. It is a non-invasive and commonly used diagnostic tool in medicine for visualising bones, soft tissues, and organs, as well as detecting and diagnosing a wide range of medical conditions. X-ray images are commonly used for detecting fractures, assessing joint conditions, diagnosing lung and heart diseases, and locating foreign objects within the body, among other applications.

4.1.1 Basic Principles of X-rays

X-rays are a form of electromagnetic waves and a form of radiation. The energy of each X-ray photon is proportional to the frequency which can be described as:

$$E = h\nu = \frac{hc}{\lambda} \tag{4.1}$$

Where h is Planck's constant ($6.63 \cdot 10^{-34}$ Js), ν is frequency, c is the speed of light ($3 \cdot 10^{8}$ m/s), and λ is the wavelength of the X-ray. In terms of placement along the electromagnetic spectrum, which is arranged by frequency or wavelength, X-rays fall between ultraviolet radiation and gamma radiation at 0.01 to 10 nm. X-rays are produced via one of two ways: through *bremsstrahlung* or characteristic radiation. Meaning "braking radiation" in German, *bremsstrahlung* is a form of radiation in which high energy accelerated electrons slow down when deflected by another charged particle due to atomic attraction and converts the amount of braking energy into radiation. Due to various amounts of braking possible, radiation produced is diverse. Secondly, X-rays may be produced via characteristic radiation. This form of radiation is produced by the expulsion of orbital electrons by incoming electrons. Electrons evicted in specific orbits produce a characteristic X-ray emission. An overview can be seen in Figure 4.1.

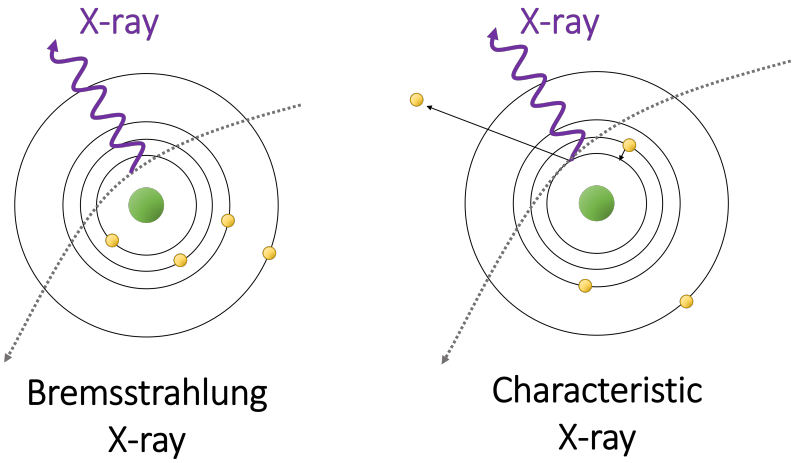

Figure 4.1: X-rays may be produced by bombarding tungsten with electrons at the anode in an X-ray tube. Electrons may lose energy and slow down which in turn produces *bremsstrahlung* X-rays (left). Alternatively, electrons may knock out an orbiting electron and an outer shell electron may fill the new vacancy. As the vacancy is filled, a characteristic X-ray is emitted (right).

Determining the penetration of X-rays within living tissue is fundamental to obtaining an image. The absorption of radiographic film is dependent on properties of X-rays and the inherent characteristics of different bodily tissue. The further the penetration of X-rays, the darker the blackening of film. Various intermediate greys can be obtained if radiation is absorbed by the tissue. Therefore, complete absorption of the X-rays results in a white image. Contrast is dependent on predominantly by the following three factors: the chemical and density properties of targeted tissue, X-ray energy, scattered radiation exposed to the film [127]. Mature bone tissue absorbs most applied radiation, resulting in their appearance as white in radiographic films. Conversely, soft tissues and gases allow for greater penetration, appearing dark grey or black. Although chemical composition of tissue cannot be altered, the applied X-ray energy and scattered radiation can be adjusted to alter contrast capabilities and ultimately the final image.

4.1.2 Image Formation

Though there are various ways to generate X-rays, we will describe the overall scanning procedure starting from the most commonly used source, the X-ray tube, for simplicity. A typical schematic representation of a scanning procedure can be seen in Figure 4.2. An X-ray tube contains a cathode and anode within an evacuated enclosure. The cathode is connected to a voltage generator and is heated via the Joule effect. As the temperature of the cathode increases, the kinetic energy of the electrons in an attached tungsten filament also increases. When the kinetic energy of the electrons overcome the binding energy of the electrons to the atoms in the filament, electrons are emitted via the thermionic effect. The electrons are then accelerated towards the target anode and characteristic X-rays or *bremsstrahlung* X-rays are generated. A less than common interaction may also occur if an electron may directly interact with the nucleus of an anode atom. In this case, a maximum energy is transferred from the electron into *bremsstrahlung*. Overall radiation of the X-rays is influenced greatly by factors such as acceleration voltage, tube current, filtration, and the material and angle of the anode. Consequently, these factors ultimately directly impact the attenuation of the X-rays of the object.

Figure 4.2: A scanning procedure typically consists of x-ray generation, where then after the x-rays are attenuated by the subject. The x-rays which pass through the subject are then detected and converted into signals which are further processed into a final image.

As the X-rays pass through an object, the intensity of the beam diminishes exponentially through a process called attenuation. Attenuation can be described by four basic interactions: the photoelectric effect, Compton (incoherent) scattering, Rayleigh/Thomson (coherent) scattering, and pair production.

The photoelectric effect states that if an incident photon maintains a higher energy than the binding energy of the atomic electrons of the target sample, an electron from a lower shell may be freed by the photon energy. Moreover, the incident photon provides a transfer additional kinetic energy to the freed electron, sometimes called the photoelectron.

When the photons of the emitted X-rays begin to lose energy and alter their direction due to the interaction with atomic electrons, Compton scattering occurs. Compton scattering occurs when the travelling photon has exceedingly higher energy than the electron binding energy. As opposed to photon absorption in the photoelectric effect, the greatly energised photon continues to travel with a lower energy or shifted wavelength in a deflected direction. The ejected electron which carries energy of the incident photon is called the Compton electron.

Rayleigh (coherent) scattering occurs when atomic electrons are targeted by low-energy photons. In this case, photons interact with local electrons found in their subsequent oscillating electric field which consequently scatter. As such, this elastic effect differs from Compton scattering since no energy transfer or ionisation occurs.

As a result, only the direction of the X-ray changes.

Overall, the sum of the four contributing factors of attenuation determines the total attenuation of the X-rays in the target sample. As the X-ray beam travels through the target sample, the intensity decreases exponentially following the Beer-Lambert law of attenuation:

$$I(x) = I_0 e^{-\mu x} \tag{4.2}$$

Where μ is the total attenuation coefficient, x is the distance travelled or thickness of the material, I_0 is the incident X-ray intensity, and I is the final intensity. However, the Beer-Lambert law in this form assumes a uniform material and monochromatic X-ray beam, which in practicality is not the case. Therefor, a varying attenuation coefficient must be accounted for by utilising the supplemented equation:

$$I(x) = I_0 e^{-\int_0^L \mu(x)dx} \tag{4.3}$$

Where the line integral along a path L where μ varies is incorporated. To adapt the equation further to consider non-monochromatic X-ray beam spectra, the equation can be modified to

$$I(x) = I_0 e^{-\int_0^L \mu(E,x)dxdE} \tag{4.4}$$

Where E is the energy of the X-rays. In practice, the equation incorporating the non-uniform μ is considered. Subsequently, the non-uniform μ results in beam hardening artefacts.

As the X-rays interact with the sample, the attenuated X-rays are captured by a detector. The detector converts the X-ray beam into electrical signals via gas ionisation or scintillation. Gas ionisation conversion directly converts the X-ray into electrical signals whereas scintillation must convert the X-rays into visible light prior to final conversion into electrical energy. This electrical energy, or signals, are further converted into binary code information. In the case of radiography, the binary code information represents the attenuation coefficient of the material. This information can then be translated to a discrete value representing a brightness value, which can further be represented in a pixel of the final image. Moreover, image filtering such as noise suppression, smoothing, or edge enhancement can further be applied to the image or set of pixels to further process the image.

Computed Tomography

Computed Tomography (CT) is closely related to X-ray imaging, as it is built upon the fundamental principles of X-ray technology. Both methods involve the use of X-rays to visualise the internal structures of the human body. However, the key distinction lies in how they capture and present these images.

In medical X-ray imaging, a stationary X-ray source emits a beam of X-rays that passes through the body and is detected on the other side. The resulting image is a two-dimensional projection that shows the superimposed structures along the X-ray path. This technique is valuable for visualising dense structures like bones but lacks the ability to distinguish between soft tissues effectively. In contrast, CT combines a rotating X-ray source and a detector array to capture multiple X-ray images from various angles as they pass through the body. A computer then

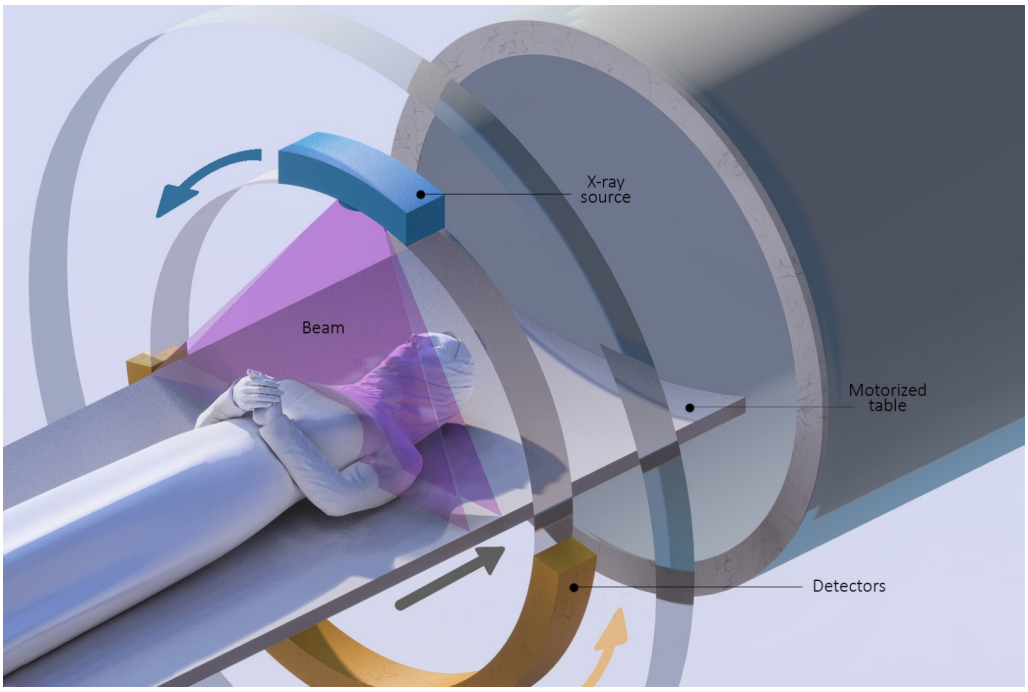

Figure 4.3: Example of CT imaging setup including X-ray source and beam, detectors, and motorised patient table.

processes this data to reconstruct cross-sectional images, or "slices", of the scanned area. These slices can be stacked together to form a detailed three-dimensional representation through a process called reconstruction, offering superior spatial resolution and tissue differentiation compared to conventional X-ray imaging. CT image reconstruction is a mathematical procedure that produces tomographic images from X-ray projection data obtained at various angles around the patient. This intricate layering of images enables healthcare professionals to visualise internal structures with remarkable clarity, making CT an essential tool for diagnosing a wide range of medical conditions, including cancer, trauma, and vascular diseases. An example of a CT setup is seen in Figure 4.3. Imaging methodologies scaled at higher complexity exist where X-ray generation and contrast development differ from what has been discussed previously.

Imaging Contrast

To further enhance details captured of materials with subtle differences in attenuation, phase contrast can be applied. Phase-contrast X-ray imaging is an advanced X-ray imaging technique that goes beyond traditional X-ray methods, primarily used for visualizing the density of tissues, bones, and other anatomical structures. One method developed by Frits Zernike in 1934 [128], enhances the visualization of soft tissues by taking advantage of the phase shift that X-rays undergo as they pass through different materials. Unlike conventional X-ray imaging, which relies on the absorption of X-rays, phase-contrast imaging primarily focuses on the changes in the phase of X-rays as they interact with tissues.

Moreover, contrast agents may be administered to emphasize vasculature before and after intravenous injection. Contrast agents can be chemically functionalised (for example, with antibodies) to specifically target molecules of certain cells and

tissue [129]. Other X-ray imaging techniques such as X-ray fluorescence for the use of non-invasive elemental analysis or Dual-energy X-ray imaging [130] are frequently used today but is out of the scope of this work.

Though clinical X-ray imaging presents us the capability to see the internal human body, the imaging technique does not come without patient safety risk. X-ray imaging involves exposure to ionising radiation which may damage the molecules found in body tissue. Biological damage due to radiation can be described as either stochastic or non-stochastic [131]. Stochastic effects are "all-or-nothing" effects which injure the DNA found in a cell, which may lead to an increased risk of cancer. Stochastic effects increase with X-ray exposure. Unlike stochastic effects, non-stochastic (deterministic) effects are dose-dependent which may include vomiting, diarrhoea, lung fibrosis, skin burns, thyroiditis, cataracts, and suppression of ovulation or sperm count [132]. As the awareness of X-ray radiation and the corresponding danger grows, safety precautions are put in place to protect both the patients and medical professionals. Advancements in imaging technology and safety protocols have led to a significant reduction in radiation exposure during X-ray imaging in recent years [133, 134]. For this reason, synchrotron-radiation sourced imaging is incompatible with clinical imaging.

4.1.3 Synchrotron Radiation-based Imaging

In addition to X-ray tubes, synchrotrons are utilized for generating X-ray radiation in large-scale for basic science research. Synchrotron facilities employ bending magnets or insertion devices to manipulate the trajectory of either electrons or positrons [135]. The resultant X-rays exhibit notable characteristics, including high collimation, monochromaticity (single energy), and high photon density, thereby significantly enhancing their imaging capabilities. While unsuitable for most clinical applications, these generated X-rays are precisely directed towards distinct beamlines tailored for diverse types of experiments. The distinct advantage of utilizing such particle accelerators lies in their capacity to produce tightly focused, monochromatic beams that are exceptionally coherent, brilliant, and readily tunable. Furthermore, these configurations offer superior image quality with expedited acquisition times. However, it should be noted that synchrotrons necessitate a substantial physical footprint, often spanning hundreds of meters or even kilometers in setup dimensions.

X-ray generation via synchrotron radiation enables nano tomographic three-dimensional imaging such as near field X-ray holography, ptychography, and transmission X-ray microscopy (TXM) [136]. These modalities are able to obtain approximately 50 nm in resolution, surpassing typical clinical CTs of 1-2 mm. Though these imaging methods provide similar resolution, TXM requires significantly less computational time for reconstruction of a 3D tomogram [137]. TXM can either be employed in scanning or full-field mode. In scanning mode, X-rays are focused onto a point via optical systems and is scanned for multiple points along the sample. In this mode, X-ray diffraction measurements may simultaneously take place. In contrast, full-field mode illuminates the whole sample at once and results in shorter imaging times. An example of a full field synchrotron-based TXM setup can be seen in Figure 4.4 [138]. X-rays are prepared and shaped with optics prior to illumination of the sample and are then focused onto the detector via a Fresnel zone plate. Zernike phase rings are added behind the zone plate to enable phase contrast prior to the

final rays being captured by a detector (camera).

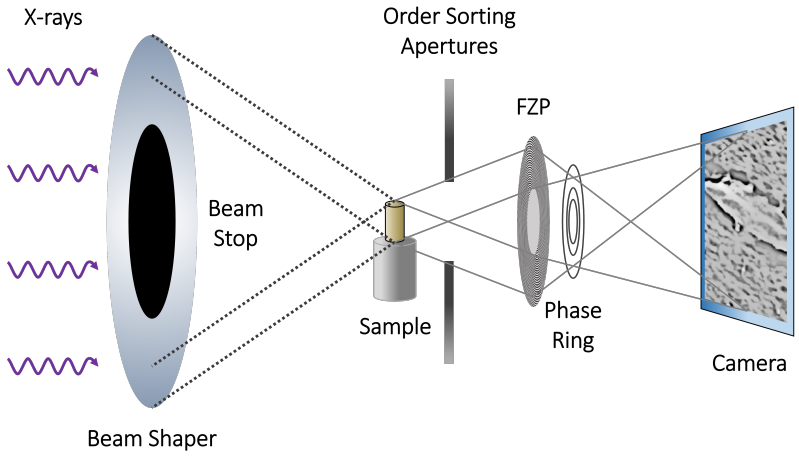

Figure 4.4: Example of TXM schematic of Zernike phase contrast setup.

While X-ray imaging excels in providing contrast for bone structures, magnetic resonance imaging (MRI) has established itself as the gold standard for distinguishing and visualizing soft tissue. Additionally, MRI offers the notable advantage of non-ionizing radiation-based imaging.

4.2 Magnetic Resonance Imaging

Magnetic resonance imaging (MRI) was first proposed by Paul C. Lauterbur in 1973 when he published images of the nuclear magnetic resonance response of glass capillaries filled with water [139]. Since then, MRI technology has rapidly evolved, with advancements in imaging speed, resolution, and the development of various specialised MRI techniques for diagnosing a wide range of medical conditions, making it a crucial tool in modern healthcare and medical research.

There are several different types of MRI techniques which are tailored to provide specific information not only about body tissue, but also about function. T_1 (longitudinal relaxation time)-weighted imaging is often employed in brain and musculoskeletal imaging by distinguishing different tissues based on their relaxation times [140, 141]. T_2 (transverse relaxation time)-weighted imaging highlights differences in the water content in tissue which may be utilised for detecting oedema or fluid-filled cyst abnormalities [142]. Diffusion-weighted MRI measures water movement within tissues which aids in the detection of stroke or tumours [143]. Functional MRI (fMRI) detects changes in blood flow and oxygenation levels in the brain, enabling brain mapping activities and research in cognition and neurological disorders [144]. Other popular techniques include magnetic resonance angiography [145], perfusion-weighted MRI [146], and Dixon MRI [147].

4.2.1 Basic Principles of MRI

The foundation of MRI is based on the nuclear spin of atoms. Nuclear spin is classically defined as the rotation of the nucleus about an axis at a fixed rate [148]. Discrete values for nuclear spin are quantified as zero, half-integer, or integer which

depend on the atomic weight and atomic number. Nuclei with no spin have both an atomic weight and atomic number which is even and does not interact with external magnetic fields, rendering these nuclei incompatible with MRI studies. Therefore, nuclei with non-zero spin can be studied with MR techniques. The ^{1}H nucleus for example, is an ideal candidate for MRI studies as it is the most abundant isotope of hydrogen and is found in the human body within fat and water.

Nuclear magnetic resonance (NMR) is inherently a quantum mechanical phenomenon, involving rigorous maths and laws of quantum mechanics. However, most MR can be described using themes of classical mechanics since the collective behaviour of nuclei resembles a familiar scenario: a spinning top interacting with a magnetic field. Therefore, the subsequent content within this work will continue to discuss MR phenomena utilising classical mechanics. The reader is encouraged to explore further text describing quantum behaviour of nuclei in MRI for further details [149].

As the positively charged nucleus rotates at a fixed rate, a constant local magnetic field or magnetic moment is induced parallel to the axis of rotation. The magnetic moment, analogous to a bar magnet, therefor defines a magnitude and orientation of the magnetic field. The basis of MR signals can then be established as the orientation of the nuclear spin may be externally affected. In terms of MR measurements, data is observed on the collection of spins, rather than individual spin. An arbitrary volume of tissue without external magnetisation will have a vector sum of zero since the entire selection of protons are randomly oriented. Conversely, in the presence of an external magnetic field $\mathbf{B_0}$, the individual protons begin to rotate perpendicular to the magnetic field. This rotation, also known as precession, is constant and tilted slightly away from the axis of $\mathbf{B_0}$ (Figure 4.5).

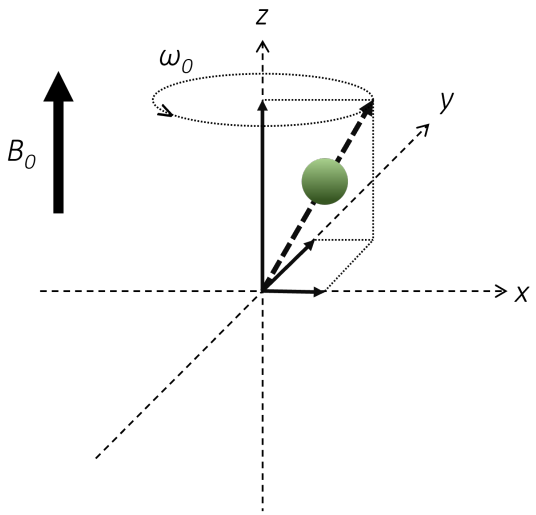

Figure 4.5: Positively charged nucleus (green) rotating at a fixed rate in Cartesian coordinates.

The rate of precession is proportional to the magnetic field strength and can be described as:

$$\omega_0 = \gamma B_0 \tag{4.5}$$

Where w_0 is the Lamor frequency (MHz), $\mathbf{B_0}$ is the applied magnetic field

strength, and γ is the gyromagnetic ratio unique to the nuclei. The gyromagnetic ratio of a particle or system is the ratio of its magnetic moment to its angular momentum. Though $\mathbf{B_0}$ creates a non-zero net magnetisation along the z-direction, the spin orientations are still randomly distributed along the x-y plane, resulting in the absence of a net magnetisation along the x-y directions. In comparison, the magnetisation along $\mathbf{B_0}$ exists due to the coupling between the protons and $\mathbf{B_0}$, known as the Zeeman interaction. This coupling causes the z-component of the magnetisation to be either parallel to $\mathbf{B_0}$, or anti-parallel against $\mathbf{B_0}$, which results in a difference of energy between the two orientations. The difference leads to a slightly positive z-value, or net magnetisation $\mathbf{M}$, which does not vary with time (Figure 4.6).

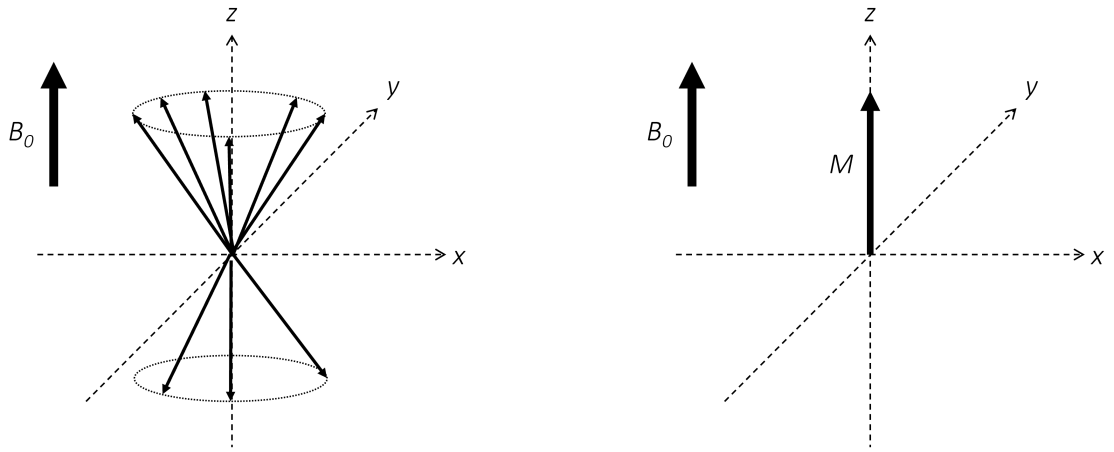

Figure 4.6: Randomly oriented spins (left) align along the main magnetic field or against the main magnetic field (antiparallel). As a result, a net difference between spins along or against the main magnetic field lead to a positive net magnetisation, M (right).

To further provide a basis of image contrast within MRI, radio frequency excitation must be understood as means of energy transfer. To manipulate $\mathbf{M}$, a pulse of radio-frequency (RF) energy can be applied. This excitation pulse typically is composed of narrow bandwidth of frequencies originated around a central frequency. The specific absorbed frequency is dependent on the applied magnetic field, $\mathbf{B_0}$. Subsequently as the RF transmitter is shut off, the protons re-emit the energy at that same frequency. When a proton absorbs the energy, it is excited from lower energy orientations to higher ones. In parallel, protons in the higher energy level are stimulated to release energy and shift towards a lower energy level. The energy difference, ΔE, between the upper and lower levels is proportional to the frequency:

$$\Delta E = h\omega_0 = h\gamma B_0 \tag{4.6}$$

Where h is Planck's constant ($6.626 \cdot 10^{-34}$ Js). It is only at this energy where transitions can be completed between spin-up and spin-down energy levels.

The process in which protons release absorbed energy from the RF pulse is called relaxation. Relaxation provides the fundamental mechanism for image contrast and describes the act in which protons return to their original configuration after excitation. Relaxation is time-dependent and is described by the corresponding

relaxation times: T_1 and T_2. Though both types of relaxation times measure the emitted energy transfer of an irradiated proton, they differ in how the energy is dissipated.

T_1 relaxation time (also known as spin-lattice relaxation or longitudinal relaxation time) is defined as the time required for the z-component of the net magnetisation **M** to return to 63% of its original value proceeding an excitation pulse. If a 90° excitation pulse is absorbed by the sample, **M** will rotate onto the x-y plane and reduce longitudinal magnetisation. As time persists, the longitudinal magnetisation will return as the protons release energy with the following exponential growth:

$$M(\tau) = M_0(1 - e^{-\frac{\tau}{T_1}}) \tag{4.7}$$

Where τ is the time after the RF pulse. T_1 relaxation times are relatively slow (miliseconds to seconds) with a 95% return value of original $\mathbf{M_0}$ after 3 T_1. Spin-lattice relaxation refers to the energised proton (spin) releases its energy to its surroundings (lattice) which maintain molecular motion with the same resonant frequency.

T_2 relaxation time (also known as spin-spin relaxation or transverse relaxation time) is the time required for the transverse component (or component along the x-y plane) to decay to 37% of its initial value. After a 90° pulse causes $\mathbf{M_0}$ to flip onto the x-y plane, complete coherence is in the transverse plane. As time continues, the coherence diminishes, and the protons reorient along $\mathbf{B_0}$. As coherence is decreased, the transverse component of $\mathbf{M_0}$ decreases to 0. T_2 or T_2* relaxation describes this very process. At the end of a 90° pulse, the protons which absorbed the energy to orient $\mathbf{M_0}$ in the x-y plane, precess at the same frequency and are synchronised. Since protons in the same vicinity will have the same frequency, energy is easily transferred between neighbouring protons. Spin-spin relaxation refers to this energy transfer, differing from energy transfer to the environment as seen in T_1 relaxation. The dephasing T_2 is always less than or equal to T_1. The total transverse relaxation time (T_2*) is defined as

$$\frac{1}{T_2{}^*} = \frac{1}{T_2} + \frac{1}{T_{2M}} + \frac{1}{T_{2MS}} \tag{4.8}$$

Where T_{2M} is the dephasing time due to main field inhomogeneities and T_{2MS} is the dephasing time due to magnetic susceptibility differences. T_2* is particularly sensitive to magnetic field inhomogeneities, which are exacerbated by the presence of metallic implants that may require refocusing. The transverse magnetisation decays after a 90° pulse:

$$M_{XY}(t) = M_{XYmax}e^{-\frac{t}{T_2{}^*}} \tag{4.9}$$

Where M_{XYmax} is the maximum transverse magnetisation following the excitation pulse. It is important to note that a difference between T_1 and T_2 relaxation is the amount of $\mathbf{B_0}$ influence. T_1 is sensitive to $\mathbf{B_0}$, where longer T_1 is measured for tissue at higher $\mathbf{B_0}$. It is only when $\mathbf{B_0}$ is less than 0.05 T where significant changes can be noticed in T_2. T_2*, T_{2M}, and T_{2MS} become greater at higher $\mathbf{B_0}$. Therefor, T_2-weighted images will have little sensitivity to $\mathbf{B_0}$, while T_2*-weighted images will show variations at higher $\mathbf{B_0}$.

Following the foundational concepts of magnetisation vectors, precession, and relaxation times, we introduce the mathematical framework that governs the dynamics of NMR. The Bloch equations, named after physicist Felix Bloch, provide a comprehensive description of how the magnetisation vector evolves under the influence of an external magnetic field and intrinsic relaxation processes.

The Bloch equations are pivotal in understanding the behaviour of nuclear spins in a magnetic field, encapsulating both the precessional motion and the relaxation mechanisms. These equations are expressed as a set of coupled differential equations that account for the longitudinal and transverse components of magnetisation:

$$\frac{dM_x(t)}{dt} = \gamma(\boldsymbol{M}(t) \times \boldsymbol{B}(t))_x - \frac{M_x(t)}{T_2} \tag{4.10}$$

$$\frac{dM_y(t)}{dt} = \gamma(\boldsymbol{M}(t) \times \boldsymbol{B}(t))_y - \frac{M_y(t)}{T_2} \tag{4.11}$$

$$\frac{dM_z(t)}{dt} = \gamma(\boldsymbol{M}(t) \times \boldsymbol{B}(t))_z - \frac{M_z(t) - M_0}{T_1} \tag{4.12}$$

where $\mathbf{M}$ is the nuclear magneization, $\mathbf{B}$ is the magnetic field experienced by the nuclei and M_0 is the steady state nuclear magnetization in the z direction.

By integrating the Bloch equations, we can predict the time-dependent behaviour of the magnetisation vector, which is essential for the accurate interpretation of MRI signals. This mathematical model not only enhances our understanding of the underlying physics but also informs the development of advanced imaging techniques and sequences.

System Components

An MRI machine comprises of several main system components which work together to provide meaningful and highly detailed images. A main magnet is the core component of the MRI machine which generates a strong, static magnetic field which can range from 1.5 T to ultrahigh fields such as 7 T. The main magnet ensures that the hydrogen nuclei within the patient's body is aligned along the static magnetic field. Gradient coils are additional electromagnetic coils that create varying magnetic field gradients within the main magnetic field. The field variations caused by the gradient coils are essential for spatial encoding. Moreover, radio-frequency or RF coils are used for the transmission of RF pulses into the patient's body and receiving the returning signals. MRI machines may have multiple types of RF coils for different applications. For example, body coils are used for larger anatomical areas such as the abdomen, while specialised surface coils may be used for areas of smaller interest such as the head. A patient table is also required to place the patient in and out of the magnetic bore of the MRI.

A powerful computer system is involved for data acquisition, image reconstruction, and processing. This system is found in the operator console, where a technologist or radiologist may control and monitor the scan. Here, imaging sequences can be selected, and parameters may be adjusted. The operator console also allows the user to communicate with the patient. Other components include shielding and safety features, a cooling system for the magnets, gradient amplifiers, and other patient monitoring equipment which are MR compatible may also be utilised.

4.2.2 Image Formation

The first step required in producing an image (Figure 4.7) is to select the region of interest. Localisation is achieved by frequency-selective excitation and by applying a slice selection gradient, G_{SS}, altering the precession of the protons along the gradient. The direction of the gradient is used to select the slice orientation. For further localisation, the frequency-selective pulse in combination with the amplitude of the slice selection gradient determine the slice thickness and slice position. When the selective pulse is applied in the presence of G_{SS}, a local region of tissue achieves a resonance condition matching the central frequency (and narrow bandwidth) of the pulse. Multi-slice imaging is achieved by varying the central frequency of the excitation pulse, thereby exciting different regions of tissue.

Figure 4.7: The image formation process in MRI begins with selecting a slice from the volume of interest. To capture elements of this slice, frequency and phase encoding occurs prior to a signal readout. The signals are then processed to form the final image.

Once the selected area is excited, signal detection from released energy is required. Frequency encoding (also known as readout) requires the use of a readout gradient (G_{RO}) to provide spatial dimensions of an image. Following the G_{SS}, the G_{RO} is applied to precess the selected protons at different frequencies, dependent on the location within the gradient. The frequencies are superimposed into the echo to be measured by a receiver coil for further processing. Information regarding the third direction is captured via phase encoding. The phase encoding gradient, G_{PE}, is used to increase or decrease the precession along the third direction. Once the G_{PE} is removed, the protons return to their original frequency with a difference in phase.

As the echo is measured by the receiver coil, the signal is digitised as a function of time in both real and imaginary values. The complex data is stored in an array where the detected signal amplitudes correspond to a row, indexed by G_{PE}. The raw data matrix is therefor composed of frequency encoding direction along the horizontal, and phase encoding along the vertical.

To convert the raw data into image data, a mathematical transformation must be completed. K-space in MRI is a data collection process that involves systematically sampling the magnetic signals emitted by the body during an imaging scan [150]. Each point in k-space represents a different frequency and phase of the magnetic signals. Once all the necessary data points are collected, complex mathematical transformations, such as Fourier transformation, are applied to rearrange and combine this data into a final image. This process allows MRI scanners to produce high-quality images of the body's internal structures, with different points in k-space contributing to different features and details in the resulting image.

4.2.3 Imaging Medical Implants

Medical implants can exert a substantial impact on MRI due to their potential interactions with the robust magnetic fields and radio-frequency pulses employed in the MRI imaging procedure. Metallic implants, such as pacemakers, joint prostheses, or surgical clips, can distort the magnetic field, causing image artefacts and potentially damaging the implant or surrounding tissues due to heating effects. Additionally, some implants can limit the visibility of nearby tissues or structures in the MRI images. Patients with implants should inform their healthcare providers and MRI technologists about their implants before undergoing an MRI, as special protocols and precautions may be necessary to ensure the safety of both the patient and the quality of the imaging study. In some cases, patients with certain types of implants may be advised not to undergo MRI, or alternative imaging modalities like CT scans may be recommended.

Magnetic Susceptibility

Metallic implants typically consist of materials characterised by a notable degree of magnetic susceptibility χ. Magnetic susceptibility quantifies the extent to which a material becomes magnetised when subjected to an external magnetic field [151]. It serves as a basis for classifying materials based on their responsiveness to such fields. A diamagnetic response ($\chi<0$) is inherent to all materials due to the presence of electrons orbiting atomic nuclei, albeit it is generally weak, resulting in a subtle repulsive force. This response predominates in the case of most materials, including biological tissues. A paramagnetic response ($\chi>0$) is more pronounced than diamagnetism but remains relatively feeble. This response emerges in molecules containing unpaired electrons that may align themselves under the influence of an external magnetic field, generating modest attractive forces. More importantly, certain metals exhibit ferromagnetic responses ($\chi\gg0$), where atomic alignment yields a robust attractive force. Ferromagnetic materials retain permanent residual magnetisation even upon removal from an external magnetic field. When placed within the strong and uniform magnetic field of an MRI machine, ferromagnetic materials can experience significant attraction forces and may be drawn into the magnet bore with great force. This poses several potential hazards in an MRI environment. The movement of ferromagnetic objects toward the MRI magnet can endanger patients and medical staff, as these objects can become projectiles if they are not securely anchored. Consequently, materials with ferromagnetic characteristics demand strict exclusion from MRI scanning environments for safety considerations.

Artefact Production

The presence of metallic implants may give rise to image distortion artefacts, commonly referred to as susceptibility artefacts. These artefacts emerge due to the intrinsic magnetic susceptibilities associated with metallic materials, resulting in localised perturbations of the magnetic field within the imaging region. Consequently, these alterations in the resonance frequency lead to pixel misalignment, resulting in notable geometric distortions, which may manifest as signal attenuation or voids (appearing as dark regions within the image) and signal enhancements (manifesting as bright regions within the image). These distortions are primarily a consequence

of disruptions in the static magnetic field and are intrinsically linked to the specific material properties of the implant. While numerous techniques have been devised to reduce artefact manifestations such as SEMAC and MAVERIC [152, 153, 154, 155], it is pertinent to note that complete elimination of metallic artefacts remains an unattained objective in MRI imaging.

Implant Heating

Medical implants introduce notable challenges, potentially leading to radio-frequency (RF) interference concerns within the context of MRI. Implant-related heating issues can arise due to exposure to two distinct time-varying fields intrinsic to MRI: RF field transmission ($B_1{}^+$) induced heating and heating stemming from switched magnetic field gradients (B_G) [156]. MRI operations entail the utilisation of radio-frequency (RF) power transmission to facilitate signal and image generation, where $B_1{}^+$ generated by a transmit RF coil serves as a key component for spin excitation, characterised by base frequencies in the megahertz (MHz) range. Meanwhile, spatial encoding, integral to MR image generation, relies on switched magnetic field gradients (B_G), characterised by frequencies in the kilohertz (kHz) range [157]. In accordance with Faraday's law, time-varying magnetic fields inherently yield electric fields (E-fields), which, in turn, prompt the generation of eddy currents. These induced eddy currents have the potential to deposit power within implants, subsequently creating secondary electromagnetic (EM) fields surrounding the implant. This phenomenon may give rise to tissue heating concerns, with the extent of RF power deposition-induced heating and heating induced by switched magnetic field gradients varying depending upon factors such as material composition, shape, spatial location, orientation, and degradation state of the conductive implant [158].

The geometry of orthopaedic screws presents a significant concern regarding RF heating. The specific absorption rate (SAR) quantifies the averaged RF power absorbed per unit of exposed mass over time [156]. SAR, in turn, is contingent upon tissue properties and MRI hardware characteristics. The surrounding tissue contributes attributes such as electrical conductivity and mass density, while the imaging hardware governs the E-field. To limit heating and mitigate high SAR values, adjustments have been made to MRI techniques and protocols. These modifications involve reducing the power of RF excitation pulses and extending the repetition time between such pulses. Noteworthy advancements in MRI hardware and methodologies aimed at reducing RF-induced implant heating have been reported extensively [159]. Pioneering strategies encompass the alteration of RF transmission fields through the utilisation of RF arrays and parallel transmission techniques featuring maximum and null current modes [160, 161].

The eddy currents generated in response to the effective transmission field $B_1{}^+$ exhibit a "skin effect" phenomenon, a fundamental principle in electrodynamics, which confines these currents to the metal's surface. While the heating of small implants like screws may be minimal, the secondary E-field induced by these eddy currents can pose risks at critical locations along the implant [156]. The primary contributor to RF-induced heating arises from RF currents indirectly induced in adjacent tissue by this secondary E-field. Additionally, slender structures such as thin wires, screws, and other one-dimensional geometries may be susceptible to the "antenna effect", leading to heightened heating. This phenomenon manifests as intensity peaks when the implant length aligns with one-quarter to one-half of the

RF wavelength within the surrounding tissue [162]. Consequently, increased heating tendencies are observed for such thin geometries, particularly pronounced at the tip ends of the implant.

The amount of information on how non-traditional implants behave in the MRI environment falls short compared to the numerous accounts of traditional metallic implants. The following chapter aims at filling this gap to provide how MRI has been used in Mg-based implant investigations.

Chapter 5

The current performance of biodegradable magnesium-based implants in magnetic resonance imaging: A review

This study presents a comprehensive review of the existing body of literature concerning the application of Magnetic Resonance Imaging (MRI) for the analysis of Mg-based implants. The investigation initiates with an introduction to Mg as a biomaterial and fundamental MRI principles, establishing a foundational understanding for the reader. The primary objective of this review is to assess the performance of Mg-based implants in the context of MRI analyses. Furthermore, this work undertakes a comparative evaluation of Mg-based materials against conventional implant materials, with the aim of confirming their potential suitability for clinical use. To achieve this, an extensive survey of current literature utilising MRI for the analysis of Mg-based implants was conducted, with specific attention to details regarding image artefacts. Among the multitude of studies examined, nine were selected based on predefined inclusive criteria, with four of them explicitly addressing the issue of image artefacts. The findings from this review affirm the successful use of MRI in analysing the soft tissue and blood vessel environment surrounding Mg-based materials. Importantly, it was observed that Mg-based materials exhibited fewer image artefacts when compared to alternative materials in various investigations. These favourable outcomes lend support to the viability of Mg-based materials for clinical utilisation, supplemented by their compatibility with MRI visualisation techniques.

The results have been published in the journal *Bioactive Materials* and has been reproduced with permission.

Bioactive Materials 6 (2021) 4360–4367

Contents lists available at ScienceDirect

Bioactive Materials

journal homepage: www.sciencedirect.com/journal/bioactive-materials

The current performance of biodegradable magnesium-based implants in magnetic resonance imaging: A review

Jonathan Espiritu [a,*], Martin Meier [b], Jan-Marten Seitz [a]

[a] Syntellix AG, Hannover, Germany
[b] Hannover Medical School, Hannover, Germany

ARTICLE INFO

Keywords:
Magnetic resonance imaging
Magnesium
Biodegradable implants
Medical imaging
Patient safety

ABSTRACT

Magnesium-based implants are re-emerging as a substantial amendment to standard orthopaedic implants. A brief introduction of magnesium (Mg) as a biodegradable material and basic magnetic resonance imaging (MRI) principles are discussed. This review aims to highlight the current performance of these implants during examinations with MRI. We also aim to summarise comparisons between Mg-based implants with current standards to emphasise the promotion of biodegradable implants in clinical practice. A comprehensive search of current literature on Mg-based implants and the utilisation of MRI in the studies was performed. Additionally, recorded artefact behaviour of Mg-based implants during MRI was investigated. A total of nine studies were included in which MRI was employed to image Mg-based implants. Of those studies, four of the nine discuss artefact production caused by the implants. MRI successfully imaged regions of interest over all and produced fewer artefacts than other materials used in the studies. MRI was employed in contrast angiography, bone growth observation, bone infection healing, and blood perfusion. Imaging capabilities of an implant material are vital to translating products into clinical application. Positive findings presented in this review suggest and support the use of Mg-based implants due to their successful visual compatibility with MRI techniques.

1. Introduction

Research in magnetic resonance imaging (MRI) has seen a strong increase in growth over the past decade. The recent advancements are warranted by the ability of the modality to provide excellent soft tissue contrast at high resolution. Additionally, MRI extends past other imaging methods by allowing for functional imaging. Metabolic functions such as tissue oxygenation, flow, diffusion, and perfusion can be visualised in MRI [1]. Although other imaging modalities like computed tomography provide detail on bone condition, MRI provides information on surrounding organs, vascular networks, and soft tissue around the implant. Long-term effects are also considered negligible since the modality does not administer any ionising radiation [2]. These assets of MRI make the imaging method favourable in various pre-clinical and clinical settings.

In parallel, significant strides have been accomplished in the area of medical implants. Constant development in the field of material science and engineering have allowed for the possibility to introduce implants into human medical applications. To date, medical implants have been employed in neural, sensory, and spinal environments. Medical implants have functioned as organ stimulation devices as well as tools for cosmetic and dental purposes. Structural implants in the form of stents, braces, rods, heart valves, bones, pins, hip prosthesis, eye, ear, skull implants and knee replacements have also been designed [3]. For a medical device to be successfully implanted, the biocompatibility of the material must be ensured. Previously, metallic implants based on titanium (Ti), stainless steel (SS), and cobalt-chromium alloys have dominated the market as orthopaedic implant material. However, magnesium (Mg) has recently been reintroduced as an appropriate alternative due to its special properties.

The first documented use of Mg in the clinical setting dates to 1878. Edward C. Huse, a physician, successfully implemented Mg wires as blood vessel ligatures [4]. Unfortunately, fast corrosion led to the early abandonment of the biomaterial. Early investigations had shown pure magnesium falling short due to fast corrosion and poor mechanical integrity [5]. Not until later was this main issue addressed by the creation of Mg-based alloys to control the problematic characteristic. To solve this, alloying elements have been introduced to increase corrosion

Peer review under responsibility of KeAi Communications Co., Ltd.
* Corresponding author.
E-mail address: espiritu@syntellix.com (J. Espiritu).

https://doi.org/10.1016/j.bioactmat.2021.04.012
Received 26 October 2020; Received in revised form 24 March 2021; Accepted 12 April 2021
Available online 30 April 2021

resistance and strengthen material matrix [6]. Such elements include calcium, zinc, manganese, strontium, tin, and silver have been chosen to improve corrosion resistance and material strength [7]. Mg binary alloys have been investigated but resulted in poor yield strength and high corrosion rates [8]. Instead, results from binary alloys have been utilised to develop multi-elemental alloys such as AZ31 [9], AZ91 [10], AM60 [11], LAE442 [12], and WE43 [13]. Notably, Mg-RE-based alloys exhibit good corrosion performance and high strength [8].

Currently, Mg and Mg-based alloys hold many benefits as an implant material option. The ability to safely degrade in-vivo as a load-bearing implant is arguably the most attractive property of the material [14]. As a biomaterial, Mg alloys more similarly align with natural bone than other alternatives. The elastic modulus of Mg alloys (45 GPa) matches relatively closer to that of bone, 3–20 GPa, unlike Ti alloys and SS (110 and 200 GPa, respectively). Additionally, Mg alloys surpass Ti alloys and SS by closely matching human cortical bone density. The similar elastic modulus and densities of Mg alloys and natural bone help prevent negative mechanical defects such as stress-shielding [15].

Not only does Mg appropriately fulfil mechanical stability, but Mg alloys also possess good biocompatibility in terms of Williams definition [16]. Already found in abundance in the human body, Mg is a key element utilised in metabolic processes. Mg is reported to stimulate the growth of bone cells and accelerates the healing of bone tissue [17]. Excess Mg cations, a corrosion product of Mg alloys, do not present risk to the body as it is eliminated in urine [18]. As mentioned previously, the ability of Mg to degrade in a physiological environment is a particular advantage that is unique to the material. Permanent orthopaedic implants which remain in the body have shown to cause inflammatory responses [19,20] as well as further refracture risk [21]. These bodily responses and mechanical failures suggest that temporary solutions be investigated. With the degradation capability of Mg, the need for secondary surgeries to remove the implant is eliminated. Although able to degrade, iron- [22] and polymer-based [23] degradable materials pose as inferior to Mg alloys as they do not stimulate bone growth and poorly match the mechanical properties of bone. Therefore, Mg-based implants present as a biocompatible, biodegradable, lightweight, load-bearing orthopaedic option.

To gain market footing and wider usage as an alternative implant material, medical imaging compatibility must be ensured for successful clinical translation of Mg-based implants. MRI offers the ability to observe soft tissue surrounding Mg-implants as they degrade during patient healing, an essential aspect for physicians. The aim of this review is to highlight and evaluate the current performance and application of Mg-based implants in the MRI environment.

1.1. Basic MRI principles

Magnetic resonance imaging (MRI) makes use of the magnetic properties of certain atomic nuclei. Most prominent is the single proton present in water molecules, therefore present in all biological tissues. An image produced in MRI displays certain radio frequency (RF) signal intensities or phases. These signals originate from human tissue where many of the free hydrogen nuclei align themselves with the direction of the magnetic field after being stimulated by RF signals. Following relaxation, the nuclei lose energy by emitting their own RF signal. Tissue is susceptible to magnetisation due to the presence of protons in the nuclei of hydrogen atoms. Protons contained in human tissue will align stochastically with a strong magnetic field causing Larmor precession [24]. The hydrogen nuclei behave like compass needles that are partially aligned by a strong magnetic field in the scanner. The nuclei will be rotated using radio waves, and they subsequently oscillate in the magnetic field while returning to equilibrium. They emit a radio signal that is detected using antennas (coils) and used for making detailed images after Fourier transformation. The MR signal is sensitive to a broad range of influences, such as chemical surrounding, nuclear mobility, molecular structure, flow, and diffusion. Depending on the tissue or movement of fluids within the area of interest, different levels and processes of relaxation can be captured. MRI is a very flexible technique that provides measures of both structure and function. Through varying different parameters of the imaging protocol, it is possible to manipulate the contrast between the degrees of relaxation.

The imaging process can be viewed as dividing the patient volume into slices, which are then further divided into a matrix of voxels. This localisation is achieved through field gradients. An independent RF signal is then produced from each voxel. Image detail and image noise is determined by voxel size, which should be sized appropriately. Factors such as contrast sensitivity, detail, noise, artefacts, and spatial characteristics of image quality can be adjusted by various protocol factor settings. Therefore, maximum benefit of MRI technology requires well-trained technicians to control the overall process and provide a purposeful image. More importantly and unlike other imaging techniques, MRI does not involve radioactivity or ionising radiation.

1.2. Metals in the MR environment

The effect of magnetic fields involved in the MRI procedure on metallic objects, specifically ferromagnetic materials, is of important safety concern [24]. Ferromagnetic materials may be attracted towards the magnetic bore of the MRI system with great acceleration and force. The magnitude of the force created is proportional to the mass of the object and is also dependent on the proximity of the metallic object to the magnet.

The greatest magnetic field strength is found at the ends of the magnetic bore, allowing for ferromagnetic implants in the patient to be susceptible to the strong field. As a result, the implanted device may become displaced during the entering or exiting of the magnetic bore. Tissue damage may occur if an elongated object is near the vicinity of field. Elongated objects may be torqued along the axis parallel to magnetic field lines. Even weak magnetic field strengths pose risk. Devices such as pacemakers, stimulators, and insulin pumps can be interfered with by a magnetic field.

Additionally, non-magnetic metals may be excellent conductors of electricity. Metallic implants are capable of absorbing radio frequency (RF) energy via induction in the MR environment. The energy deposition into the metallic implants may result in a significant temperature increase of the implant and the surrounding tissue. Since Mg is a metal, Mg-based implants may succumb to this type of heating. Investigations of implant heating have been conducted for materials such as stainless steel [25], deep brain stimulation leads [26], and pacemaker leads [27], in which all resulted in an increase of temperature. However, no reports have been described on heating caused by Mg materials exclusively.

The formation of eddy currents, or localised currents, can also occur in the presence of a magnetic field. Safety guidelines have been created to prevent major patient risk caused by these effects. However, the electrical effects of unlooped conductors, such as rods or wires, are sometimes disregarded. Spark formation across gapped metal objects may occur if through changing magnetic fields a voltage is induced in linear conductors, causing the heating of implanted metallic objects. Resonance phenomena such as standing waves may occur in shorter implants, also resulting in the heating of the conductor ends. For these safety reasons, metallic conductors that are not part of the MR system should not be in near location of the magnet. All patient monitoring equipment must be routed to a safe distance from the magnetic bore. Ultimately, a strong analysis of the effects of metallic implants in a magnetic environment is crucial to ensure the safety of the patient. As far as this review has reached, there have been no documented literature published describing any incident regarding magnesium implants during an MRI procedure.

2. Materials and methods

To begin this review, following the PRISMA guidelines, journal

search engines such as Google Scholar and the Mendeley Web Catalogue were utilised in finding articles relating to the following key terms: magnetic resonance imaging, magnesium implants, biodegradable implants, and artefacts. This initial search began on July 1, 2019. Studies were included if magnesium or magnesium-based implants were involved with MRI as a form of imaging modality. Many magnesium-based implant studies were narrowed down to those which utilised MRI in the investigation. Later, studies that discussed artefacts caused by the implants in the MR environment were analysed. No found studies meeting this inclusion criteria were excluded.

3. Results

3.1. Mg-based implant applications and MRI characterisation

Mg-based implants have been successfully implemented in many fields of clinical research. The following section addresses current applications of Mg-based implants and the role of MRI in each respective study. A summary of findings can be seen in Table 1.

In 2005, Eggebrecht et al. released a case study where a Mg-based stent was implanted into a 54-year-old patient suffering from coronary artery disease. The male patient presented with two-vessel coronary artery disease and stable angina. Treatment prescribed to the patient was the implantation of an absorbable Mg-based stent. The stent was based on a Mg alloy that provided mechanical stability comparable to common SS alternatives. Furthermore, the alloy allowed for controlled complete resorption within approximately two months. To image the stent, x-ray methods could not be utilised as the stent was designed with a percentage of magnesium greater than 90%, resulting in complete radiolucency. However, due to Mg properties, non-invasive follow-up was possible through MRI since the stent produced few metallic artefacts [28]. Contrast-enhanced MR angiography was successfully imaged of the right artery one week after stent implantation. The stented segment is clearly visualised without hindrance of metallic artefacts.

The treatment of chronic osteomyelitis, or bone infection, calls for implantable material with antibacterial properties. A material consisting of Mg and copper (Cu) was proposed by Li et al., in 2016. By testing varying Cu contents (0.05, 0.1, and 0.25 wt %), the group investigated the material's ability to treat methicillin-resistant Staphyloccus aureus-induced (MRSA) osteomyelitis. In-vitro and in-vivo, the biocompatibility and antibacterial capabilities of the material were analysed. MRI was employed in this study to observe the healing process of the bone infection in the left tibias of rabbits at various time periods. Four weeks after MRSA injection, MRI provided visualisation of the cortical bone thickening due to abscess formation, soft tissue swelling, and small amounts of gas production [29]. In combination with other results, the evidence produced from the MR images indicated the potential usage of Mg–Cu alloy material with 0.25 Cu % in orthopaedic infection surgery. It is important to note that x-ray and MRI images were taken throughout this study. Images taken of the Mg implants are indifferent if not clearer when compared to the Ti samples in both imaging modalities.

Mg implants are a load-bearing mechanical alternative to standard Ti and SS-based materials. Today, Mg-based implants can be found in various orthopaedic surgeries where MRI has been applied to assess bone formation, implant degradation, and overall healing post-invasive surgery.

Moreover, implant resorption tracking has been successfully visualised using MRI techniques. Modrejewski et al. analysed the degradation behaviour of Mg alloy screws used in distal metatarsal osteotomies [30]. This was the first clinical study of its kind to focus on implant resorption with an emphasis on MRI analysis as the main imaging method. MRI procedures were administered at 3-, 6-, 12-, and 36-months post-operation with different image sequences seen in Fig. 1. At 3 months, the MRI scans were able to provide identification of partial bone growth between the osteotomy gap. The screw contour was still identifiable due to an obvious signal loss. After 12 months, the residual borders of the osteotomy zone could still be seen. At 36 months, significant signal loss was apparent with the length of the screw no longer identifiable. In this study, Modrejewski et al. accurately employed MRI to track Mg degradation and bone healing.

A case series lead by Gigante et al. investigated the treatment of intercondylar eminence fractures with Mg screws. Current literature debates the traditional treatment of tibial spine avulsion fractures with either the implementation of internal fixation devices (screws) or bone tunnel fixation via resorbable sutures. In this study, Gigante et al. explore a third option of applying resorbable Mg screws that combines the best features of the two previously mentioned techniques [31]. Seven patients underwent MRI examination before and after surgery. MRI was chosen as it is the most reliable in imaging meniscal or ligament injuries and was performed after 6- and 12-months post-surgery to evaluate screw degradation. Images seen in Fig. 2 confirm active healing at the fracture site with complete resorption of the fixation device. At 12 months, MRI assessment revealed complete fracture healing, resorption of screws, and newly formed bone.

To address bone defect repair, Lai et al. formulated a novel Mg-based porous scaffold as a solution to treat steroid associated osteonecrosis in 2019 [32]. The scaffold was created from Mg powder, poly-lactide-*co*-glycolide (PGLA), and β-tricalcium phosphate (β-TCP). The listed elements formed the PGLA/TCP/Mg (PTM) scaffold. The study revolved around the development and testing of the PTM scaffold in-vitro and in-vivo. More specifically, the osteogenic and angiogenic responses of the implant were evaluated in a rabbit model. To assess perfusion function, dynamic contrast-enhanced (DCE-) MRI was employed after 2, 4, and 8 weeks post-surgical implantation. DCE-MRI was utilised to measure the blood perfusion parameter "maximum enhancement" (ME). ME is defined as the maximum percentage of signal intensity increase from a measured baseline signal intensity. DCE-MRI successfully demonstrated a difference in ME between the newly designed scaffold and control groups. When compared to the control, the PTM scaffold promoted greater blood perfusion in early stages. During the study, Lai et al. did not observe any local subcutaneous hydrogen gas cavities. In conjunction with other imaging methods, DCE-MRI results suggested that the PTM scaffold could increase blood perfusion and promote angiogenesis.

3.2. MRI investigations with records of artefact production

Artefacts are observable distortions in MRI images that falsely represent true anatomical measurements. These distortions are produced by perturbations of the static magnetic field and depend on the specific material properties of the implanted device. Moreover, the medical device's magnetic susceptibility characteristic largely affects the distortions generated. Therefore, the evaluation of artefact production is essential when choosing a biomaterial. To date, there has been no investigation on how the production methods of Mg alloys or material preparations affect artifacts in medical imaging explicitly. Table 2 describes the accounts of artefact production in the usage of Mg-based implants.

In 2008, Ernstberger et al. investigated the evaluation of Mg

Table 1
Studies administering MRI techniques on Mg implants.

Year	Author	Study Design	MRI Usage
2005	Eggebrecht et al.	Case study	Contrasted MR-angiography successfully applied
2015	Modrejewski et al.	Case series	Observed bone growth and implant degradation
2016	Li et al.	Comparison study	Observed healing process of bone infection
2018	Gigante et al.	Case series	Evaluated screw degradation
2019	Lai et al.	Prospective study	DCE-MRI observed blood perfusion

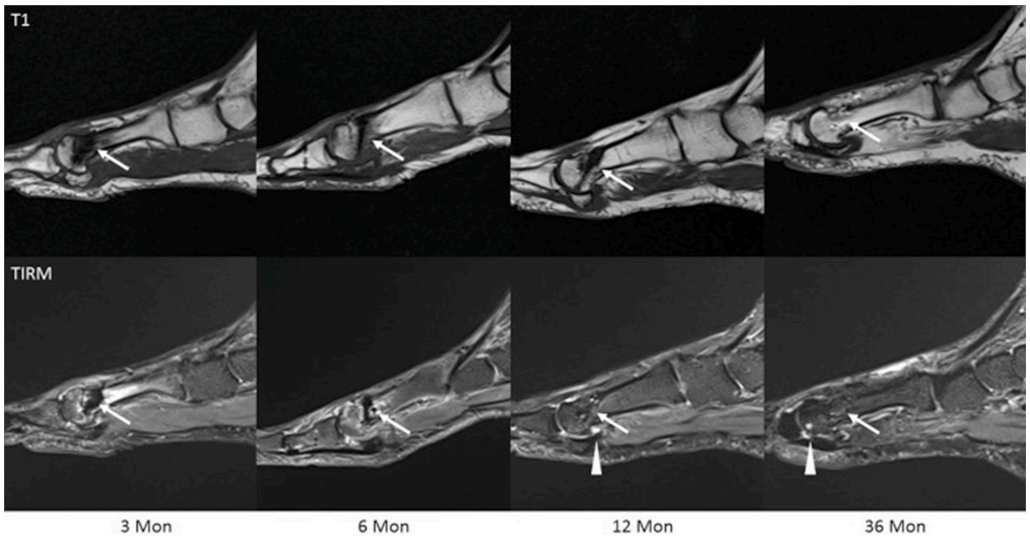

Fig. 1. Sample images of Mg screw implants at different time points with two different imaging protocols, T1 and TIRM. Over time, image artefact reduces as implant degrades. Arrow tips point at joint effusion [30].

compared to Ti and carbon-fibre-reinforced polymers (CFRP) as materials for invertebral test spacers. In particular, the study emphasised artefact production in MRI generated by these materials. Three sizes of each material spacer (nine spacers in total) were implanted into a single Gottingen minipig cadaver spine. The first material was made of TiAl6V4, the second material was made of MgAlMn50, and the third material was made of CFRP which can be seen in Fig. 3. After the MRI was performed, a comparison of artefact production between the sizes and materials was carried out by calculating the total artefact volume (TAV) of each spacer. Using DICOM reader software, the area of the artefacts was measured and multiplied by slice thickness as described by the Debatin multisection slice technique. The MRI evidence revealed the TAV of the Ti-based material to be statistically and significantly greater than the TAV produced by the Mg-based spacers ($p < 0.001$). The Mg-based spacers were also found to produce almost identical artefact behaviours as the CFRP spacers ($p > 0.05$). The authors concluded their study suggesting that spinal implants based on Mg material behave similarly to CRFP devices in MRI scans [33]. However, due to the osseoconductive nature of Mg, implants based on Mg alloys provide an extra asset.

A later study led by Filli et al. analysed the metal-induced artefacts produced by a Mg alloy versus Ti and SS controls. The study focused on the production of these artefacts in computed tomography (CT) and MRI specifically. In the interest of this review, the MRI results of this investigation will be highlighted. Four orthopaedic pins were analysed in this in-vitro study. One pin was made of Ti6Al7Nb, the second was made of SS, and the final two pins were made of MgYNdHRE (two varied diameters). The pins were placed in a phantom filled with CuSO4 solution, presumably to reduce T1 relaxation time. After the MRI scans, the maximum diameter of the artefacts produced by the metallic objects were measured. The experiment revealed that the Mg alloy material produced significantly fewer artefacts than SS ($p = 0.019–0.021$) [34]. Compared to Ti, the Mg alloy produced less artefacts, although not statistically significant. It is important to note however, the biodegradable Mg alloy induced substantially fewer artefacts in CT when compared to the other controls as well.

An ex-vivo trial was carried out by Belenko et al., in 2015 to assess the imaging behaviour of Mg implants. Belenko et al. analysed the Mg-based implants in different imaging modalities and compared the performance to traditional Ti-based implants. A CE-approved Mg-based screw (MAGNEZIX©) and an equivalent Ti screw were imaged with the following modalities: digital radiography (DX), multidetector computed tomography (MDCT), high-resolution flat panel CT (FPCT), and MRI. The materials were not only scanned native but were also implanted into fresh chicken tibia to simulate bone and soft tissue. To measure artefacts in MRI, the diameter of signal loss due to metallic distortion was measured. If multiple artefacts were produced, the longest artefact was chosen. In Fig. 4, the Mg-based screw generated less severe and fewer artefacts when compared to the Ti screw ($p < 0.005$) [35]. Similarly, to the native scans, the ex-vivo assessment revealed the Mg-based screw to be superior to Ti with regards to minor artefact production and signal distortion. Additionally, a metal-artefact reduction sequence technique called WARP was applied to the MRI scans. Unfortunately, the technique was only able to reduce artefacts of the Ti screw with statistical significance ($p < 0.001$). Regardless of this result, Belenko et al. support the use of Mg-based implants as the material produces less artifacts compared to Ti and out-performed Ti in all of the modalities involved in the study. A few years after this trial was completed, extra supportive findings and results were published into a further descriptive research article by Sonnow et al. where the experiments are discussed in greater detail [36].

A paramount study was published in 2017 by Plaass et al. describing the results of a 3-year randomised clinical trial. The clinical trial focused on the application of Mg screws for the treatment of hallux valgus and the comparison of effectiveness against Ti compression screws. The first mid-term study of its kind, Plaass et al. investigated Mg implants for the fixation of distal metatarsal osteotomies. Twenty-six patients with symptomatic hallux valgus were randomly divided into two cohorts where one group was to be treated with the Mg screw while the other was treated with the Ti screw. Clinical follow up was conducted for three years post-surgery. Various clinical tests evaluating range of motion and patient pain were administered throughout the follow-up period. All MRI scans were evaluated for potential presence of metallic debris resulting from implantation to determine any relations between MRI artefact with potential metallic debris from the surgery procedure. MRI was utilised to assess differences in oedema, soft tissue reaction, bone resorption, and bone healing, which revealed no significant difference between the materials. Despite the presence of debris in three of the Mg

Fig. 2. MRI at six months post-operation (top) shows fracture healing and implant resorption. At 12 months (bottom), the fracture is healed, resorption is complete and replaced with new bone-like material [31].

Table 2
Studies describing Mg implant artefact production in MRI.

Year	Author	Implant Type	Artefact Behaviour
2008	Ernstberger et al.	Intervertebral spacer	Reduction compared to Ti spacers
2015	Filli et al.	Pin	Reduction compared to Ti and SS pins
2015/ 2017	Belenko et al./ Sonnow et al.	Screw	Reduction compared to Ti screws
2017	Plaass et al.	Screw	Reduction compared to Ti Screws

patients, metal artefacts were still significantly lower in the Mg-group versus the Ti-group ($p < 0.05$) [37]. Overall, it was reported that an improvement of the significant measures for all tested clinical scores was observed with no statistically relevant differences between the two patient groups. After the 3-year period, the Mg-based screws were found to be fully degraded but not fully remodelled. The authors note that the volume of remodelling zones decreased over time, suggesting that hydrogen gas was not developed too fast to cause any major tissue displacement. More importantly, the authors suggest that Mg should strongly be considered since the material produced less artefact than Ti.

4. Discussion

Literature discussed in this review describes the interaction of Mg-based implants with magnetic fields produced in MRI procedures. As outlined in the various studies, Mg-based implants present a contemporary option to traditional orthopaedic implants due to their bone-like mechanical properties and degradation capability. As MRI does not involve ionising radiation, the imaging modality favours patient health

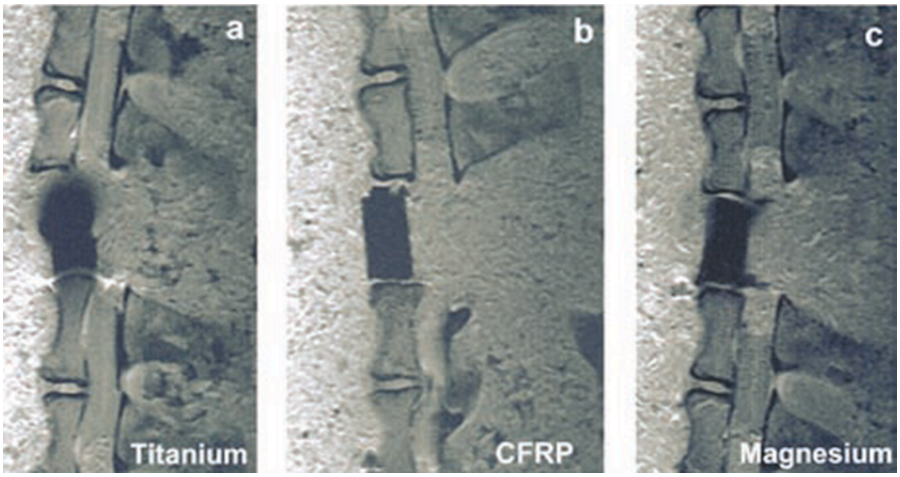

Fig. 3. MRI of various artefact produced by titanium, CFRP, and magnesium [33].

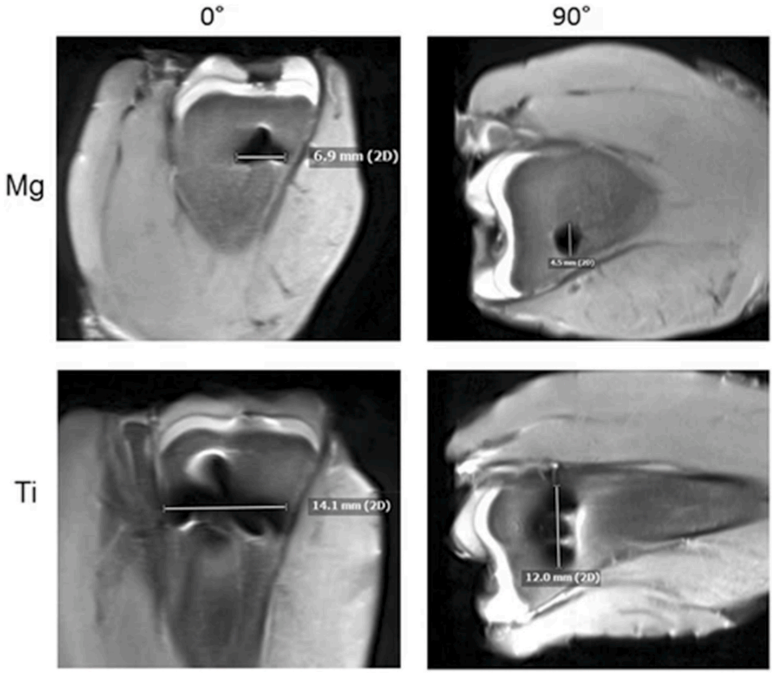

Fig. 4. Artifact production of Magnesium and Titanium in two views of the screw using 3T MRI [36].

and limits long-term effects.

An important characteristic of Mg implants is the radiological viewing of gas release due to material degradation. Hydrogen gas is produced during the corrosion process and though non-toxic, gas production may cause local tissue displacement and temporary gas cavities [38]. Of the studies mentioned in this review, only Li et al., Plaass et al., and Lai et al. successfully observe the presence of gas in their MRI results, or lack thereof. Although no reports on gas formation in their study, Sonnow et al. suggest that future investigations be aimed at further differentiation of air, gas formation, and artifacts around implant site [36]. The ability to observe gas formation around Mg implants promote MRI as a compatible imaging modality.

According to the findings stated in this review, Mg-based implants produce minor artefacts during MRI processes when compared to other commercial equivalent implants. As pointed in Table 2, Mg has shown to produce lower artefacts than Ti. Both materials have paramagnetic properties which cause them to create local magnetic field inhomogeneities. However, the degree in which the materials produce metallic artefact are limited by the magnetic susceptibility of each material. The lower magnetic susceptibility property of Mg reduces these distortions when compared to Ti. The significant benefit of lower artefact production is greater image quality of true anatomical location.

Higher-detailed imaging allows for surgeons and radiologists to accurately provide correct diagnoses. Furthermore, other biodegradable Mg-based supporting structures and geometries come into the focus of medical applications, such as cardiovascular stents. The performance of Mg-based implants relies heavily on the production process, which has major impact on material properties and therefor magnetic field responses. This is an important factor but is outside the scope of this work.

Within the range of MRI application in the development of Mg-based implants, future investigations should emphasise the later stages of clinical translation further. Specific to MRI, the understanding of Mg-based implant heating is necessary to ensure patient safety. Although there have been accounts of artefact description of Mg-based implants, additional qualitative and quantitative metallic artefact investigations are warranted as suggested by mentioned authors which may provide information on implant degradation state. Finally, MRI has shown to provide significant information on soft tissue and should be utilised in addition with other imaging modalities for an overall multimodal analysis of Mg-based implants.

5. Conclusion

The evidence presented in this review warrants further exploration of Mg-based implants in conjunction with MRI analysis. As shown in the findings, MRI is a viable imaging modality. Further in vivo studies are justified to better quantify artefact production caused by Mg in MRI investigations. Implants based on Mg material display adequate behaviour in the MRI environment and yields promising results for future research and clinical applications.

Authors' contributions

Espiritu: Study conception and design, Acquisition of data, Analysis and interpretation of data, Drafting of manuscript, Critical revision. Meier: Acquisition of data, Drafting of manuscript, Critical revision. Seitz: Drafting of manuscript. Critical revision

Declaration of competing interest

Syntellix AG is a medical technology manufacturer of metallic and bio-absorbable clinical implants. Authors Espiritu and Seitz are employed as Research Associate and Director of Research and Development, respectively.

Acknowledgements

This project has received funding from the European Union's Horizon 2020 research and innovation programme under the Marie Skłodowska-Curie grant agreement No 811226.

References

[1] B. Gruber, M. Froeling, T. Leiner, D.W. Klomp, RF coils: a practical guide for nonphysicists, J. Magn. Reson. Imag., Bd. 48 (3) (2018) 590–604.
[2] E. Weidman, K. Dean, W. Rivera, M. Loftus, T. Stokes, R. Min, „MRI safety: a report of current practice and advancements in patient preparation and screening,, Clin. Imag., Bd 39 (6) (2015) 935–937.
[3] M. Prakasam, J. Locs, K. Salma-ancane, D. Loca, A. Largeteau, L. Berzina-Cimdina, Biodegradable materials and metallic implants—a review, J. Funct. Biomater., Bd. 8 (4) (2017) 44.
[4] E.C. Huse, A new ligature, Chicago Med J Exam, 1878.
[5] M.G. Seelig, A study of magnesium wire as an absorbable suture and ligature material, Arch Surg., Bd. 8 (2) (1924) 669–680.
[6] M. Bamberger, G. Dehm, Trends in the development of new Mg Alloys, Annu. Rev. Mater. Res. Bd. 37 (2008) 505–533.
[7] R. Radha, D. Sreekanth, Insight of magnesium alloys and composites for orthopedic implant applications - a review, J. Magnes and Alloys, Bd. 5 (3) (2017) 286–312.
[8] Y. Chen, Z. Xu, C. Smith, J. Sankar, Recent advances on the development of magnesium alloys for biodegradable implants, Acta Biomater. Bd. 10 (11) (2014) 4561–4573.
[9] Y. Zong, G. Yuan, X. Zhang, L. Mao, J. Niu, W. Ding, Comparison of biodegradable behaviors of AZ31 and Mg–Nd–Zn–Zr alloys in Hank's physiological solution, Mater. Sci. Eng.: *B*, Bd. 177 (5) (2012) 395–401.
[10] M.B. Kannan, R.K.S. Raman, In vitro degradation and mechanical integrity of calcium-containing magnesium alloys in modified-simulated body fluid, Biomaterials, Bd. 29 (15) (2008) 2306–2314.
[11] S.K. Lu, H.I. Yeh, T.Y. Tian, W.H. Lee, Degradation of magnesium alloys in biological solutions and reduced phenotypic expression of endothelial cell grown on these alloys, in: 3rd Kuala Lumpur international conference on biomedical engineering, Bd 15, 2006, pp. 98–101.
[12] N. Angrisani, J. Reifenrath, F. Zimmermann, R. Eifler, A. Meyer-Lindenberg, K. Vano-Herrera, C. Vogt, „Biocompatibility and degradation of LAE442-based magnesium alloys after implantation of up to 3.5 years in a rabbit model, Acta Biomater. Bd. 44 (15) (2016) 355–365.
[13] C.H. Ye, Y.F. Zheng, S.Q. Wang, T.F. Xi, und, Y.D. Li, In vitro corrosion and biocompatibility study of phytic acid modified WE43 magnesium alloy, Appl. Surf. Sci., Bd. 258 (8) (2012) 3420–3427.
[14] M. Staiger, A. Pietak, J. Huadmai, G. Dias, „Magnesium and its alloys as orthopedic biomaterials: a review, Biomaterials, Bd 27 (9) (2006) 1728–1734.
[15] H. Brar, J. Wong, und, M. Manuele, „Investigation of the mechanical and degradation properties of Mg–Sr and Mg–Zn–Sr alloys for use as potential biodegradable implant materials, J. Mech. Behav. Biomed. Mater., Bd. 7 (2012) 87–95.
[16] D.F. Williams, The Williams Dictionary of Biomaterials, Liverpool University Press, 1999.
[17] C. Liu, Z. Ren, Y. Xu, S. Pang, X. Yhau, Y. Zhao, „Biodegradable Magnesium Alloys Developed as Bone Repair Materials: A Review, Recent Applications of Scanning Microscopy in Surface Engineering (2018).
[18] M. Bornapour, M. Celikin, M. Cerruti, M. Pekguleryuz, „Magnesium implant alloy with low levels of strontium and calcium: the third element effect and phase selection improve bio-corrosion resistance and mechanical performance, Mater. Sci. Eng.: *C*, Bd. 35 (2014) 267–282.
[19] B. Heublein, R. Rohde, V. Kaese, M. Niemeyer, W. Hartung, A. Haverich, „Biocorrosion of magnesium alloys: a new principle in cardiovascular implant technology? Heart, Bd. 89 (6) (2003) 651–656.
[20] O. Böstman, H. Pihlajamäki, Clinical biocompatibility of biodegradable orthopaedic implants for internal fixation: a review, Biomaterials 21 (24) (2000) 2615–2621.
[21] G. Marcucci, M.L. Brandi, Kyphoplasty and vertebroplasty in the management of osteoporosis with subsequent vertebral compression fractures, Clin. Cases in Miner. Bone Metabol. 7 (1) (2010) 51–60.
[22] H. Hermawan, d. Dube, D. Mantovani, „Development of degradable Fe-35Mn alloy for biomedical application, Adv. Mater. Res. 15-17 (2006) 107–112.
[23] J. Choueka, J.L. Charvet, K.J. Koval, H. Alexander, K.S. James, K.A. Hooper, J. Kohn, Canine bone response to tyrosine-derived polycarbonates and poly(L-lactic acid), J. Biomed. Mater. Res. 31 (1) (1996) 35–41.
[24] P. Sprawls, Magnetic Resonance Imaging: Principles, Methods, and Techniques, Medical Physics Publishing, 2000.
[25] P. Nordbeck, F. Fidler, I. Weiss, M. Warmuth, M.T.E.P. Friedrich, W. Geistert, O. Ritter, P.M. Jakob, M.E. Ladd, H.H. Quick, W.R. Bauer, Spatial distribution of RF-induced E-fields and implant heating in MRI, Magn. Reson. Med. 60 (2) (2008) 312–319.
[26] K.B. Baker, J.A. Tkach, J.A. Nyenhuis, M. Phillips, F.G. Shellock, J. Gonzalez-Martinez, A.R. Rezai, „Evaluation of specific absorption rate as a dosimeter of MRI-related implant heating, J. Magn. Reson. Imag. 20 (2) (2004) 315–320.
[27] G. Calcagnini, M. Triventi, F. Censi, E. Mattei, P. Bartolini, W. Kainz, H.I. Bassen, In vitro investigation of pacemaker lead heating induced by magnetic resonance imaging: role of implant geometry, J. Magn. Reson. Imag. 28 (4) (2008) 879–886.
[28] H. Eggebrecht, J. Rodermann, P. Hunold, A. Schmermund, D. Bose, M. Haude, R. Erbel, „Novel magnetic resonance-compatible coronary stent: the absorbable magnesium-alloy stent, Circulation 112 (18) (2005).
[29] Y. Li, L. Liu, P. Wan, Z. Zhai, Z. Mao, Z. Ouyang, D. Zu, Q. Sun, L. Tan, L. Ren, Z. Zhu, y. Hao, X. Qu, K. Zang, K. Dai, „Biodegradable Mg-Cu alloy implants with antibacterial activity for the treatment of osteomyelitis: in vitro and in vivo evaluations, Biomaterials 106 (2016) 250–263.
[30] C. Modrejewski, C. Plaass, S. Ettinger, F. Caldarone, H. Windhagen, C. Stukenbog-Colsman, C. von Falck, L. Belenko, „Degradation behavior of Magnesium-alloy srews after distal metatarsal osteotomies in MRI, Fuß & Sprunggelenk 13 (3) (2015) 156–161.
[31] A. Gigante, N. Setaro, M. Rotini, S.S. Finzi, M. Marinelli, „Intercondylar eminence fracture treated by resorbable magnesium screws osteosynthesis: a case series, International Journal of the Care of the Injured 49 (3) (2018).
[32] Y. Lai, Y. Li, H. Cao, J. Long, X. Wang, L. Li, C. Li, Q. Jia, B. Teng, T. Tang, J. Peng, D. Eglin, M. Alini, D. Grijpma, G. Richards, L. Qin, „Osteogenic magnesium incorporated into PLGA/TCP porous scaffold by 3D printing for repairing challenging bone defect, Biomaterials 197 (2019) 207–219.
[33] T. Ernstberger, G. Buchhorn, G. Heidrich, „Intervertebral test spacers and postfusion MRI artifacting: a comparative in vitro study of magnesium versus titanium and carbon fiber reinforced polymers as biomaterials, Cent. Eur. J. Med. 4 (4) (2009) 496–500.
[34] L. Fili, R. Luechinger, T. Frauenfelder, S. Beck, R. Guggenberger, N. Farshad-Amacker, G. Andreisek, Metal-induced artifacts in computed tomography and magnetic resonance imaging: comparison of a biodegradable magnesium alloy versus titanium and stainless steel controls, Skeletal Radiol. 44 (2015) 849–856.

[35] L. Belenko, S. Könneker, F. Wacker, C. von Falck, Biodegradable Magnesium Herbert Screw in Different Modalities - Image Quality and Artifacts, European Society of Radiology, 2015.
[36] L. Sonnow, S. Könneker, P.M. Vogt, F. Wacker, C. von Falck, „Biodegradable magnesium Herbert screw – image quality and artifacts with radiography, CT and MRI, BMC Medical Imaging 17 (16) (2017).
[37] C. Plaass, C. von Falck, S. Ettinger, L. Sonnow, F. Calderone, A. Weizbauer, J. Reifenrath, L. Claassen, H. Waizy, K. Daniilidis, C. Stukenborg-Colsman, H. Windhagen, „Bioabsorbable magnesium versus standard titanium compression screws for fixation of distal metatarsal osteotomies - 3 year results of a randomized clinical trial, J. Orthop. Sci. 23 (2) (2018) 321–327.
[38] J.M. Seitz, R. Eifler, F.W. Bach, H.J. Maier, Magnesium degradation products: effects on tissue and human metabolism, J. Biomed. Mater. Res. 102 (10) (2014) 3744–3753.

Chapter 6

Detailing the influence of PEO-coated biodegradable Mg-based implants on the lacuno-canalicular network in sheep bone: A pilot study

In this pilot investigation, we undertake an examination of the impact of a biodegradable material upon the lacuno-canaliculi network (LCN) utilising non-destructive 3D imaging techniques for the first instance. To advance our comprehension of the interrelationship between bone and implants, it is imperative to examine the structural foundation of the LCN and its reaction to surface-modified Mg-based materials. This research endeavours to discern morphological distinctions within the LCN of sheep, particularly in proximity to uncoated and plasma electrolytic oxidation (PEO) coated WE43 screws, through the application of synchrotron-based transmission X-ray microscopy. Our findings reveal that the deployment of PEO-coated materials tends to encourage more favourable lacunar configurations, while the uncoated counterparts promote a more extensive interconnected LCN. Notably, the innovative imaging methodology employed in this study possesses the potential to shed new light on the existing understanding of the interplay between the LCN and biodegradable materials.

The results have been published in the journal *Bioactive Materials* and has been reproduced with permission.

Bioactive Materials 26 (2023) 14–23

Contents lists available at ScienceDirect

Bioactive Materials

journal homepage: www.keaipublishing.com/en/journals/bioactive-materials

Detailing the influence of PEO-coated biodegradable Mg-based implants on the lacuno-canalicular network in sheep bone: A pilot study

Jonathan Espiritu [a,*], Sandra Sefa [b], Hanna Ćwieka [b], Imke Greving [c], Silja Flenner [c], Regine Willumeit-Römer [b], Jan-Marten Seitz [a], Berit Zeller-Plumhoff [b,**]

[a] Syntellix AG, Hannover, Germany
[b] Institute of Metallic Biomaterials, Helmholtz-Zentrum Hereon, Geesthacht, Germany
[c] Institute of Materials Physics, Helmholtz-Zentrum Hereon, Geesthacht, Germany

ARTICLE INFO

Keywords:
Nanotomography
Lacuno-canalicular network
Bone
Magnesium
Biodegradable implants

ABSTRACT

An increasing prevalence of bone-related injuries and aging geriatric populations continue to drive the orthopaedic implant market. A hierarchical analysis of bone remodelling after material implantation is necessary to better understand the relationship between implant and bone. Osteocytes, which are housed and communicate through the lacuno-canalicular network (LCN), are integral to bone health and remodelling processes. Therefore, it is essential to examine the framework of the LCN in response to implant materials or surface treatments.

Biodegradable materials offer an alternative solution to permanent implants, which may require revision or removal surgeries. Magnesium alloys have resurfaced as promising materials due to their bone-like properties and safe degradation *in vivo*. To further tailor their degradation capabilities, surface treatments such as plasma electrolytic oxidation (PEO) have demonstrated to slow degradation.

For the first time, the influence of a biodegradable material on the LCN is investigated by means of non-destructive 3D imaging. In this pilot study, we hypothesize noticeable variations in the LCN caused by altered chemical stimuli introduced by the PEO-coating.

Utilising synchrotron-based transmission X-ray microscopy, we have characterised morphological LCN differences around uncoated and PEO-coated WE43 screws implanted into sheep bone. Bone specimens were explanted after 4, 8, and 12 weeks and regions near the implant surface were prepared for imaging. Findings from this investigation indicate that the slower degradation of PEO-coated WE43 induces healthier lacunar shapes within the LCN. However, the stimuli perceived by the uncoated material with higher degradation rates induces a greater connected LCN better prepared for bone disturbance.

1. Introduction

An expanding market for new implants has been established as a response to an increase in orthopaedic surgeries. Surgical intervention requiring bone implants aim to create direct contact between implant material and bone. How this contact which is influenced by bone reorganization and remodelling is generally studied as well as a deeper understanding of bone healing around modern implant materials and technologies is unclear.

Bone is a hierarchical material that requires studying at several scales with each hierarchical level containing significant information. Macro-to micro-scale investigations are conducted to study the bone-to-implant interface and bone volume to total volume in order to assess the overall osseointegration of the implant [1,2]. Scaling further to the nanoscale, the study and imaging of bone cell arrangement can be achieved [3]. The most abundant bone cell type [4], osteocytes, are dispersed throughout the mineralized extracellular matrix (ECM) and are critical to bone forming and remodelling processes [5]. Mature osteocytes are situated in a highly connected system named the lacuno-canalicular network (LCN). Entrapped in the lacunae, osteocytes are connected through dendritic channels called canaliculi in which they establish communication. Recently, canalicular junctions (CJ) have

Peer review under responsibility of KeAi Communications Co., Ltd.
* Corresponding author. Syntellix AG, Aegidientorplatz 2a, Hannover, 30159, Germany.
** Corresponding author. Helmholtz-Zentrum Hereon, Max-Planck-Strasse 1, Geesthacht, 21502, Germany.
E-mail addresses: espiritu@syntellix.com (J. Espiritu), berit.zeller-plumhoff@hereon.de (B. Zeller-Plumhoff).

https://doi.org/10.1016/j.bioactmat.2023.02.018
Received 15 November 2022; Received in revised form 31 January 2023; Accepted 14 February 2023
Available online 20 February 2023

shown to play a significant role in the LCN and have also been investigated [6]. The LCN enables biochemical signal communication between osteocytes and the transportation of nutrients [4]. Osteocytes locally initiate bone remodelling by generating signals in response to mechanical stimuli in the form of shear stress due to the flow of the extracellular fluid (ECF). Bone deformations are perceived by osteocytes and transduced into a signal which is transmitted to the rest of the network [7], triggering the recruitment of osteoblasts and osteoclast precursor cells [8]. Besides the mechanosensory capabilities of osteocytes, ECF found in the LCN enables mineral exchange with ECM [9]. Damage to the LCN or reduction in the LCN surface area may in turn impair mineral mobilisation and the mechanotransduction properties of osteocytes. Reduced interconnectivities hinder osteocyte communication and bone remodelling [10]. Irregular LCNs have been associated with bone diseases such as osteoporosis, osteoarthritis, and osteomalacia [11]. Furthermore, sex and age-related changes have been reported to show a decrease of lacunae density and loss of canaliculi, altering communication within the LCN [10,12]. Therefore, disruption to the LCN due to bone damage or implantation of (stimulating) biomaterials warrants further investigation.

Today, orthopaedic implants are used to replace or support damaged bone. However, traditional implant materials have shown to introduce unwarranted inflammatory responses [13] and further refracture risks [14]. Magnesium (Mg) and Mg-based alloys have re-emerged as promising alternative implant materials due to their successful degradation performance *in vivo* [15]. The similar elastic modulus and densities between Mg-based alloys and natural bone negate negative mechanical defects such as stress-shielding [16,17]. Though successful clinical cases have been reported using Mg-based alloys as implant material [18–22], additional research in potential surface treatments to further optimise degradation capabilities of Mg is on-going.

An inherent characteristic of pure Mg implants is fast degradation accompanied by hydrogen gas accumulation. This build-up of gas may lead to mechanical instability and consequently ineffective implantation. To overcome this, one surface treatment in particular, plasma electrolytic oxidation (PEO) has shown to lower the degradation rate of non-treated Mg-based implants [23–26]. Furthermore, PEO treatments surpass other surface technologies by producing thicker coatings, excellent adhesive strength, and can be applied to complex geometries [27]. By augmenting the degradation capabilities of these alloys further, Mg-based implants could potentially address other indications and fracture types which may require a more tailored degradation rate. Although there have been investigations of the LCN near permanent materials such as titanium [28], there is no documentation of LCN characterisation around biodegradable material.

Advancements in synchrotron-based imaging allows for better time effective imaging, without compromising imaging capabilities or sample damage. Characterising the structures found in the LCN has been challenging to date, as imaging requires a relatively large field-of-view and spatial resolutions below 100 nm. Human lacunae have previously been reported to have an average surface area of 20–70 μm^2 [29]. Canaliculi have been described to have an average diameter of 100–600 nm [30,31], being much more difficult to resolve. Previously, the LCN has been characterised with various imaging modalities. (Quasi) two-dimensional methods including light [32], scanning electron [33–36], and transmission electron microscopy [30,37–39] have been utilised to image LCN structures though limited due to penetration depth and challenging sample preparation. Confocal microscopy [6,7,10,40,41] has also been applied, though with limited field-of-view. By comparison, X-ray and synchrotron radiation-based methods including ptychography, transmission X-ray microscopy (TXM) and near-field holotomography are enabling studying the LCN at high resolutions non-destructively in 3D with a relatively large field-of-view [3,6,9,42–47]. Though laboratory sources may provide similar spatial resolutions, synchrotron radiation increases imaging speed with comparable or better image quality [48]. In this investigation, synchrotron radiation-based X-rays are conditioned by a double crystal monochromator and are further shaped by a condenser onto bone specimen. Behind the sample, Zernike phase rings are placed to attain qualitative phase contrast before images are captured with an X-ray camera.

In addition to the lack of LCN characterisation around degraded Mg-based implants, there is currently no information on the influence of PEO coating technologies on LCN morphology. As such, it is integral to understand the relationship between the PEO coating of Mg-based screws and the LCN to ensure successful implantation and controlled degradation. Two types of materials are analysed in this investigation, an untreated WE43-based magnesium alloy and a PEO surface-treated WE43-based magnesium alloy. The aim of this investigation is to provide a proof-of-concept study regarding the influence of PEO coatings on Mg-based screws implanted into sheep bone by characterizing the LCN at the nanoscale level in 3D using synchrotron radiation-based TXM. We hypothesize that the changed degradation rate induced by the PEO coating results in an altered chemical stimulus perceived by the LCN. This altered stimulus may lead to a change in LCN arrangement or morphology leading to variations in bone remodelling.

2. Materials and methods

2.1. Implant material

Orthopaedic interference screws (Fig. 1) with a diameter of 6 mm and 20 mm length were analysed in this investigation. Two types of materials manufactured by Syntellix AG (Hanover, Germany) were evaluated in this study: an untreated WE43-based magnesium alloy and a PEO surface-treated WE43-based magnesium alloy with a layer thickness of approximately 10–30 μm. Furthermore, the WE43 alloy is composed of Mg with the addition of Yttrium (3.7–4.3 %), Rare Earth Elements (2.4–4.4 %), and Zirconium (0.4 %) [49]. The specific composition and production methods for the alloy used in this investigation have been patented by Syntellix AG [50].

2.2. Animal experiments

Animal experiments were provided ethical clearance by the Landesamt für Arbeitsschutz, Verbraucherschutz und Gesundheit von Brandenburg (ethical clearance number 2347-31-2016). Bone specimens were explanted from the hind legs of three sheep (female German Heath, at least 2 years of age) with body weights between 43 and 57 kg. Each sheep received two screw implants, one made of WE43 and the other a

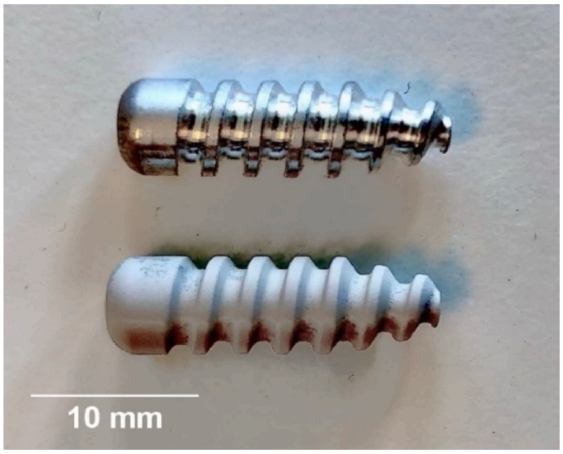

Fig. 1. Uncoated (top) and surface treated (bottom) WE43 orthopaedic interference screws manufactured by Syntellix AG (Hanover, Germany).

PEO-coated WE43 implant in either the distal femur or the proximal tibia. Implant material were spread among implant sites in such a manner that not only one specific material was placed in one site. The surgical methodology and selected time frames were chosen due to its acceptance for biological testing and evaluation of medical devices as set out by EN ISO 10993–6:2007 [51].

Before implantation, the animals were sedated intramuscularly with 0.4 mg/kg diazepam followed by general anaesthesia of 10 mg/kg ketamine. Shaving, cleaning, disinfection, and sterile covering of both knees took place before incisions. For tibial implantation, the skin was incised medial on the proximal end of the tibia exposing the shaft of tibia. The periosteum on the medial surface was then prepared. For femoral implantation, an incision was made medial on the distal end of the femur. The femoral trochlea and medial condyle were exposed and the caudomedial end of the trochlear crest was further prepared. At both implantation sites, a drill with 6 mm diameter was applied to a depth of approximately 20 mm. The application of interference screw was then achieved by means of screwdriver. Wounds were closed with continuous fascia and subcutaneous sutures, and with continuous intracutaneous suture skin bonding.

Butorphanol (0.5 mg/kg) was administered as prophylactic analgesia for a period of minimally three days *post operationem*. The animals were housed in groups during the acclimatization as well as during the study period. Individual times of postoperative recovery were ensured. Straw was used for bedding, supplied fresh and sufficiently on a weekly basis as well as if required. The sheep were provided with drinking water and ad libitum. After either four, eight, or twelve weeks of healing, the animals were sedated and put under general anaesthesia as described previously, followed by T61 intravenous euthanization.

2.3. Sample processing and data acquisition

Following euthanization, the implantation sites including the implanted screws were extirpated preserving adjacent bone tissue with at least 2 cm distance to the specific test item for a total of 6 explants. The samples were placed in increasing percentages of ethanol (Herbeta Arzneimittel Detlef Karlowski e.K., Berlin, Germany) for eight weeks. Following dehydration, the samples were embedded in polymethyl methacrylate (Kulzer GmBH, Hanau, Germany) and sliced in half along the length of the screw for further study.

2.3.1. Micro-computed tomography (μCT)

The embedded samples were first imaged via a laboratory μCT (Phoenix Nanotom by Baker Hughes, Celle, Germany) with an operating voltage of 100 kV at 70 μA current resulting in a pixel size of approximately 6 μm. Scanning was completed with 1000 ms exposure time with 2400 projections. Scans were reconstructed in Datos|x (Baker Hughes, Celle, Germany) where any movement during the scan was corrected using the image optimisation function. Imaging data acquired from μCT scans were then utilised for degradation rate calculations.

2.3.2. Scanning electron microscopy

Following μCT scanning, the embedded samples were cut perpendicular to the screw's long axis approximately 10 mm from the head of the screw using a diamond wire saw (Well Diamond Wire Saws SA, Mannheim, Germany) based on previous μCT scans. The exposed samples were then subject to polishing. Firstly, samples were cleaned with ethanol prior to and after mechanical polishing (Diamant suspension, with particle size 3 μm for 7 min). After cleaning, the quality of polishing was verified using a light microscope. The samples were then sputtered with gold for 1 min via a CRESSINGTON sputter coater (TESCAN GmbH, Dortmund, Germany). The sputtered samples underwent scanning electron microscopy (SEM). The TESASCAN AMBER X (TESCAN GmbH, Dortmund, Germany) was used to image the samples with a current of 10 pA and an applied voltage of 10 kV. A 300 μm field-of-view was achieved with an image size of 1024 pixels by 1024 pixels. Following SEM imaging (Fig. 2), two regions of interest from the trabecular bone from each explant (millimetres from the screw surface) were selected for further processing. A further region was selected a larger distance from the screw surface to benchmark as undisturbed bone.

2.3.3. Synchrotron radiation-based transmission X-ray microscopy (TXM)

Bone specimens with a diameter and height of 50 μm were subject to focused ion beam milling at Fraunhofer Institute for Integrated Systems and Device Technology (Erlangen, Germany) producing a total of 18 samples (2 regions of interest approximately 150 μm from the bone-implant interface and 1 region at a distance of at least 1.3 mm per explant). The samples were mounted onto a custom holder. Following the milling process, imaging was performed at the nanotomography end station at the P05 imaging beamline operated by Helmholtz-Zentrum Hereon at the PETRA III storage ring at the Deutsches Elektronen-Synchrotron (Hamburg, Germany) [52]. An energy of 11.2 keV was selected using a Si111 double crystal monochromator ($\Delta E/E \sim 10^{-4}$). The sample was illuminated using a 1.8 mm beam shaping condenser with square fields of 50 μm by 50 μm, providing an illumination of the same size in the sample plane. The objective lens was a Fresnel zone plate with a diameter of 150 μm and an outermost zone width of 50 nm. Zernike phase rings were placed in the back-focal-plane of the Fresnel zone plate to enable phase contrast imaging. All optics were designed and fabricated in the X-ray Optics and Applications group of the Paul-Scherrer-Institut (Switzerland). The X-ray camera, a Hamamatsu C12849–101U camera with a sCMOS chip with 6.5 μm physical pixel size and a 10 μm Gadox scintillation layer, was placed 19.45 m behind the sample. With these optics, camera and distances, an effective field of view of roughly 46 μm with an effective pixel size of 22.8 nm was achieved. Image reconstruction was performed using respective TomoPy pipelines [53] with binning factor 2 of the raw images, resulting in a voxel size of 45.6 nm.

2.4. Degradation rate

μCT data was loaded into Fiji/ImageJ [54] for post-processing. Anistropic diffusion was applied to reduce noise before applying thresholding techniques to the data, segmenting the bone and implant material in Avizo (Version 2021.1, Thermo Fisher Scientific, Waltham, USA). Degradation rates were determined for both materials based on the segmented data using the following equation [55]:

$$Degradation\ rate = \frac{Initial\ volume\ of\ base\ material - corroded\ base\ volume}{Surface\ area\ of\ initial\ base \times time\ in\ years}$$

2.5. Calculation of lacunar density based on SEM images

SEM data underwent gaussian filtering within Fiji/ImageJ to prepare for segmentation and lacunae quantification. In Avizo, the implant was dilated by 1 mm and was subtracted from the original image to capture the region of interest. The bone within the region of interest was segmented by thresholding techniques to determine the surface area. After, the region of interest was exported from Avizo and loaded into Fiji/ImageJ where the multiple object selection tool was utilised to manually count the lacunae. Finally, the lacunar density was determined by dividing the counted lacunae by the surface are of bone which was previously segmented.

2.6. LCN segmentation

Before segmentation, the SRTXM data was first denoised by an iterative non-local means filter [56] designed to remove texture caused by back projected noise and artefacts in high resolution tomography. The denoised data was then subjected to segmentation in Avizo.

Firstly, the bone and LCN including the canaliculi, canalicular junctions, and lacunae structures were segmented using greyscale

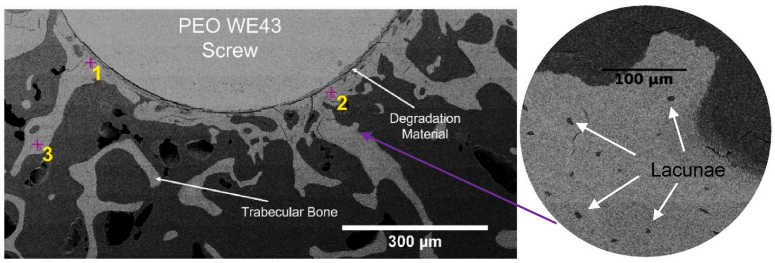

Fig. 2. Example cross section SEM image of PEO surface-treated screw samples after 12-weeks of implantation. Residual WE43 material, degradation layer, and trabecular sheep bone are visible. Two near regions (positions 1 and 2) and one further region (position 3) of interest are marked with crosses for milling. An example magnification of the SEM image showing lacunae is also shown (right), allowing for lacunar density to be derived from the image.

thresholding and manual correction. To segment the lacunae in Fig. 3, the LCN was masked and eroded to remove the canaliculi structures. The remaining structures were then labelled separately and were followed by volume size filtering to ensure only the lacunae were left and canalicular junctions were removed. Finally, the remaining objects were dilated to their approximate original shape followed by manual correction. To segment the canaliculi and canalicular junctions, the lacunae were subtracted from the LCN mask. Moreover, the LCN label was skeletonised for further nodal analysis.

2.7. Quantitative analysis of the LCN

Quantitative analysis was completed in Avizo. The lacunae were quantified by the number of lacunae found in the sample (Lc.N), the total volume of the lacunae (Lc.TV), the bone volume (BV), the density of the lacunae (Lc.N/BV) and the lacunar porosity (Lc.TV/BV). Additionally, the morphology of the lacunae was calculated in terms of sphericity and smoothness (or compactness) using the following equations:

$$Sphericity = \frac{\pi^{\frac{1}{3}}(6 \times Volume)^{\frac{2}{3}}}{Surface\ area}$$

$$Smoothness = \frac{Surface\ area^3}{36 \times \pi \times Volume^2}$$

The canaliculi were quantified by measuring the canalicular total volume (Ca.TV) and the canalicular porosity (Ca.TV/BV). To make better use of partially cut-off lacunae in the measured samples, the average number of canaliculi per lacunar surface area was also calculated. The canalicular junction density (CJ.N/BV) was determined by analysing the skeletonization nodes of the LCN. With the addition of lacunar volume, the total volume of the LCN (LCN.TV) and the LCN porosity (LCN.TV/BV) could be evaluated. Distance mapping was utilised in Avizo to calculate the distance between a matrix voxel and an LCN voxel (d_{LC}). Furthermore, the Fiji/ImageJ plugin [54], MorphoLibJ [57], was used to determine the average distance of any canalicular point to the nearest lacunae (d_{net}) by means of geodesic distance mapping.

3. Results

3.1. Degradation rates

An example of a 3D rendered explant with segmented bone and screw material can be seen in Fig. 4 (A). At 4-weeks, the degraded PEO-coated screw shows good bone contact with signs of degradation more noticeably at the tip. Calculated *in vivo* degradation rates for the uncoated and PEO-coated material are plotted for four, eight, and twelve weeks in Fig. 4 (B). Both samples revealed degradation rates lower than 1 mm/year during the first month, decreasing as time persists. Moreover, the PEO-coated material exhibited a more consistent and lesser degradation rate overall. There is approximately a 50% decrease in degradation rate initially, reducing to approximately 20% at 12 weeks between the two materials.

3.2. Qualitative comparison

Following µCT imaging, regions of interest within the bone surrounding the implant were identified for TXM in scanning electron microscopy (SEM) images of the same cross-section. Additionally, the lacunar density (Fig. 5) was calculated by segmenting the bone area imaged by SEM and manually counting the number of lacunae which were within 1 mm of the implant surface. The bone implanted with PEO material revealed to have approximately 30% lower lacunar density surrounding the implant when compared to the uncoated material.

Fig. 6 illustrates the image segmentation of the selected region of interests near the implant imaged using TXM organised by material and *in vivo* degradation time. The 3D renderings of segmented data show the lacunae (variously coloured) and canaliculi (light blue). From visual inspection, more lacunae were captured in the PEO samples. However, the lacunae found near the uncoated material appear larger in volume. There are clear differences in the organisation of canaliculi in terms of

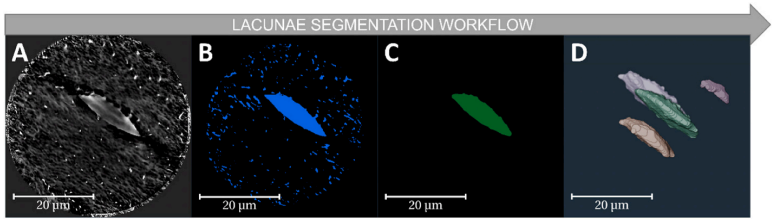

Fig. 3. Sample data workflow of lacunae segmentation in Avizo. A) Denoised TXM image of bone sample showing LCN structures. B) Initial LCN segmentation after greyscale thresholding and manual correction. C) Partially eroded structures with component labelling after smaller volumes are removed. D) Final volume rendering of multiple lacunae after reversing erosion (dilation).

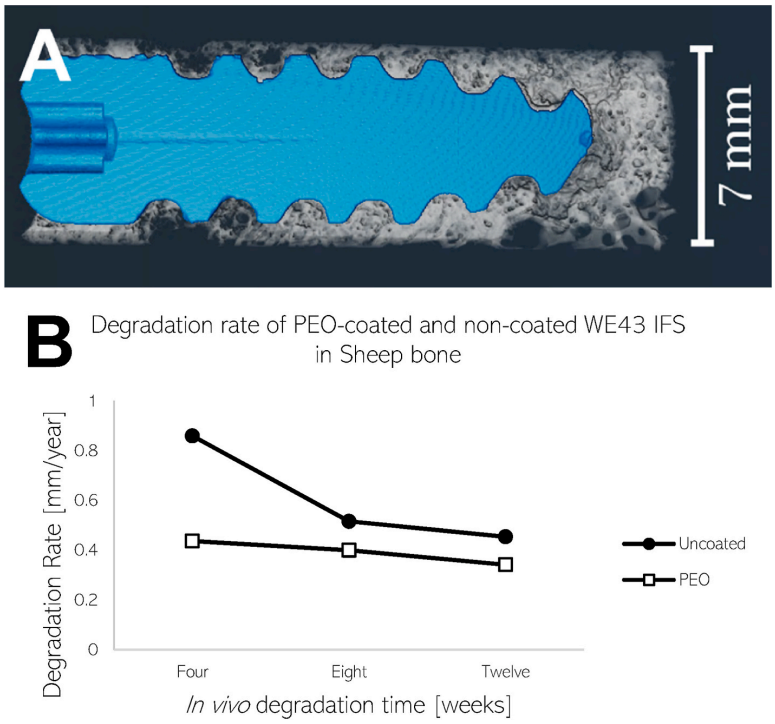

Fig. 4. A) 3D rendering of a 4-week degraded PEO-coated screw surrounded by trabeculae bone created in Avizo. Non-degraded WE43 material is segmented in blue and surrounding non-metallic material in white (bone and degradation layer). B) In vivo degradation rates of uncoated and PEO-coated screws after 4, 8, and 12 weeks calculated from segmented μCT data.

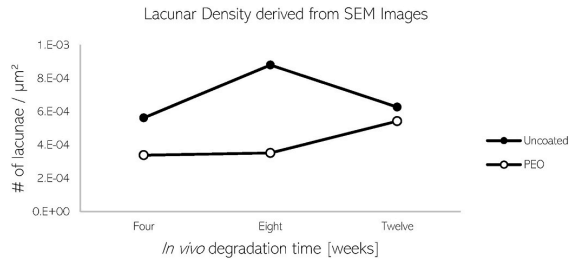

Fig. 5. Calculated lacunar density of uncoated and PEO-coated screws after 4, 8, and 12 weeks calculated from SEM images.

direction seen in the different time points. Thicker and irregular canaliculi are more apparent at 8 weeks of *in vivo* degradation.

3.3. Quantitative analysis of the LCN morphology

Based on the segmented data of the LCN, a quantitative analysis of the network structure was performed. The following figures describe results of the two bone samples found near the implant. Results based on the third sample further from the implant can be found in the Supplementary Material.

Reported values of lacunar porosity and density are depicted in Fig. 7. The lacunar volume in both LCNs found near the implant materials comprises of less than 4% of the total bone volume between four and twelve weeks. From eight to twelve weeks, the lacunar porosity of the LCN surrounding the uncoated material is greater than the selected LCN near the PEO-coated material. However, an elevated lacunar density near the PEO-coated material is seen during this time period. Bone analysed further away from the uncoated implant revealed a lower average lacunar porosity and density, relative to PEO-coated material.

Lacunar morphology in terms of sphericity and smoothness were investigated for the segmented lacunae. Two general classifications of shapes were found in the bone specimen: smooth and irregular. The lacunae were averaged for each time-point and plotted in Fig. 8. The lacunae found near the PEO-coated implant exhibited a smoother and ellipsoid-like shape in contrast to the irregular-shaped lacunae found near the uncoated material at the analysed time points. Lacunae analysed further away from the implant surface overall display a round and healthy lacunar shape during early time points and decline in smoothness and regularity towards shapes found near the implant as time progresses.

In terms of canalicular structures, the porosity and average number of canaliculi per area of lacunae found near the implant surface are described in Fig. 9. During all time-points, the canaliculi made up a higher percentage of the total bone volume found near the uncoated material, with maximum values at eight weeks. Additionally, a lower number of canaliculi were found attached to lacunae near the PEO implant. With regards to the bone samples further from the implant surface, the canicular presence in terms of porosity and number of canaliculi per area of lacunae was elevated in the bone implanted with uncoated material.

The canalicular junction density and overall LCN porosity of the bone samples located near the implant are shown in Fig. 9. During all observed time-points, the canalicular junction density was elevated in the LCN found near the uncoated material, climaxing at 8 weeks. The total volume of the LCN found around the PEO-coated material was

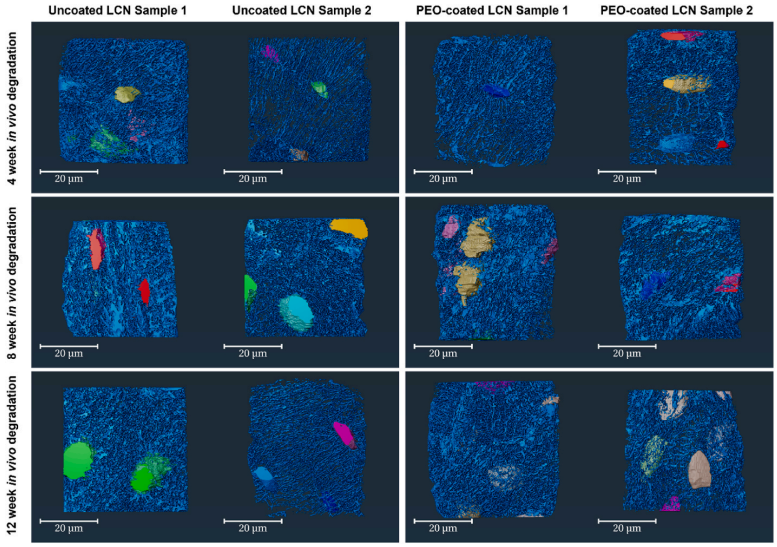

Fig. 6. 3D renderings of the LCN in sheep bone near uncoated and PEO-coated WE43 implants organised by *in vivo* degradation time and material. Renderings were segmented in Avizo highlighting lacunae (colors are for visualization purposes only) and the canaliculi (light blue) for bone specimen after 4, 8, and 12 weeks. Two samples per material were selected for each time-point.

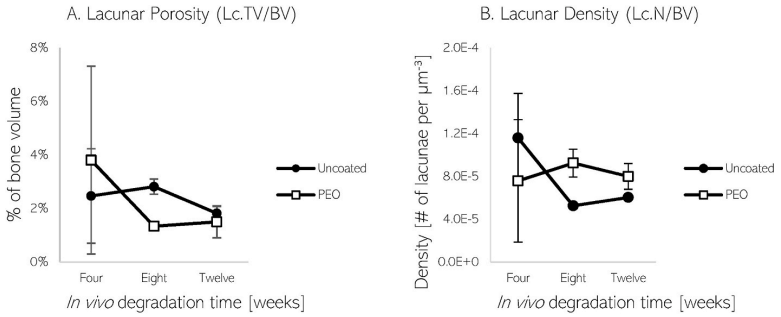

Fig. 7. Plots of lacunar porosity or percentage of lacunar volume in bone (A) and lacunar density (B) of LCN near uncoated and PEO-coated Mg implants after 4, 8, and 12 weeks.

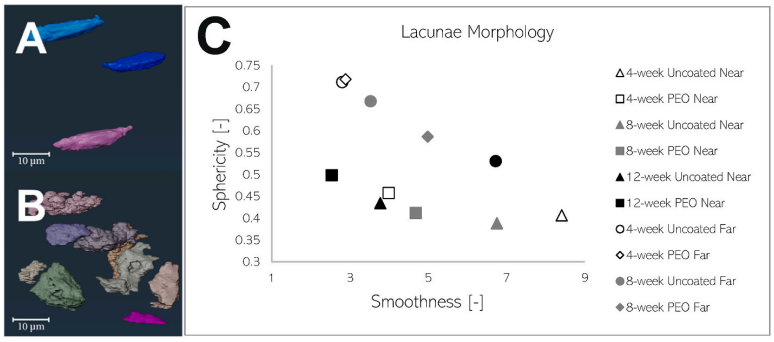

Fig. 8. *3D renderings of sheep lacunae found at 12 weeks* (A) and *4 weeks* (B) *near non-coated WE43 screw samples. Plot (C) describes the average morphology of lacunae found in the LCN near and further away uncoated and PEO-coated WE43 implants in sheep bone. The x-axis describes smoothness or compactness (unitless) of lacunae shape, where a value of 0 corresponds to perfect smoothness. The y-axis describes the sphericity (unitless) of the lacunae shape, where a value of 1 corresponds to a perfect sphere. Samples "near" the implant were selected mms from implant surface, while "far" samples were selected further from the implant surface from undisturbed bone.*

observed to be generally lower. At further distances, the canicular junction density was found to be greater in the bone implanted with non-coated material, but still lower in overall LCN porosity when compared to PEO-coated implanted material.

As a measure of LCN functionality, its transport efficiency can be assessed. Kollmannsberger et al. describe transport efficiency as the time

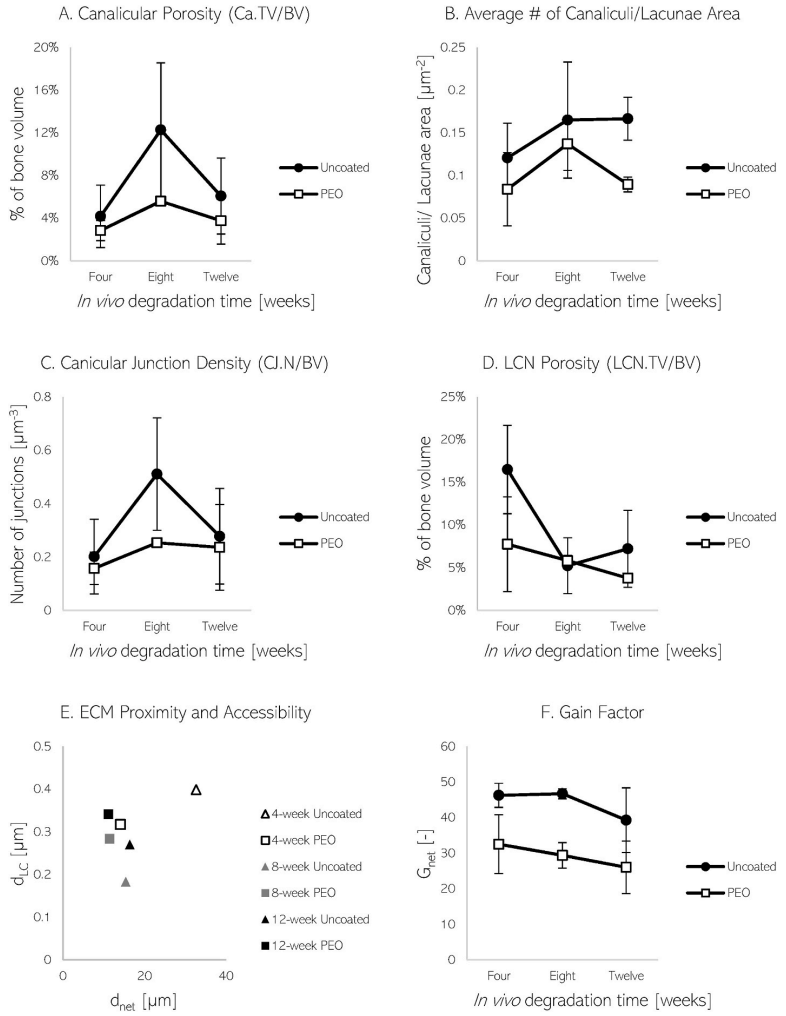

Fig. 9. Plots of canaliculi porosity or percentage of canalicular volume in bone (A), average number of canaliculi per area of lacunae (B), canalicular junction density (C), and LCN porosity or volume (D) near uncoated and PEO-coated WE43 implant material after 4, 8, and 12 weeks. Additionally, the ECM proximity, accessibility (E) and gain factors (F) of bone near uncoated and PEO-coated WE43 implants over time are shown. Parameters d_{LC} denotes LCN distance to matrix voxel, d_{net} denotes average canalicular distance to neighbouring lacunae, and G_{net} is the gain factor.

required for ECF to travel between the osteocytes and ECM, with the assumption that time is proportional to distance. The transport efficiency between the osteocytes and ECM due to the LCN can be described by the gain factor, G_{net} [7]:

$$G_{net} = \frac{d_{LC} + d_{net}}{d_{LC} + \frac{1}{k} \times d_{net}}$$

It is determined by calculating the average 3D Euclidean distance between the LCN and an ECM voxel (d_{LC}), and the average longest distance within the canaliculi to reach the nearest lacunae (d_{net}) where k is the ratio of $v_{network}/v_{matrix}$. A value of $k = 100$ was chosen since the diffusion coefficient of small molecules through bone matrix is approximated to be at least 100 times smaller than for diffusion through the LCN, as described by Kollmannsberger et al. [7].

The LCN near the implant surface of both materials show similar average distances from the ECM (Fig. 9, E). However, there is a much larger variability in ECM proximity and accessibility in terms of d_{LC} and d_{net} seen in the LCN near uncoated samples. The calculated gain factors of the material over the specified time points are shown in Fig. 9 (F). Both materials depict a downward trend in gain factor as time persists. However, the uncoated material exhibiting higher gain overall. No clear differences between the different implant material were noticed in the ECM proximity of bone further away from the implants. However, the d_{net} was shorter in comparison to bone analysed by the implant. Moreover, the bone further away produced lower Gain Factors when compared to the bone analysed near the implant.

4. Discussion

In this investigation, we report the application of TXM to characterise the LCN morphology of woven sheep bone in the vicinity of implanted biodegradable material for the first time. As discussed, the reactive nature of Mg may lead to rapid degradation rates which do not allow for proper tissue healing, causing overall clinical implication.

As implant degradation occurs, mechanical loading on the implant and surrounding tissue changes as the base metallic material decreases. The rate in which the implant degrades determines how the mechanical loading is distributed throughout the ECM at a specific time, and in turn the shear stress of fluid flow within the LCN from loading. Additionally, the varying degradation rates result in different chemical stimuli sensed

by the osteocytes which may also influence LCN morphology. From our μCT data, a 32% decrease in average degradation rate is exhibited over the selected time points in uncoated samples. This decrease is seemingly low, however, since PEO-coatings have exhibited a reduction in degradation rates by up to 90% and show generally lower degradation rates [58]. With a slower degradation rate introduced by PEO, geometries requiring more material may be produced without risk of premature degradation, such as plates and corresponding screws [23]. Additionally, with a slight increase in implant diameter created by the PEO process described in the methodology, implant stability may improve [59].

Based on SEM imaging, we were able to calculate the lacunar density within 1 mm of the implant material. A higher lacunar density, which has demonstrated to increase nutrients exchange [9], was observed around the uncoated material. An increased lacunar density may have developed as a response to the faster degradation of the uncoated material. With rapid degradation of the uncoated material, a higher amount of nutrients may need to be extracted from the ECM and transported via ECF to initiate bone remodelling processes. As such, the higher lacunar density found around the uncoated material may be aiding in such processes, which may yet to be sensed by the bone surrounding the slower degrading PEO-coated material.

Lacunar morphology has previously been investigated to characterise bone diseases [10–12]. From Fig. 8, a greater portion of imaged lacunae surrounding the PEO material is plotted near the top-left quadrant of the graph, describing the lacunae as rounder and smooth. In comparison, the lacunae surrounding the uncoated material was plotted on the right half of the graph due to their irregularity in shape. The smoother ellipsoidal lacunar shapes found in bone surrounding the PEO-coated material could suggest that lower degradation rates favour lacunar ellipsoidicity. As a result, bone remodelled around the PEO-coated material might be more resistant to micro-damage and micro-cracks as investigated by Liu et al. [34]. Furthermore, smooth ellipse lacunar shapes were determined to be more prominent in mature bone post-operations [60]. With regards to the influence of time, both coated and uncoated bone samples near the implant begin to increase in smoothness as time persists. In contrast, lacunae located further from the implant surface shared smoothness and roundness with that of undisturbed lacunae shape at earlier time points. As time persisted however, the further lacunae begin to increase in irregularity, as seen in Fig. 8c, which may be suggestive of the distance influence between lacunae and implant surface. Regarding lacunar density, a higher number of lacunae in bone is found near the PEO-coated sample after eight weeks. A slower degradation of material caused by the PEO-coating may in turn promote higher density of lacunae. A denser lacunar count might indicate a higher exchange rate of nutrients between the ECF and ECM at lacunar sites, as suggested by Hesse et al. [9].

We found a greater interconnectivity and canalicular presence in the LCN is seen near the uncoated WE43. Furthermore, canalicular porosity and CJ density were higher during all time points, peaking at eight-weeks of degradation. The higher canalicular presence, interconnectivity and higher variability in ECM proximity and accessibility may be indicative of the LCN response to higher degradation rates. Although in our results a higher gain factor may be associated with higher canalicular interconnectivity in our findings, previous studies have found contrary results. Structural quantification of the LCN found in ovine bone has only been documented once in literature. Kollmannsberger et al. analysed the healthy LCN of different mice and sheep bones regarding intercellular transport and communication during a single time-point [7]. The slower-growing sheep bone was found to have lower interconnectivity, however, better organised when compared to the irregular fast-growing mouse bone. By visual inspection, the sheep bone exhibited regular spacing unlike the irregular mouse bone. The analysis revealed a denser canalicular network in sheep bone, greater access to ECM, and gain factors almost double the amount in the mouse bone. However, the study was conducted using confocal microscopy with voxel sizes of only 200 nm, which may have been a leading cause for the sparse network observed in mice as indicated by the study by Yu et al. which showed that high spatial resolution is required for the most accurate results [3].

When considering the bone samples selected further away from the implant surface, there is a lower canalicular presence and connectivity when compared to bone samples near the implant. In conjunction, the Gain Factor of bone further from the implant was determined to be lower than bone located closer to the implant surface. Casanova et al. have described a progressive increase in connectivity of the LCN during fracture healing in mice during early stages of repair [60], which does not seem to be present at the bone samples further from the implant surface. The lower transportation efficiency and network connectivity observed in distant bone analysed in this investigation may be inherent to undisturbed LCN. The LCN found further away from the implant may not be required to respond to chemical changes caused by the implant material, and therefore display a lack of additional network efficiency and connectivity.

As mentioned, the study led by Kollmannsberger et al. is the only instance in which the LCN is investigated in sheep bone in literature [7]. Kollmannsberger et al. reported a lacunar porosity (or void fraction) of approximately 5 %, which similarly aligns with the lacunar porosity found near the PEO-coated material (4–8 %) in this study. However, canalicular densities in terms of distance per volume reported in our investigation (0.82–2.41 $\mu m/\mu m^3$) are much higher than what is stated by Kollmannsberger et al. (0.19 $\mu m/\mu m^3$). The higher density of the canaliculi observed in our study however, is clearly supported by the segmentation of the canaliculi as visualised in Fig. 6. The distance from a matrix voxel to the LCN (d_{LC}) was found to be smaller in our investigation (0.2–0.4 μm) when compared to the 1 μm reported by Kollmannsberger et al. which again may likely be due to the higher resolution used for imaging in our study. The average distance within the canaliculi to reach a cell body (d_{net}) reported by Kollmannsberger et al. (10.25 μm) more similarly resembled the LCN found near the PEO-coated material (12.25 μm). From our results, the LCN found near the PEO-coated material contributed to a lower gain factor over the analysed time, which more comparably aligns to the reported gain factor of 10 found in mature sheep bone mentioned by Kollmannsberger et al. This may suggest that the slower degradation induced by the PEO-coated material may arrange an LCN with comparable gain capabilities as mature bone. Overall, our quantitative results are in good agreement with the values reported by Kollmannsberger et al.

The LCN is crucial to bone remodelling and maintaining mineral homeostasis. From Fig. 9, we see that bone surrounding the PEO-coated material exhibited lower canalicular porosity and fewer canaliculi attached to the lacunar surfaces when compared to bone found near the uncoated material. The reduced shear stresses sensed by local osteocytes caused by a delayed degradation of metallic base materials may in turn reduce the required permeability of the LCN. Bortel et al. found that interconnectivity between canaliculi promotes robust network transport capabilities and mineral access when canaliculi are interrupted [43]. The study revealed that although interconnectivity increases total canalicular network length, an increase in canaliculi acts to stabilise the overall network performance. If interruption occurs at one pathway, a larger ECM volume is still accessible due to extra connections within the system. Thus, the LCN surrounding the PEO-coated material may have limited access to ECM if canalicular interruption occurs when compared to bone with more connectivity as a response to higher degradation rates. Interestingly, not only is there a stronger canalicular presence near bone found in the vicinity of the implant surface for the uncoated samples, but results from distant bone demonstrate a higher connectivity when compared to bone implanted with PEO-coated material as well.

In addition to earlier works describing the analysis of lacunae and canaliculi, Wittig et al. have introduced a third LCN structure, the canalicular junction (CJ). Findings from their study suggest that these

CJs are integral to osteocyte communication and possibly canalicular ECF flow. We report CJ density values of approximately 10^8 per mm^3 (Fig. 9) and lacunar densities of approximately and 10^4 per mm^3 (Fig. 7) for both implant materials. This factor of 10^4 between CJ and lacunar density may be introduced as response to altered chemical stimuli by the LCN specifically after material implantation, unlike typical stimuli sensed from everyday physical activity. This factor may be characteristic to healing bone as previous studies show a similar quantitative amounts between CJ and lacunar density in healthy bone [6]. Wittig et al. demonstrated that CJs found in healthy sheep femora occur at a density similar to that of osteocyte lacunae. By visual inspection of the segmented TXM data, it is evident that the LCN in our samples are not as evenly dispersed and well-organised as the undisturbed bone specimen imaged by Wittig et al. For this reason, altered stimuli received by the LCN due to implanted material may induce an increase in CJ density. Specifically, a higher degradation rate, as found in the uncoated material, may induce an increase in CJ density in surrounding bone.

This investigation has some limitations. Though LCN variations are apparent between the two materials, statistical analyses could not be performed due to low number of samples. Additionally, the bone sample furthest from the 12-week PEO coated specimen was lost during the manufacturing of the bone specimen. A variability is introduced since bone healing may progress at different speeds depending on the animal, thus requiring an increase in animal samples to better substantiate the results. Furthermore, bone specimen analysed in this investigation were collected from internal woven bone of sheep femur and tibia. Investigations of the superficial lamellar bone response would provide further insight since woven bone is characterised as inadequately organised and less dense with higher cellularity when compared to lamellar bone. The inclusion of longer time points, particular to the PEO-coated material, would provide a deeper understanding and quantification of the delayed effect caused by retarded degradation. Moreover, similar investigations to include human bone is warranted to further justify LCN equivalencies to sheep bone. Surface morphology of the PEO coating should additionally be investigated to determine the influence of implant surface on the LCN.

5. Conclusion

To the best of our knowledge, this pilot investigation is the first of its kind to analyse LCN morphology surrounding a biodegradable implant. Morphological differences in sheep bone LCN have been observed as a response to varied chemical stimuli induced by uncoated and PEO-coated WE43 materials. Smoother ellipsoidal lacunar shapes surrounding PEO-coatings may indicate that lower degradation rates favour lacunae which are better resistant to damage. To the contrary, uncoated material exhibiting higher degradation rates seem to elicit a higher interconnected LCN prone to better stability against canalicular interruption. To confirm delayed variations, PEO-coatings cause on the LCN, similar studies including additional samples, longer time periods, and new complexity measures should further be performed.

Funding sources

This project has received funding from the European Union's Horizon 2020 research and innovation programme under the Marie Skłodowska-Curie grant agreement No 811226. Author Flenner gratefully acknowledges the financial support from the Deutsche Forschungsgemeinschaft (DFG, German Research Foundation) - Project number 192346071, SFB 986 (project Z2).

CRediT authorship contribution statement

Jonathan Espiritu: Data curation, Formal analysis, Investigation, Methodology, Validation, Visualization, Roles, Writing – original draft. **Sandra Sefa:** Data curation. **Hanna Cwieka:** Data curation. **Imke Greving:** Methodology, Resources, Software, Supervision, Validation, Writing – review & editing. **Silja Flenner:** Funding acquisition, Methodology, Software, Validation, Writing – review & editing. **Regine Willumeit-Römer:** Funding acquisition, Project administration, Writing – review & editing. **Jan-Marten Seitz:** Funding acquisition, Project administration, Resources, Writing – review & editing. **Berit Zeller-Plumhoff:** Conceptualization, Data curation, Investigation, Methodology, Project administration, Software, Supervision, Validation, Writing – review & editing.

Declaration of competing interest

Syntellix AG is a medical technology manufacturer of metallic and bio-absorbable clinical implants. Authors Espiritu and Seitz are employed as Research Associate and Chief Technical Officer, respectively.

Acknowledgements

We acknowledge provision of beamtime by PETRA III DESY within the Proposal I-20210281. This research was supported in part through the Maxwell computational resources operated at DESY.

Appendix A. Supplementary data

Supplementary data to this article can be found online at https://doi.org/10.1016/j.bioactmat.2023.02.018.

References

[1] D. Krüger, S. Galli, B. Zeller-Plumhoff, D. Wieland, N. Peruzzi, B. Wiese, P. Heuser, J. Moosmann, A. Wennerberg, R. Willumeit-Römer, High-resolution ex vivo analysis of the degradation and osseointegration of Mg-xGd implant screws in 3D, Bioact. Mater. 13 (2022) 37–52.
[2] J. Moosmann, B. Zeller-Plumhoff, D. Wieland, S. Galli, D. Krüger, T. Dose, H. Burmester, F. Wilde, M. Bech, N. Peruzzi, B. Wiese, A. Hipp, F. Beckmann, J. Hammel, R. Willumeit-Römer, Biodegradable magnesium-based implants in bone studied by synchrotron radiation microtomography, in: Proceedings SPIE 10391, Developments in X-Ray Tomography XI, 2017. San Diego, California, US.
[3] B. Yu, A. Pacureanu, C. Olivier, P. Cloetens, F. Peyrin, Assessment of the human bone lacuno-canalicular network at the nanoscale and impact of spatial resolution, Sci. Rep. 10 (2020) 4567.
[4] L. Bonewald, The amazing osteocyte, J. Bone Miner. Res. 26 (2) (2011) 229–238.
[5] F. Shah, P. Thomesen, A. Palmquist, A review of the impact of implant biomaterials on osteocytes, J. Dent. Res. 97 (9) (2018).
[6] N. Wittig, M. Laugesen, M.B.-G.F. Birkbak, A. Pacureanu, S. Bruns, M. Wendelboe, A. Burüel, H. Sorenson, J.B.H. Thomsen, Canalicular junctions in the osteocyte lacuno-canalicular network of cortical bone, ACS Nano 13 (6) (2019) 6421–6430.
[7] P. Kollmannsberger, M. Kerschnitzki, F. Repp, W. Wagermaier, R. Weinkamer, P. Fratzl, The small world of osteocytes: connectomics of the lacuno-canalicular network in bone, New J. Phys. 19 (2017).
[8] J. Wang, F. Jia, T. Gilbert, S. Woo, Cell orientation determines the alignment of cell-produced collagenous matrix, J. Biomech. 36 (1) (2003) 97–102.
[9] B. Hesse, P. Varga, M. Langer, A. Pacureanu, S. Schrof, N. Männicke, H. Suhonen, P. Maurer, P. Cloetens, F. Peyrin, K. Raum, Canalicular network morphology is the major determinant of the spatial distribution of mass density in human bone tissue: evidence by means of synchrotron radiation phase-contrast nano-CT, J. Bone Miner. Res. 30 (2) (2014) 346–356.
[10] A. Ashique, L. Hart, C. Thomas, J. Clement, P. Pivonka, Y. Carter, D. Mousseau, D. Cooper, Lacunar-canalicular network in femoral cortical bone is reduced in aged women and is predominantly due to a loss of canalicular porosity, BoneKEy Rep. 7 (2017) 9–16.
[11] M. Tate, J. Adamson, A. Tami, T. Bauer, The osteocyte, Int. J. Biochem. Cell Biol. 36 (1) (2004) 1–8.
[12] L. Tiede-Lewis, S. Dallas, Changes in the osteocyte lacunocanalicular network with aging, Bone 112 (2019) 101–113.
[13] M. Hussein, A. Mohammed, N. Al-Aqeeli, Wear characteristics of metallic biomaterials: a review, Materials 8 (5) (2015) 2749–2768.
[14] D. Vos, M. Verhofstad, Indications for implant removal after fracture healing: a review of the literature, Eur. J. Trauma Emerg. Surg. 39 (2013) 327–337.
[15] H. Windhagen, K.W.A. Radtke, J. Diekmann, Y. Noll, U. Kreimeyer, R. Schavan, C. Stukenborg-Colsman, H. Waizy, Biodegradable magnesium-based screw clinically equivalent to titanium screw in hallux valgus surgery: short term results of the first prospective, randomized, controlled clinical pilot study, Biomed. Eng. Online 12 (62) (2013).

[16] H. Zhou, B. Liang, H. Jiang, Z. Deng, K. Yu, Magnesium-based biomaterials as emerging agents for bone repair and regeneration: from mechanism to application, Journal of Magnesium and Alloys 9 (3) (2021) 779–804.
[17] S. Amukarimi, M. Mozafari, Biodegradable magnesium-based biomaterials: an overview of challenges and opportunities, MedComm 2 (2) (2021) 123–144.
[18] H. May, Y. Kati, G. Gumussuyu, T. Emre, M. Unal, O. Kose, Bioabsorbable magnesium screw versus conventional titanium screw fixation for medial malleolar fractures, J. Orthop. Traumatol. 21 (9) (2020).
[19] F. Wagner, A. Post, T. Yilmaz, D. Maier, J. Neubauer, M. Feucht, N. Südkamp, K. Reising, Biomechanical comparison of biodegradable magnesium screws and titanium screws for operative stabilization of displaced capitellar fractures, J. Shoulder Elbow Surg. 29 (9) (2020) 1912–1919.
[20] B. Acar, O. Kose, M. Unal, A. Turan, Y. Kati, F. Guler, Comparison of magnesium versus titanium screw fixation for biplane chevron medial malleolar osteotomy in the treatment of osteochondral lesions of the talus, Eur. J. Orthop. Surg. Traumatol. 30 (2020) 163–173.
[21] H. Atkinson, S. Khan, Y. Lashgari, A. Ziegler, Hallux valgus correction utilising a modified short scarf osteotomy with a magnesium biodegradable or titanium compression screws – a comparative study of clinical outcomes, BMC Muscoskel. Disord. 20 (334) (2019).
[22] B. Acar, O. Kose, A. Turan, M. Unal, Y. Kati, F. Guler, Comparison of bioabsorbable magnesium versus titanium screw fixation for modified distal chevron osteotomy in hallux valgus, BioMed Res. Int. 2018 (2018) 9.
[23] C. Rendenbach, H. Fischer, A. Kopp, K. Schmidt-Bleek, H. Kreiker, S. Stumpp, M. Thiele, G. Duda, H. Hanken, B. Beck-Broichsitter, O. Jung, N. Kröger, R. Smeets, M. Heiland, Improved in vivo osseointegration and degradation behavior of PEO surface-modified WE43 magnesium plates and screws after 6 and 12 months, Mater. Sci. Eng. C 129 (2021).
[24] H. Sampatirao, S. Radhakrishnapillai, S. Dondapati, E. Parfenov, R. Nagumothu, Developments in plasma electrolytic oxidation (PEO) coatings for biodegradable magnesium alloys, Mater. Today Proc. 46 (2) (2021) 1407–1415.
[25] T. Monetta, P. Parnian, A. Acquesta, Recent advances in the control of the degradation rate of PEO treated magnesium and its alloys for biomedical applications, Metals 10 (7) (2020).
[26] E. Matykina, I. Garcia, R. Arrabal, M. Mohedano, B. Mingo, J. Sancho, M. Merino, A. Pardo, Role of PEO coatings in long-term biodegradation of a Mg alloy, Appl. Surf. Sci. 389 (2016) 810–823.
[27] H. Sampatirao, S. Radhakrishnapillai, S. Dondapati, E. Parfenov, R. Nagumothu, Developments in plasma electrolytic oxidation (PEO) coatings for biodegradable magnesium alloys, Materials Stoday; Proceedings 46 (2) (2021) 1407–1415.
[28] F. Shah, X. Wang, P. Thomsen, K. Grandfield, A. Palmquist, High-resolution visualization of the osteocyte lacuno-canalicular network juxtaposed to the surface of nanotextured titanium implants in human, ACS Biomater. Sci. Eng. 1 (5) (2015) 305–313.
[29] T. Nakashima, M. Hayashi, T. Fukunaga, K. Kurata, M. Oh-hora, J. Feng, L. Bonewald, T. Kodama, A. Wutz, E. Wagner, J.T.H. Penninger, Evidence for osteocyte regulation of bone homeostasis through RANKL expression, Nat. Med. 17 (2011) 1231–1234.
[30] L. You, S. Weinbaum, S. Cowin, M. Schaffler, Ultrastructure of the osteocyte process and its pericellular matrix, Anat. Rec. 278A (2) (2004) 505–513.
[31] Y. Lin, S. Xu, AFM analysis of the lacunar-canalicular network in demineralized compact bone, J. Microsc. 241 (3) (2010) 291–302.
[32] S. Hirose, M. Li, T. Kojima, P. de Freitas, S. Ubaidus, K. Oda, C. Saito, N. Amizuka, A histological assessment on the distribution of the osteocytic lacunar canalicular system using silver staining, J. Bone Miner. Metabol. 25 (2007) 374–382.
[33] T. Hasegawa, T. Yamamoto, H. Hongo, Z. Qiu, M. Abe, T. Kanesaki, K. Tanaka, T. Endo, P. de Freitas, M. Li, N. Amizuka, Three-dimensional ultrastructure of osteocytes assessed by focused ion beam-scanning electron microscopy (FIB-SEM), Histochem. Cell Biol. 149 (2018) 423–432.
[34] Y. Liu, B. Chen, D. Yin, Effects of direction and shape of osteocyte lacunae on resisting impact and micro-damage of osteon, J. Mater. Sci. Mater. Med. 28 (38) (2017).
[35] P. Schneider, M. Meier, R. Wepf, R. Müller, Serial FIB/SEM imaging for quantitative 3D assessment of the osteocyte lacuno-canalicular network, Bone 49 (2) (2011) 304–311.
[36] S. Okada, S. Yoshida, S. Ashrafi, D. Schraufnagel, The canalicular structure of compact bone in the rat at different ages, Microsc. Microanal. 8 (2) (2002) 104–115.
[37] H. Kamioka, Y. Kameo, Y. Imai, A. Bakker, R. Bacabac, N. Yamada, A. Takaoka, T. Yamashiro, T. Adachi, J. Klein-Nulend, Microscale fluid flow analysis in a human osteocyte canaliculus using a realistic high-resolution image-based three-dimensional model, Integrative Biology 4 (10) (2012) 1198–1206.
[38] H. Kamioka, S. Murshid, Y. Ishihara, N. Kajimura, T. Hasegawa, R. Ando, Y. Sugawara, T. Yamashiro, A. Takaoka, T. Takano-Yamamoto, A method for observing silver-stained osteocytes in situ in 3-μm sections using ultra-high voltage electron microscopy tomography, Microsc. Microanal. 15 (5) (2009) 377–383.
[39] M. Rubin, J. Rubin, I. Jasiuk, SEM and TEM study of the hierarchical structure of C57BL/6J and C3H/HeJ mice trabecular bone, Bone 35 (1) (2004) 11–20.
[40] R. Genthial, E. Beaurepaire, M. Schanne-Klein, F. Peyrin, D. Farlay, C. Olivier, Y. Bala, G. Boivin, J. Vial, D. Debarre, A. Gourrier, Label-free imaging of bone multiscale porosity and interfaces using third-harmonic generation microscopy, Sci. Rep. 7 (2017).
[41] S. Kamel-ElSayed, L. Tiede-Lewis, Y. Lu, P. Veno, S. Dallas, Novel approaches for two and three dimensional multiplexed imaging of osteocytes, Bone 76 (2015) 129–140.
[42] M. Dierolf, A. Menzel, P. Thibault, P. Schneider, C. Kewish, R. Wepf, O. Bunk, F. Pfeiffer, Ptychographic X-ray computed tomography at the nanoscale, Nature 467 (2010) 436–439.
[43] E. Bortel, L. Gover, N. Eisenstein, C. Seim, H. Suhonen, A. Pacureanu, P. Westenberger, K. Raum, M. Langer, F. Peyring, O. Addison, B. Hesse, Interconnectivity explains high canalicular network robustness between neighboring osteocyte lacunae in human bone, Adv. Nano Biomed Res. 2 (4) (2021).
[44] A. Pacureanu, M. Langer, E. Boller, P. Tafforeau, F. Peyrin, Nanoscale imaging of the bone cell network with synchrotron X-ray tomography: optimization of acquisition setup, Med. Phys. 39 (4) (2012) 2229–2238.
[45] P. Varga, B. Hesse, M. Langer, S. Schrof, N. Männicke, H. Suhonen, A. Pacureanu, D. Pahr, F. Peyrin, K. Raum, Synchrotron X-ray phase nano-tomography-based analysis of the lacunar–canalicular network morphology and its relation to the strains experienced by osteocytes in situ as predicted by case-specific finite element analysis, Biomech. Model. Mechanobiol. 14 (2015) 267–282.
[46] E. Stockhausen, M. Qwamizadeh, E. Wölfel, H. Hemmatian, I. Fiedler, S. Flenner, E. Longo, M. Amling, I. Greving, R. Ritchie, F. Schmidt, B. Busse, Collagen fiber orientation is coupled with specific nano-compositional patterns in dark and bright osteons modulating their biomechanical properties, ACS Nano 12 (1) (2021) 455–467.
[47] S. Flenner, A. Kubec, C. David, M. Storm, C. Schaber, F. Vollrath, M. Müller, I. Greving, J. Hagemann, Hard X-ray nano-holotomography with a Fresnel zone plate, Opt Express 28 (25) (2020) 37514–37525.
[48] B. Zeller-Plumhoff, D. Tolnai, M. Wolff, I. Greving, H. Norbert, R. Willumeit-Römer, Utilizing synchrotron radiation for the characterization of biodegradable magnesium alloys—from alloy development to the application as implant material, Adv. Eng. Mater. 23 (11) (2021).
[49] A. Materials, Magnesium Elektron WE43 Alloy (UNS M18430), 2022 [Online]. Available: https://www.azom.com/article.aspx?ArticleID=9279. (Accessed 29 July 2022).
[50] S. Ag, Method for Producing a Medical Implant from a Magnesium Alloy", United States Patent US9402669B2, 2011, 06 09.
[51] I. O. f. S. (ISO), Biological Evaluation of Medical Devices — Part 6: Tests for Local Effects after Implantation, ISO 10993-6:2007, Berlin, Germany, 2007.
[52] S. Flenner, M. Storm, A. Kubec, E. Longo, F. Döring, D. Pelt, C. David, M. Müller, I. Greving, Pushing the temporal resolution in absorption and Zernike phase contrast nanotomography: enabling fast in situ experiments, Jounral of Synchrotron Radiation 27 (5) (2020) 1339–1346.
[53] D. Gürsoy, F. De Carlo, X. Xiao, C. Jacobsen, TomoPy: a framework for the analysis of synchrotron tomographic data, J. Synchrotron Radiat. 21 (5) (2014) 1188–1193.
[54] J. Schindelin, I. Arganda-Carreras, E. Frise, V. Kaynig, M. Longair, T. Pietzsch, S. Preibisch, C. Rueden, S. Saalfeld, B. Schmid, J. Tinevez, D. White, V. Hartenstein, K. Eliceiri, P. Tomancak, A. Cardona, Fiji: an open-source platform for biological-image analysis, Nat. Methods 9 (2012) 676–682.
[55] E. Nidadavolu, F. Feyerabend, T. Ebel, R. Willumeit-Römer, M. Dahms, On the determination of magnesium degradation rates under physiological conditions, Materials 9 (8) (2016) 627.
[56] S. Bruns, S. Stipp, H. Sorensen, Looking for the Signal: a guide to iterative noise and artefact removal in X-ray tomographic reconstructions of porous geomaterials, Adv. Water Resour. 105 (2017) 96–107.
[57] D. Legland, I. Arganda-Carreras, P. Andrey, MorphoLibJ: integrated library and plugins for mathematical morphology with ImageJ, Bioinformatics 32 (22) (2016) 3532–3534.
[58] X. Gu, S. Li, X. Li, Y. Fan, Magnesium based degradable biomaterials: a review, Front. Mater. Sci. 8 (2014) 200–218.
[59] C. Ivanoff, L. Sennerby, C. Johansson, B. Rangert, U. Lekholm, Influence of implant diameters on the integration of screw implants: an experimental study in rabbits, Int. J. Oral Maxillofac. Surg. 26 (2) (1997) 141–148.
[60] M. Casanova, A. Schindeler, L. Peacock, L. Lee, P. Schneider, D. Little, R. Müller, Characterization of the developing lacunocanalicular network during fracture repair, JBMR Plus 5 (9) (2021).

Chapter 7

Evaluating metallic artefact of biodegradable magnesium-based implants in magnetic resonance imaging

The attainment of appropriate image quality is a critical factor underpinning the efficacy of magnetic resonance imaging (MRI). It is well-documented that Mg-based materials have been associated with the generation of image distortions in MRI examinations. Nevertheless, a notable void exists in current literature concerning the impact of the degradation properties inherent to Mg-based implants on MRI image quality. This study is dedicated to the comprehensive investigation and quantification of the metallic artefact characteristics exhibited by Mg-based orthopaedic screws, particularly as they undergo degradation in diverse media and tissue environments. Our findings, derived from extensive experimentation encompassing *in vitro, in vivo,* and clinical scenarios involving scaphoid fracture treatments, reveal a notable reduction in artefact generation by Mg-based material over extended degradation periods. Notably, statistical analysis demonstrates a significant difference ($p < 0.05$) in metallic artefact production between the Mg-based and titanium (Ti) material groups. These outcomes present a compelling argument for further exploration of Mg-based materials as viable candidates for medical implants, including an in-depth inquiry into their potential role in facilitating the assessment of bone healing through MRI modalities.

The results have been published in the journal *Bioactive Materials* and has been reproduced with permission.

Bioactive Materials 15 (2022) 382–391

Contents lists available at ScienceDirect

Bioactive Materials

journal homepage: www.keaipublishing.com/en/journals/bioactive-materials

Evaluating metallic artefact of biodegradable magnesium-based implants in magnetic resonance imaging

Jonathan Espiritu [a,*], Mostafa Berangi [b,c,d], Christina Yiannakou [e], Eduarda Silva [f], Roberto Francischello [g,h], Andre Kuehne [b], Thoralf Niendorf [b,c,d], Sören Könneker [c], Regine Willumeit-Römer [i], Jan-Marten Seitz [a]

[a] Syntellix AG, Hannover, Germany
[b] MRI.TOOLS GmbH, Berlin, Germany
[c] Charité – Universitätsmedizin Berlin, Corporate Member of Freie Universität Berlin and Humboldt Universität zu Berlin, Berlin, Germany
[d] Berlin Ultrahigh Field Facility (B.U.F.F.), Max-Delbrueck Center for Molecular Medicine in the Helmholtz Association, Berlin, Germany
[e] Hannover Medical School, Hannover, Germany
[f] Institute of Clinical Physiology, National Research Council, Pisa, Italy
[g] Chemistry and Industrial Chemistry Department, Università di Pisa, Via Moruzzi 13, Pisa, Italy
[h] Fondazione Toscana Gabriele Monasterio, Via Moruzzi 1, Pisa, Italy
[i] Institute for Materials Research, Helmholtz Zentrum Hereon, Geesthacht, Germany

ARTICLE INFO

Keywords:
Magnetic resonance imaging
Magnesium
Biodegradable implants
Medical imaging
Translational medicine

ABSTRACT

Magnesium (Mg) implants have shown to cause image artefacts or distortions in magnetic resonance imaging (MRI). Yet, there is a lack of information on how the degradation of Mg-based implants influences the image quality of MRI examinations. In this study, Mg-based implants are analysed *in vitro, ex vivo,* and in the clinical setting for various magnetic field strengths with the aim to quantify metallic artefact behaviour. *In vitro* corroded Mg-based screws and a titanium (Ti) equivalent were imaged according to the ASTM F2119. Mg-based and Ti pins were also implanted into rat femurs for different time points and scanned to provide insights on the influence of soft and hard tissue on metallic artefact. Additionally, MRI data of patients with scaphoid fractures treated with CE-approved Mg-based compression screws (MAGNEZIX®) were analysed at various time points post-surgery. The artefact production of the Mg-based material decreased as implant material degraded in all settings. The worst-case imaging scenario was determined to be when the imaging plane was selected to be perpendicular to the implant axis. Moreover, the Mg-based implant outperformed the Ti equivalent in all experiments by producing lower metallic artefact ($p < 0.05$). This investigation demonstrates that Mg-based implants generate significantly lower metallic distortion in MRI when compared to Ti. Our positive findings suggest and support further research into the application of Mg-based implants including post-operative care facilitated by MRI monitoring of degradation kinetics and bone/tissue healing processes.

1. Introduction

Traditional permanent orthopaedic implants have shown to cause inflammatory responses [1] in addition to further refracture risk [2]. These inappropriate bodily reactions and mechanical failures suggest that other solutions be investigated for temporary bone support, such as magnesium (Mg)- based alloy materials. The ability to safely degrade *in vivo* as a load-bearing implant material is arguably the most attractive property [3–5]. The similar elastic modulus and densities between Mg alloys and natural bone prevent negative mechanical conditions such as stress-shielding [6]. Recognizing the increasing usage of Mg material in the clinical setting magnetic resonance imaging (MRI) presents a viable diagnostic imaging modality for the examination of the degradation status of biodegradable implants and for the study of the implant/tissue interface. MRI is a mainstay of today's diagnostic imaging due to its ability to provide excellent soft tissue contrast at high spatial resolution [7–9]. Computed tomography (CT) is widely used in clinical practice to image bone fractures and corresponding implants. However, CT provides little information on soft tissue processes. The use of ionising

Peer review under responsibility of KeAi Communications Co., Ltd.
* Corresponding author.
E-mail address: espiritu@syntellix.com (J. Espiritu).

https://doi.org/10.1016/j.bioactmat.2021.11.035
Received 8 September 2021; Received in revised form 12 November 2021; Accepted 28 November 2021
Available online 6 January 2022

Abbreviations

AP	Anterior/Posterior
ASTM	American Society of Testing and Materials
B 0	Main Magnetic Field
DICOM	Digital Imaging and Communications in Medicine
FOV	Field of View
GRE	Gradient Echo
HF	Head/Foot
LR	Left/Right
Mg MRI	Magnetic Resonance Imaging
ORTH	Orthogonal
PAR	Parallel
RF	Radio Frequency
SAG	Sagittal
TAV	Total Artefact Volume
TE	Echo Time
Ti	Titanium
tp	Time Point
TR	Repetition Time
TRA	Transverse
TSE	Turbo Spin Echo
w	Weighted

radiation in serial CT examinations adds to the cumulative radiation dose of patients which may be associated with a small but significantly increased risk of malignancy [10]. Since MRI does not administer any type of ionising radiation, long-term harmful effects are considered insignificant [11]. However, diagnostic imaging quality can be compromised by image artefacts attributed to the patient (motion and flow artefacts), signal processing (wrap around and chemical shifts), or to the hardware (static magnetic field or radiofrequency (RF) transmission field inhomogeneities).

In MRI metallic implants may cause image distortion artefacts, or susceptibility artefacts. Metals have intrinsic magnetic susceptibilities that produce significant local field disturbances. These local changes in the resonance frequency shift image pixels away from their true positions leading to significant geometric distortions including signal reduction or voids (black areas in the image) and signal enhancements (bright areas in the image). These distortions are created by perturbations of the static magnetic field and are related to the specific material properties of the implant. Although there have been many methods demonstrating a reduction in artefacts [12], complete metallic artefacts cannot be removed.

Metallic implants made of materials, like Mg, have shown to cause image artefacts due to the inherent magnetic susceptibility of the material. However, their impact on MRI quality is less compared to other current permanent metallic implants [13].

The evaluation of artefact production in MRI is necessary when choosing a biomaterial. Artefact limitation is vital since compromised or poor image quality may disturb medical diagnosis or anatomical visualisation. The aim of this investigation is to quantify the metallic artefact production of Mg-based implants during the degradation process in various MRI settings with the ultimate goal to support the use of Mg-based implants in the clinical setting due to successful visualisation in MRI. To benchmark the MRI performance of Mg-based implants standard, commercial Ti based implants are used as a reference.

2. Materials and methods

2.1. In vitro investigation

Orthopaedic compression screws 40 mm in length and diameter of 3.2 mm made of WE43-based material manufactured by Syntellix AG (Hannover, Germany) underwent *in vitro* degradation. The volume of the WE43 screw is 151.51 mm^3 with a surface area of 552.54 mm^2. Chemical composition of WE43 includes Yttrium (3.7–4.3%), Rare Earth Elements (2.4–4.4%), Zirconium (0.4%), with the remainder composing of Mg [14]. A non-degraded WE43 screw and a titanium equivalent of similar geometry were included for comparative results (Fig. 1).

The WE43 samples were degraded via a modified ASTM F3268 Standard [15] with Dulbecco's Phosphate Buffered Saline (DPBS). A total of five screws were degraded in the DPBS with different immersion times varying by one week with a total of five time points (1 week, 2 weeks, 3 weeks, 4 weeks, and 5 weeks). After immersion time was completed, the samples were cleaned with distilled water to remove any excess salts and rinsed with ethanol to prevent further oxidation before drying and storage.

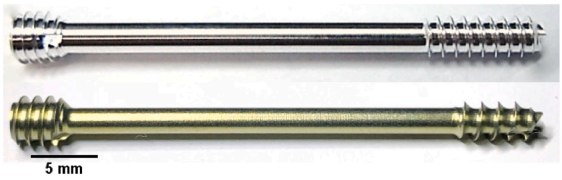

Fig. 1. 40 mm Mg-based orthopaedic compression screw MAGNEZIX® CS ø3.2 (top) and Ti market-equivalent (bottom).

For the in vitro MRI measurements, a 1.5 T (GE Signa Artist, GE Healthcare, Waukesha, USA), 3.0 T (Skyra Fit, Siemens, Erlangen, Germany) and 7.0 T (Magnetom, Siemens, Erlangen, Germany) MRI Scanner were used. Further details on the imaging protocol and imaging techniques employed for the *in vitro* measurements are documented in Table 1.

The following *in vitro* procedure has been adapted from ASTM F2119 [16] and consists of two parts: (1) the acquisition of images with the test object's long axis perpendicular to the main magnetic field (B_0), and (2) the acquisition of images with the test object's long axis parallel to the main magnetic field. Implant orientation relative to the main magnetic field, imaging sequence applied, slice orientation, phase-encoding direction, and material were varied for each combination before each image acquisition. The test object was suspended in a home built phantom acrylic container via a 3D printed holder filled with $CuSO_4$ solution (Merck Millipore, USA) to reduce T_1 relaxation effects. Artefact dimensions were determined by applying the ASTM F2119 definition for artefacts via a custom MATLAB (The MathWorks Inc., USA) script. Examples of measurements completed by the script are shown in Fig. 2. The diameter artefact is measured by determining the longest artefact along the diameter of the screw. The length artefact is determined by measuring the longest artefact along the length of the screw. The largest

Table 1
Parameters of sequences used for *in vitro* MRI investigations.

B_0 Field Strength [T]	1.5		3.0		7.0	
RF Coil Type	Spinal		Spinal		Basic Volume	
Sequence	GRE	TSE	GRE	TSE	GRE	TSE
TR [ms]	100	500	500	1190	550	1190
TE [ms]	15	20	13	20	13	30
FOV [mm]	300	300	180	200	185	185
Matrix Size [pixel]	256	256	256	256	256	256
Slice Thickness [mm]	2	2	2	2	2	2

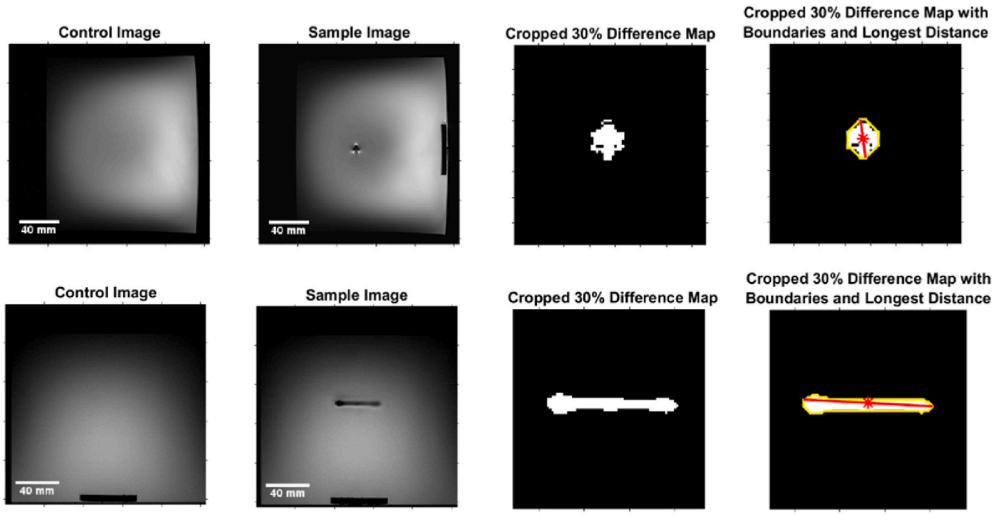

Fig. 2. Script workflow of diameter (to p) and length (bottom) artefact measurement of image data acquired at 3 T MRI. A control and a sample image are loaded and compared to detect a 30% intensity change. This change is used to create a binary image where a longest distance can then be measured (red indicator line).

measurements are taken as the 'worst-case' artefact.

Calculation of test object distortion was performed to determine the artefact size in relation to the test object dimension. Test object distortion is calculated by:

$$\frac{\textit{Total artefact length measured} - \textit{test object dimension}}{\textit{Test object dimension}}$$

2.2. Ex vivo investigation

2.2.1. Experimental animals

All *in vivo* experiments were carried out in accordance with the National Ethical Guidelines (Italian Ministry of Health; D.L.vo 26/2014) and the guidelines from Directive 2010/63/EU of the European Parliament. The protocol was approved by the Instituto Superiore di Sanità on behalf of Italian Ministry of Health and Ethical Panel (Prot. n° 299/2020-PR) and the local ethics committee. Additionally, the protocol conformed to the ARRIVE guidelines [17].

A total of three 12-week-old female Wistar rats were used in this experiment. On surgery, animals were anesthetized with an intraperitoneal injection of 5 mg/kg Xylazine (Rompum Elanco, Italy) and 10 mg/kg Zoletil (Virbac, Switzerland). The depth of anaesthesia was controlled by toe pinch response.

2.2.2. Surgical approach

Through a lateral approach, an incision was made on the skin and the muscles are carefully teased away to expose the mid-diaphyseal region of the femur. A drill with 1.55 mm diameter is used to prepare the transcortical implantation bed with the longitudinal axis of this drill perpendicular to the longitudinal axis of the femoral diaphysis. Drilling is performed at low rotational speed and profuse physiological saline (Fresenius Kabi, Italy) irrigation is applied via syringe to minimise frictional heat and thermal necrosis. A pin implant of 8 mm in length and 1.5 mm in diameter made of WE43 or Ti was implanted in this procedure. The cylindrical implant is inserted by gentle tapping, resulting in a uniform press fit. After transcortical placement is ensured, the operating field is cleaned with sterile cotton tips for remaining bone debris and the wound is closed with resorbable sutures (Johnson & Johnson Medical, Italy). Thereafter, the contralateral side is operated in the same way and using the same implant type.

The sacrifice of the animals at various time-points is performed with a lethal dose of isoflurane (IsoFlo, Zoetis, Italy); hind paws are explanted cutting through the hip joint and stored at −20 °C until further analysis.

2.2.3. Explant imaging

The explants were scanned to obtain information on the influence of hard and soft tissue on the artefact production, moving closer to mimicking the true physiological environment. *Ex vivo* MRI measurements of the hind paws were performed at Consiglio Nationale delle Ricerche Area della Ricerca di Pisa (Pisa, Italy) using a 7 T small animal MRI scanner (Bruker Avance III HD 300). Further details and sequences employed for measurements are documented in Table 2.

DICOM images were loaded and analysed with MATLAB. The artefact area of each scan was measured within each sequence set for one explant containing a WE43-based pin one day after surgery, one explant containing a WE43-based pin thirty days after surgery, and one explant containing a Ti-based equivalent. A single time-point was selected for Ti since the material is not expected to degrade, unlike the WE43 material. A total of 18 tracings were completed (six tracings per sample). To calculate the total artefact volume (TAV) for each scan, the artefact areas measured for each slice were summed and multiplied by the slice thickness as described by the Debatin method [18].

2.3. Clinical investigation

2.3.1. Clinical trial

Imaging data in humans was provided by the randomised controlled clinical trial SCAMAG (Comparison of scaphoid fracture osteosynthesis

Table 2
MRI sequences applied during explant imaging at 7 T.

B_0 Field Strength [T]	7.0
RF Coil	Quadrature Bird Cage
Sequence	T1 RARE
TR [ms]	1500
TE [ms]	7
Spatial resolution [mm]	0.12
FOV [mm]	30
Matrix Scan [pixel]	256
Slice Thickness [mm]	0.8

by magnesium-based headless Herbert screws with titanium Herbert screws) [19]. The trial is a blinded observer controlled parallel two-group post-market trial with a follow-up of one year per patient. Each involved patient is treated with either a Ti or Mg-based compression screw. The primary aim of SCAMAG is to demonstrate Mg-based compression screws as non-inferior when compared to Ti in the treatment of scaphoid fractures. The study protocol adheres to the SPIRIT [20] and CONSORT [21] statements. The SCAMAG trial was approved by the ethics committee of the Hanover Medical School (MHH) on September 27, 2017 (registration number: 7614) including registration with the German Register for Clinical Trials (DRKS, drks.de) on December 4, 2017 (registration number: DRKS00013368).

2.3.2. Patient imaging

Randomly chosen patients involved in the study treated with Mg-based compression screw (MAGNEZIX® CS, Syntellix AG, Hannover, Germany) participated in MRI examinations. The scans were performed on a 3 T MR scanner (Vario, Siemens, Erlangen, Germany) at the Medical School Hannover (Hannover, Germany). Typical wrist imaging MRI protocols were performed for this study, which are summarised in Table 3.

DICOM images were loaded and analysed with MATLAB R2019b (The MathWorks Inc., US). A total of four patient follow-up scans were included in this analysis. The first, second, third, and fourth patients were treated with a single compression screw of sizes Ø 2.7 mm with length 26 mm, Ø 3.2 mm with length 26 mm, Ø 3.2 mm with length 20 mm, Ø 3.2 mm with length 24 mm, respectively. The artefact area of each scan was measured within each sequence set for the available time points: 1.5-, 3-, 6-, and 12-months post operation. A total of 64 tracings were completed. The TAV was calculated similarly as in Section 2.2.

2.4. Statistics

Statistical analyses were performed using RStudio (RStudio, USA). A p-value of <0.05 was chosen to be statistically significant.

To compare the artefacts produced by Ti, Mg, and various time-corroded Mg samples in the *in vitro* measurements with respect to implant orientation, sequence type, slice orientation, and encoding direction, an analysis of variance (ANOVA) was completed. If a significant p-value was determined, pairwise comparisons were performed using a Tukey's post hoc multiple comparison procedure.

For *ex vivo* investigations, the ANOVA test was applied to determine differences between material implanted into the rat femur. The ANOVA test was also applied in the clinical cases to determine the significant effects of slice orientation and healing time on the TAV.

Table 3
MRI scanning protocols from SCAMAG clinical trial. Scanning sequences used include proton density-weighted turbo spin echo with fat saturation (PDw TSE with FS) and T1/T2-weighted turbo spin echo (T1/T2w TSE).

Field Strength [T]	3.0			
Sequence	PDw TSE with fat saturation	T1w TSE	T2w TSE	T2w TSE
Slice Plane	Axial	Coronal 1	Coronal 2	Sagittal
TR [ms]	3220–4290	485–586	3090–3160	2430–2920
TE [ms]	37	32	39	97
Spatial resolution [mm]	0.22	0.20	0.25	0.25
FOV [mm]	100 × 80	100 × 80	100 × 80	100 × 80
Slice Thickness [mm]	2	2	2	2

3. Results

3.1. In vitro results

3.1.1. Titanium vs magnesium

By varying different MRI scanning parameters (seen in Fig. 3) the significant differences were found for the Ti and Mg samples. For all main field magnetic strengths, the Mg-samples produced significantly less artefacts than the Ti counterparts. Turbo spin echo sequences produced lower artefacts versus gradient echo sequence. The averaged diameter- and length-measured artefacts are summarised in Table 4. Averaged distortions or artefact measured based on material and magnetic field strength are documented in Fig. 4. An increase in magnetic field strength results in an increase in artefact size for both materials. The application of the gradient echo sequence and use of Ti material generally produced higher distortions than the turbo spin echo sequence and the use of Mg with the exception of the PAR-TSE-TRA-AP/LR protocol at 3.0 T and 7.0 T of the PAR-TSE-SAG-AP protocol at 7.0 T. The Tukey post-hoc test revealed significant pairwise differences between the artefacts size obtained at 1.5 T and 7 T and at 3 T versus 7 T. No significant difference in artefact size was found between 1.5 T and 3 T. The p-values of parameters changed in this investigation are listed in Table 5.

3.1.2. The influence of Mg in vitro corrosion time on artefact production

Examining the effect of the Mg implant corrosion time on the artefact size revealed statistically significant results (Table 6). For all magnetic field strengths a general decrease of image distortion was found for increasing *in vitro* corrosion times of the implant (Fig. 5).The spin echo sequence produced lower artefacts than the gradient echo sequence (Fig. 6).

3.2. Ex vivo results

Fig. 7 illustrates MR images obtained for rat explants with Mg and Ti pins using the small bore animal 7 T MRI scanner. Ti produced higher distortion of approximately 3 times more TAV than the Mg-based samples ($p < 0.05$) when scanned with the Turbo RARE sequence. TAV averaging highlighted in Fig. 8 indicates a very minor decrease in TAV from one day to thirty days of the Mg samples post-surgery, although not significant. The implantation of the pin into the femur with hard tissue (bone) and soft tissue (muscle) disturbs the anatomic integrity of the images by introducing artefacts as illustrated in Fig. 7.

3.3. Clinical results

Fig. 9 shows a decrease in the hypointense area surrounding the implant after one month, three months, and twelve months post-surgery for a single patient. The rest of the patient data follows a comparable trend (Fig. 10). Significant differences were found between healing times and imaging slice positions. An increase in implant degradation and patient healing time resulted in a decrease in artefact production. Imaging the implant at 1.5 months with a T2w TSE sequence in the sagittal direction produced the largest TAV of approximately 650 mm^3. Since the screw is implanted into the scaphoid bone, the shape of the implant in Fig. 9 is defined since it is primarily surrounded by one type of material, spongy bone.

4. Discussion

Postoperative care in the field of orthopaedic surgery relies heavily on precise imaging techniques. Early-stage research of biomaterials concentrates on the assurance of appropriate mechanical and physiological responses between the host and the implant. Further along a product's developmental stage requires insight on product application and translational aspects. Medical imaging compatibility is one of the

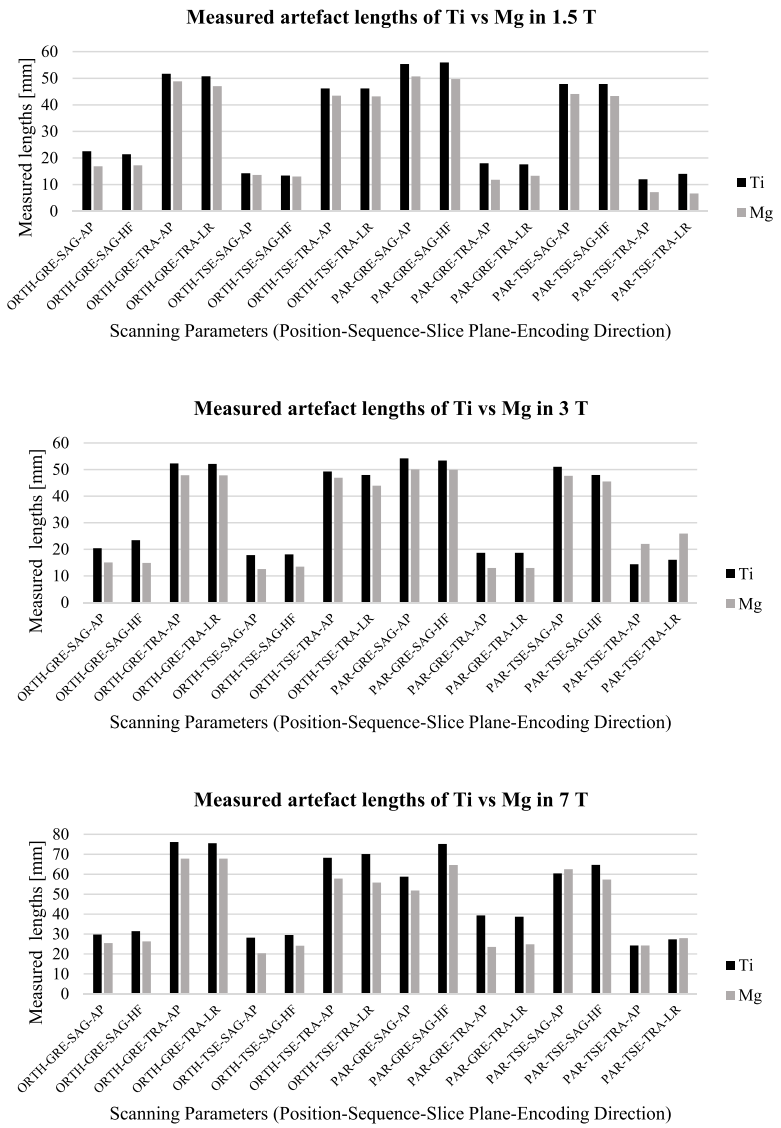

Fig. 3. Measured artefact lengths of Ti and Mg in various magnetic strengths. Implant position relative to the main magnetic field, sequence applied, slice plane, and phase encoding direction were altered for artefact measurements. (Reading format of y-axis: IMPLANT POSITION-SEQUENCE-SLICE PLANE-ENCODING DIRECTION).

Table 4
Average measured metallic artefact of Ti and Mg in MRI along the diameter and length of the implant.

B_0 Field Strength [T]	1.5		3.0		7.0	
Material	Ti	Mg	Ti	Mg	Ti	Mg
Average Diameter [mm]	16.7 ± 3.9	12.5 ± 3.9	18.5 ± 2.7	16.2 ± 5.0	31.1 ± 5.3	24.6 ± 2.2
Average Length [mm]	50.2 ± 3.9	46.3 ± 3.2	51.0 ± 2.4	47.5 ± 2.1	68.7 ± 6.9	60.7 ± 5.9

many focusses. The artefact production of an implant material may sometimes be overlooked but is a key property of the material and must be considered during a product's design process. Previous studies have documented artefact behaviour of magnesium-based implants in MRI [22–24]. Our study is the first which reports on the assessment of artefact behaviour of WE43-based implants in *in vitro, ex vivo,* and clinical environments. Our work adds to the literature by examining the impact of the magnetic field strength on the artefact behaviour. More importantly, our study provides clinically meaningful insights on how degradation time affects artefact behaviour for the experimental setups used in this work.

A well-known and commercially equivalent orthopaedic implant material like Ti is widely used today [25]. With research and popularity

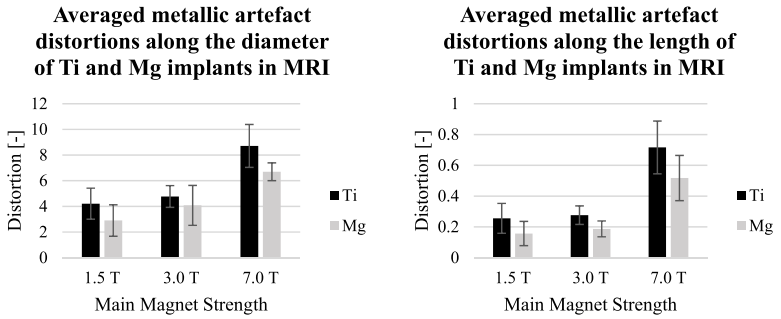

Fig. 4. Averaged artefact distortions of diameter (left) and length (right) measurements of Ti and Mg in MRI.

Table 5
ANOVA and post hoc significance of varied parameters on metallic artefact produced by Ti vs Mg in MRI. Encoding directions are abbreviated as follows: anterior/posterior (AP), head/foot (HF), and right/left (RL).

Parameter	Diameter p-value	Length p-value
B_0 Magnetic Strength	<0.05	<0.05
3 T:1.5 T	0.11	0.73
7 T:1.5 T	<0.05	<0.05
7 T:3 T	<0.05	<0.05
Implant Position	0.68	0.57
Imaging technique (GRE:TSE)	<0.05	<0.05
Phase Encoding Direction	0.62	0.47
HF:AP	0.77	0.67
RL:AP	0.66	0.99
RL:HF	0.98	0.70
Material	<0.05	<0.05

Table 6
ANOVA and post hoc significance of varied parameters on metallic artefact produced by corroded Mg samples for different time points (tp). Encoding directions are abbreviated as follows: anterior/posterior (AP), head/foot (HF), and right/left (RL).

Parameter	Diameter p-value	Length p-value
B_0 Magnetic Strength	<0.05	<0.05
3 T:1.5 T	<0.05	0.40
7 T:1.5 T	<0.05	<0.05
7 T:3 T	<0.05	<0.05
Implant Position	0.60	0.13
Imaging Technique (GRE:TSE)	<0.05	<0.05
Encoding Direction	0.44	0.12
HF:AP	0.51	0.54
RL:AP	0.61	0.82
RL:HF	0.99	0.32
Corrosion Time	<0.05	<0.05
1tp:0tp	0.24	0.98
2tp:0tp	0.21	0.61
3tp:0tp	<0.05	0.11
4tp:0tp	<0.05	0.05
5tp:0tp	<0.05	<0.05
2tp:1tp	0.98	0.95
3tp:1tp	0.98	0.43
4tp:1tp	0.47	0.26
5tp:1tp	0.08	<0.05
3tp:2tp	0.99	0.91
4tp:2tp	0.51	0.79
5tp:2tp	0.09	0.24
4tp:3tp	0.89	0.99
5tp:3tp	0.35	0.82
5tp:4tp	0.94	0.94

of magnesium-based implants increasing, a comparison between the two materials is conceptually appealing. Our findings demonstrate that the Mg-based material outperforms Ti in the *in vitro* environment by producing lower metallic distortion artefacts. Magnetic field perturbations are present around metallic objects in MRI which leads to a modification of hydrogen nuclei precession rates. The change in precession rates results in signal losses or pixel shifts and may manifest in local hypointensities or hyperintensities in MR images. Magnetic field variations are dependent on the magnetic susceptibility of the implant and the surrounding environment (in our case a $CuSO_4$ solution). Since the difference between the magnetic susceptibility of Ti and $CuSO_4$ is pronounced versus the difference between Mg and $CuSO_4$, larger magnetic field distortions are to be expected around a Ti implant.

When introducing corrosion time as a parameter, a decrease in artefact production is noticed as the implant is degraded *in vitro*. As Mg degrades in the body, the base metallic material corrodes forming non-metallic degradation layers composing mainly of MgO and $Mg(OH)_2$ [26]. As such, the base metallic material begins to shrink in volume resulting in a reduced artefact size. This decrease in artefact size is confirmed by our results obtained for a range of *in vitro* corrosion times. The question of how the degradation layer affects artefact production can be answered by analysing the magnetic properties of the degradation layer. Mainly composing of $Mg(OH)_2$ [27], the degradation layer consists of diamagnetic material. As *in vivo* degradation occurs, calcium and magnesium apatite corrosion products additionally form [28]. However, since calcium phosphates are intrinsically diamagnetic, these compounds are trivial with respect to magnetic field interference. Thus, the degradation layer dampens the effects of magnetic field variations caused by the base metallic material. This layer has been reported to be on the micrometer scale [29], which may be assumed to have an almost negligible damping effect.

Standards and norms governed by global organisations, such as ASTM F2119, are referred to by regulatory bodies to ensure patient safety and quality control. Our *in vitro* investigations, based on the ASTM F2119 standard, also considered how parameters such as implant position, encoding direction, and imaging techniques affected artefact production. Of the three, the only parameter that significantly affected artefact production was the MR imaging technique used. In both *in vitro* investigations, GRE imaging generally produced larger artefact size versus fast spin-echo imaging. Spin echo based imaging techniques are less affected by susceptibility artefacts than gradient echo techniques because of the use of a train of refocusing pulses that helps to partially compensate for dephasing of spins caused by metallic objects. Additionally, imaging the diameter of the screw produced larger artefact size than imaging the length of the screw.

Our results add to the literature by providing important insights on how the main magnetic field strength of an MRI system contributes to metallic artefact production. An early study by Ludeke et al. describe show the magnitude of susceptibility artefacts increases with magnetic field strength [30]. This relationship is exemplified in Figs. 4 and 5 where an increase of distortion was observed when moving from 1.5 T to 3.0 T and 7.0 T. It should be noted that conductive implants interact

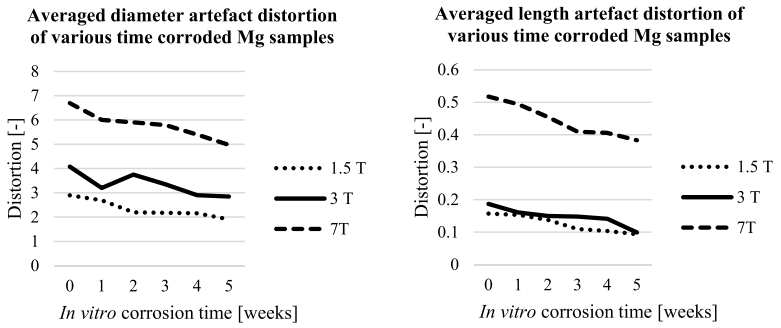

Fig. 5. Averaged diameter (left) and length (right) artefact distortions of Mg-based samples as a function of *in vitro* corrosion time.

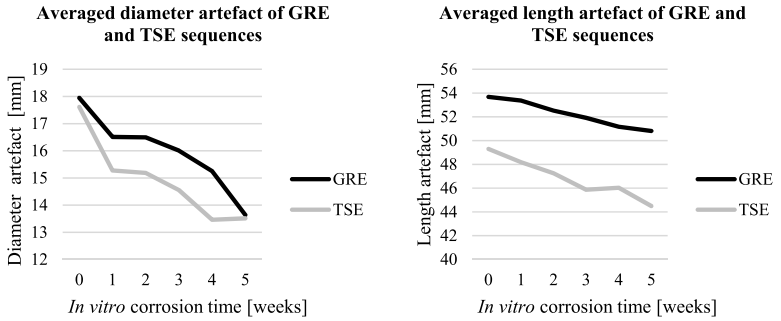

Fig. 6. Averaged diameter (left) and length (right) measured artefacts of Mg-based samples as a function of *in vitro* corrosion time and scanning sequences.

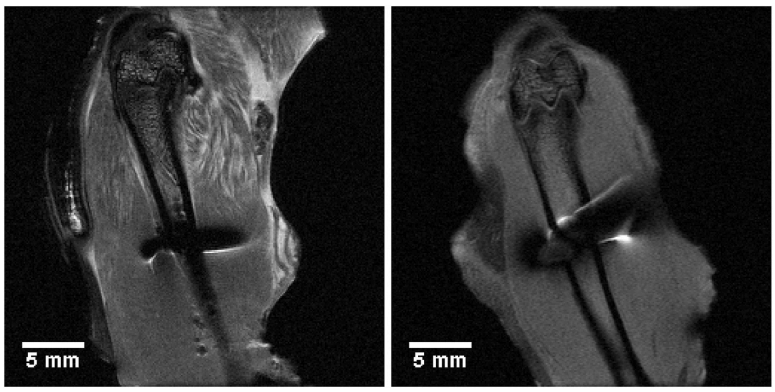

Fig. 7. Example of T1-weighted images of rat femur explants with WE43 and Ti pins implanted transcortical to bone.

with radio frequency (RF) signals from MRI transmitters. These interferences may cause extra artefacts and may even elevate local RF power deposition and energy absorption in the neighbouring region of the implants which may exceed regulatory limits and RF exposure guidelines [31,32].

Explants analysed in this investigation underwent freezing at −20 °C and thawing before scanned in a small animal 7.0 T MRI system. MRI availability could not be synchronised with the euthanasia of the animals and therefore animals needed to be stored. The freezing and thawing cycle has shown to effect MRI by significantly reducing the effective transversal relaxation time T_2* [33]. Such an effect should be considered when interpreting the results. However, the motivation behind our explant analysis is to provide insights into artefact production in hard and soft tissue. Although there were no significant differences obtained for the WE43 samples at different time points, Ti showed an approximately three times larger TAV than the WE43 material.

The clinical results and analysis revealed important information on artefact production of Mg-based implants used to treat scaphoid fractures. Averaging measurements of the four patients included in this investigation followed a similar trend of artefact reduction with patient healing time. The decrease in distortion also provides proof of implant degradation or a loss of metallic base material. More importantly, after averaging all patients and artefacts derived for each imaging plane, an extrapolation of the healing time can be made until the artefact size

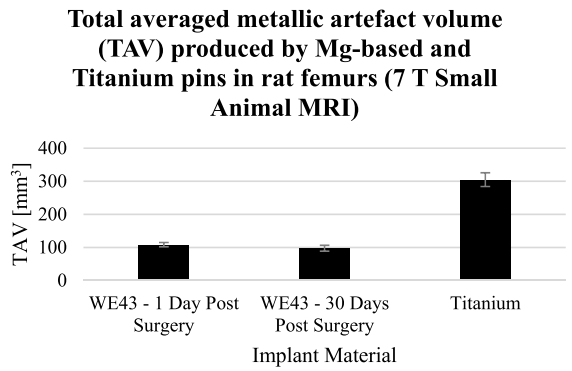

Fig. 8. Total averaged artefact volume produced by pins implanted into rat femurs imaged in 7 T small animal MRI.

reaches zero. Although this extrapolation has limitations (such as implant size), complete disappearance of artefact is approximately reached at 2.1 years, which is in accordance with a one-to-three-year implant resorption period [4,34,35]. Many methods have been employed to track implant degradation rates *in vitro* and *in vivo*, such as computed tomography segmentation and hydrogen gas release [36]. The reduction in metallic artefact size measured in MRI with progressing degradation may offer a viable alternative for screw degradation monitoring and tracking.

This investigation utilised two parameters to quantify artefact production caused by the Mg-based and Ti implants. Distortion quantifications were employed in the *in vitro* measurements while total artefact volume (TAV) was employed in the *ex vivo* and clinical analysis. The inclusion of two measurement methods was chosen to describe the artefact production behaviour of the implants in more than one way. Analysing the two measured quantities show an agreement in the decline of metallic distortion trend of Mg during the degradation process.

Metal artefact reduction techniques are widely used today to negate the effects of metallic implants in MRI [37]. Various specialised software and MRI vendors provide dedicated imaging techniques tailored for reducing metallic artefacts. Since these approaches vary from MRI vendor to vendor, our study excluded their impact as it is out of the scope of this study. However, the literature reports that some metal artefact reduction techniques do not produce statistically significant results when applied to Mg [24]. Examining the efficacy of these metal artefact reduction techniques on Mg-based material warrants further investigation.

A limitation of the *in vitro* aspect of this study is found in the natural behaviour of Mg itself. The inherent corrosion process of the implants made it impractical for samples to be tested more than once due to the interaction with $CuSO_4$ solution. Regarding explant analysis, the movement of blood is avoided in the *ex vivo* animal studies so that blood motion artefacts are eliminated. An increase in explant samples and clinical patients would enhance the statistical power of our findings.

Future studies should include the examination of different animal models to gain insights for other orthopaedic applications or solutions. Alternative *in vitro* implant degradation methods can be used to mimic specific environments. These methods should also be analysed to investigate how the degradation method affects artefact production. Furthermore, the inclusion of multi-modal data such as clinical computed tomography can be explored in quantifying an implant volume to MRI artefact production ratio.

Assessing the artefact production behaviour of Mg-based implants *in vitro, ex vivo,* and in clinical application provides valuable insights into the material's properties and its implications for MRI image quality. Our results demonstrate that Mg-based implants displayed a decrease in metallic artefact production with implant degradation. As the implant degrades and artefact production decreases, better visualisation of bone healing is achieved. To summarise, the Mg-based implant outperformed the Ti material by inducing lower artefact size.

5. Conclusion

In this investigation, *in vitro, ex vivo,* and clinical studies demonstrate a reduction in artefact size with implant degradation time for Mg-based screws. The largest artefact behaviour or "worst-case" scenario caused by the WE43 implants were found when imaging the non-degraded state in the *in vitro* and *ex vivo* experiments. In the clinical study, the largest

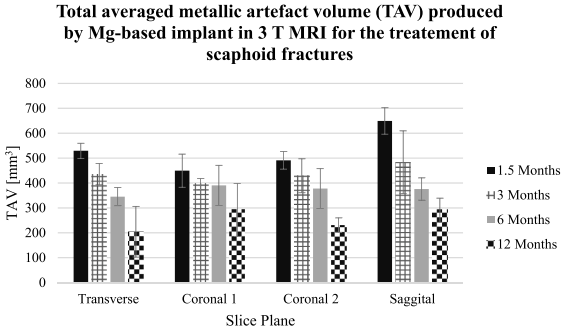

Fig. 10. Total artefact volume produced by Mg-based implant as a function of healing time in different slice planes in 3 T MRI.

Fig. 9. T2-weighted images of scaphoid with Mg-based screw one (left), three months (middle), and twelve months (right) after surgery. White arrows indicate position of implant.

TAV was observed when imaging the implant at 1.5 months in the sagittal plane. When compared against Ti-based implants, the Mg-based material induces significantly lower artefacts. Translational findings from this study suggests that Mg-based implant material should be promoted for future orthopaedic solutions due to lower artefact production. Further clinical studies are required to determine degradation rates based on artefact production as an alternative approach for degradation tracking.

CRediT authorship contribution statement

Jonathan Espiritu: Conceptualization, Methodology, Software, Validation, Formal analysis, Investigation, Resources, Data curation, Writing – original draft, Visualization. **Mostafa Berangi:** Investigation, Data curation. **Christina Yiannakou:** Formal analysis, Investigation, Resources, Data curation. **Eduarda Silva:** Methodology, Resources. **Roberto Francischello:** Data curation, Resources. **Andre Kuehne:** Investigation, Data curation, Writing – review & editing, Supervision. **Thoralf Niendorf:** Resources, Writing – review & editing. **Sören Könneker:** Methodology, Resources, Data curation. **Regine Willumeit-Römer:** Conceptualization, Supervision, Project administration, Funding acquisition. **Jan-Marten Seitz:** Conceptualization, Validation, Resources, Writing – review & editing, Supervision, Project administration, Funding acquisition.

Declaration of competing interest

Authors Kuehne and Berangi are employees of MRI.TOOLS GmbH. Author Niendorf is CEO and founder of MRI.TOOLS GmbH. Syntellix AG is a medical technology manufacturer of metallic and bio-absorbable clinical implants. Authors Espiritu and Seitz are employed as Research Associate and Chief Technical Officer, respectively.

Acknowledgements

We would like to thank Eileen Höltje and Fabian Willers from Syntellix AG (Hannover, Germany) and Roman Leicht from MRI.TOOLS GmbH (Berlin, Germany) for their support with the experiments. We would also like to acknowledge the help from Petra Keilberg, Gianni Novani, Hana Hlavata, and Matteo Bianchi from the Fondazione Toscana Gabriele Monasterio Hospital (Pisa, Italy) and Luca Menichetti from the Institute of Clinical Physiology, National Research Council (Pisa, Italy) for their support. This project has received funding from the European Union's Horizon 2020 research and innovation programme under the Marie Skłodowska-Curie grant agreement No 811226.

References

[1] B. Heublein, R. Rohde, V. Kaese, M. Niemeyer, W. Hartung, A. Haverich, Biocorrosion of magnesium alloys: a new principle in cardiovascular implant technology? Heart 89 (6) (2003) 651–656.
[2] G. Marcucci, M.L. Brandi, Kyphoplasty and vertebroplasty in the management of osteoporosis with subsequent vertebral compression fractures, Clin. Cases Mineral Bone Metabol. 7 (1) (2010) 51–60.
[3] H. May, Y.A. Kati, G. Gumussuyu, T.Y. Emre, M. Unal, O. Kose, Bioabsorbable magnesium screw versus conventional titanium screw fixation for medial malleolar fractures, J. Orthop. Traumatol. 21 (9) (2020).
[4] C. Plaass, C. von Falck, S. Ettinger, L. Sonnow, F. Calderone, A. Weizbauer, J. Reifenrath, L. Claassen, H. Waizy, K. Daniilidis, C. Stukenborg-Colsman, H. Windhagen, Bioabsorbable magnesium versus standard titanium compression screws for fixation of distal metatarsal osteotomies – 3 year results of a randomized clinical trial, J. Orthop. Sci. 23 (2) (2018) 321–327.
[5] R. Biber, J. Pauser, M. Brem, H.J. Bail, Bioabsorbable metal screws in traumatology: a promising innovation, Trauma Case Rep. 8 (2017) 11–15.
[6] H. Brar, J. Wong, M. Manuele, Investigation of mechanical and degradation properties of Mg-Sr and Mg-Zn-Sr alloys for use as potential biodegradable implants materials, J. Mech. Behav. Biomed. Mater. 7 (2012) 87–95.
[7] A. Chatterjee, C. Harmath, A. Oto, New prostate MRI techniques and sequences, Abdominal Radiol. 45 (2020) 4052–4062.
[8] P. Stroman, H. Warren, G. Ioachim, J. Powers, K. McNeil, A comparison of the effectiveness of functional MRI analysis methods for pain research: the new normal, PLoS One 15 (12) (2020).
[9] C. Nunez-Peralta, J. Alonso-Perez, J. Diaz-Manera, The increasing role of muscle MRI to monitor changes over time in untreated and treated muscle diseases, Curr. Opin. Neurol. 33 (5) (2020) 611–620.
[10] D.P. Frush, K. Applegate, Computed tomography and radiation: understanding the issues, J. Am. Coll. Radiol. 1 (2) (2004) 113–119.
[11] E. Weidman, K. Dean, W. Rivera, M. Loftus, T. Stokes, R. Min, MRI saftey: a report of current practise and advancements in patient preparation and screening, Clin. Imag. 39 (6) (2015) 935–937.
[12] P.M. Jungmann, C.A. Agten, C.W. Pfirrmann, R. Stutter, Advances in MRI around metal, J. Magn. Reson. Imag. 46 (4) (2017) 972–991.
[13] J. Espiritu, M. Meier, J.-M. Seitz, The current performance of biodegradable magnesium-based implants in magnetic resonance imaging: a review, Bioact. Mater. 6 (12) (2021) 4360–4367.
[14] Azo Materials, Magnesium Elektron WE43 Alloy (UNS M18430), 18 June 2013 [Online]. Available: https://www.azom.com/article.aspx?ArticleID=9279. (Accessed 7 October 2021).
[15] ASTM International, ASTM standard F3268-18a, in: Standard Guide for in Vitro Degradation Testing of Absorbable Metals, West Conshohocken, PA, 2018.
[16] ASTM International, ASTM standard F2119-07, in: Standard Test Method for Evaluation of MR Image Artifacts from Passive Implants, West Conshohocken, PA, 2013.
[17] V. Hurst, A. Ahluwalia, S. Alam, M. Avey, M. Baker, W. Browne, A. Clark, I. Cuthill, U. Dirnagl, M. Emersion, P. Garner, S. Holgate, D. Howells, N. Karp, S. Lazic, K. Lidster, C. MacCallum, M. Macleod, E. Pearl, O. Petersen, et al., The ARRIVE guidelines 2.0: updated guidelines for reporting animal research, PLoS Biol. 18 (7) (2020).
[18] J.F. Debatin, S.N. Nadel, H. Sostman, C. Spritzer, A.J. Evans, T.M. Grist, Magnetic resonance imaging—Cardiac ejection fraction measurements, Invest. Radiol. 27 (3) (1992) 198–203.
[19] S. Könneker, K. Krockenberger, C. Pieh, C. von Falck, B. Brandewiede, P. Vogt, M. Kirschner, A. Ziegler, Comparison of SCAphoid fracture osteosynthesis by MAGnesium-based headless Herbert screws with titanium Herbert screws: protocol for the randomized controlled SCAMAG clinical trial, BMC Muscoskel. Disord. 20 (2019) 357.
[20] A. Chan, J. Tetylaff, D. Altman, A. Laupacis, P. Gotzsche, K. Krleza-Jeric, A. Hrobjartsson, H. Mann, K. Dickersin, J. Berlin, C. Dore, W. Parulekar, W. Summerskill, T. Groves, K. Schulz, H. Sox, F. Rockhold, D. Rennie, D. Moher, SPIRIT 2013 statement: defining standard protocol items for clinical trials, Ann. Intern. Med. 158 (3) (2013) 200–207.
[21] CONSORT Group, CONSORT 2010 Statement: updated guidelines for reporting parallel group randomised trials, PLoS Med. (2010).
[22] T. Ernstberger, G. Buchhorn, G. Heidrich, Intervertebral test spacers and postfusion MRI artifacting: a comparative in vitro study of magnesium versus titanium and carbon fiber reinforced polymers as biomaterials, Open Med. 4 (4) (2009) 496–500.
[23] L. Fili, R. Luechinger, T. Frauenfelder, S. Beck, R. Guggenberger, N. Farshad-Amacker, G. Andreisek, Metal-induced artifacts in computed tomography and magnetic resonance imaging: comparison of a biodegradable magnesium alloy versus titanium and stainless steel controls, Skeletal Radiol. 44 (6) (2015) 849–856.
[24] L. Sonnow, S. Könneker, P.M. Vogt, F. Wacker, C. von Falck, Biodegradable magnesium Herbert, BMC Med. Imag. 17 (16) (2017).
[25] M.S.K. Kaur, Review on titanium and titanium based alloys as biomaterials for orthopaedic applications, Mater. Sci. Eng. C 102 (2019) 844–862.
[26] J. Seitz, R. Eifler, F. Bach, H. Maier, Magnesium degradation products: effects on tissue and human metabolism, J. Biomed. Mater. Res. 102 (10) (2014) 3744–3753.
[27] R. Rettig, S. Virtanen, Composition of corrosion layers on a magnesium rare-earth alloy in simulated body fluids, J. Biomed. Mater. Res. 88A (2) (2008) 359–369.
[28] J. Seitz, R. Eifler, W. Bach, H. Maeir, Magnesium degradation products: effects on tissue and human, J. Biomed. Mater. Res. 102 (10) (2013) 3744–3753.
[29] R. Willumeit-Römer, The interface between degradable Mg and tissue, JOM 71 (4) (2019) 1447–1455.
[30] K.M. Lüdeke, P. Röschmann, R. Tischler, Susceptibility artefacts in NMR imaging, Magn. Reson. Imag. 3 (4) (1985) 329–343.
[31] International Electrical Commision, International standard, medical equipment - Part 2: particular requirements for the safety of magnetic resonance equipment for medical diagnosis, 2nd Revision, in: International Electrotechnical Commission 60601-2-33, 2002, pp. 29–31.
[32] ICNIRP, Guidelines for limiting exporsure to time-varying electric, magnetic, and electromagnetic fields (up to 300 GHz), Health Phys. 74 (4) (1998) 494–522.
[33] S.L. Pownder, P.H. Shah, H.G. Potter, M.F. Koff, The effect of freeze-thawing on magnetic resonance imaging T2* of freshly harvested bovine patellar tendon, Quant. Imag. Med. Surg. 5 (3) (2015) 368–373.
[34] H. Waizy, J. Diekmann, A. Weizbauer, J. Reifenrath, I. Bartsch, V. Neubert, R. Schavan, H. Windhagen, In vivo study of a biodegradable orthopedic screw (MgYREZr-alloy) in a rabbit model for up to 12 months, J. Biomater. Appl. 28 (5) (2013) 667–675.

[35] H. Waizy, J. Seitz, J. Reifenrath, A. Weizbauer, F. Bach, A. Meyer-Lindenberg, B. Denkena, H. Windhagen, Biodegradable magnesium implants for orthopedic applications, J. Mater. Sci. 48 (2013) 39–50.
[36] L. Liu, K. Gebresellasie, B. Collins, H. Zhang, Z. Xu, J. Sankar, Y. Lee, Y. Yun, Degradation rates of pure zinc, magnesium, and magnesium alloys measured by volume loss, mass loss, and hydrogen evolution, Appl. Sci. 8 (9) (2018) 1459.
[37] M. Reichert, T. Ai, J.N. Morelli, M. Nittka, U. Attenberger, V.M. Runge, Metal artefact reduction in MRI at both 1.5 and 3.0Tusing slice encoding for metal artefact correction and view angle tilting, Br. J. Radiol. 88 (2015) 1048.

Chapter 8

Radiofrequency induced heating of biodegradable orthopaedic screw implants during magnetic resonance imaging

In this work, translational aspects of medical device and material development are investigated. Ensuring patient safety during medical imaging is of the utmost importance during clinical follow-up. It has been demonstrated that permanent implants have shown to heat surrounding tissue during MRI. However, there is no current information on the influence of the degradation layer of Mg-based orthopaedic screws. In this study, WE43 implants were degraded *in vitro* for material and heating investigations following international standards. It is shown that the heating profile of the WE43 screws decreases with degradation time. Therefore, the highest potential safety risk in this regard may be after initial screw implantation. Clinicians and MRI technicians may use this data to prepare a vigilant imaging schedule for post-operative patient care.

The results have been published in the journal *Bioactive Materials* and has been reproduced with permission.

Bioactive Materials 25 (2023) 86–94

Contents lists available at ScienceDirect

Bioactive Materials

journal homepage: www.keaipublishing.com/en/journals/bioactive-materials

Radiofrequency induced heating of biodegradable orthopaedic screw implants during magnetic resonance imaging

Jonathan Espiritu [a,*], Mostafa Berangi [b,c,d], Hanna Cwieka [e], Kamila Iskhakova [e], Andre Kuehne [b], D.C. Florian Wieland [e], Berit Zeller-Plumhoff [e], Thoralf Niendorf [b,c,d], Regine Willumeit-Römer [e], Jan-Marten Seitz [a]

[a] Syntellix AG, Hannover, Germany
[b] MRI.TOOLS GmbH, Berlin, Germany
[c] Charité – Universitätsmedizin Berlin, Corporate Member of Freie Universität Berlin and Humboldt Universität zu Berlin, Berlin, Germany
[d] Berlin Ultrahigh Field Facility (B.U.F.F.), Max-Delbrueck Center for Molecular Medicine in the Helmholtz Association, Berlin, Germany
[e] Institute of Metallic Biomaterials, Helmholtz Zentrum Hereon, Geesthacht, Germany

ARTICLE INFO

Keywords:
Biodegradable implants
Magnesium
Medical imaging
Magnetic resonance imaging
Patient safety

ABSTRACT

Magnesium (Mg)-based implants have re-emerged in orthopaedic surgery as an alternative to permanent implants. Literature reveals little information on how the degradation of biodegradable implants may introduce safety implications for patient follow-up using medical imaging. Magnetic resonance imaging (MRI) benefits post-surgery monitoring of bone healing and implantation sites. Previous studies demonstrated radiofrequency (RF) heating of permanent implants caused by electromagnetic fields used in MRI. Our investigation is the first to report the effect of the degradation layer on RF-induced heating of biodegradable orthopaedic implants.

WE43 orthopaedic compression screws underwent *in vitro* degradation. Imaging techniques were applied to assess the corrosion process and the material composition of the degraded screws. Temperature measurements were performed to quantify implant heating with respect to the degradation layer. For comparison, a commercial titanium implant screw was used.

Strongest RF induced heating was observed for non-degraded WE43 screw samples. Implant heating had shown to decrease with the formation of the degradation layer. No statistical differences were observed for heating of the non-degraded WE43 material and the titanium equivalent. The highest risk of implant RF heating is most pronounced for Mg-based screws prior to degradation. Amendment to industry standards for MRI safety assessment is warranted to include biodegradable materials.

1. Introduction

Rise in aging population, technological advancements, and availability of better medical facilities drive the prevalence of orthopaedic implantations [1]. With the resorption of biodegradable materials, the need for implant removal using secondary surgery is averted along with significant reduction of patient burden and health care costs. Interest in magnesium (Mg)-based materials has shown exponential increase as a contemporary alternative to traditional permanent implants [2–5]. The appeal is warranted by the material's appropriate biocompatibility [6] and mechanical properties [3].

Postoperative care of orthopaedic implants is aided by imaging of implantation sites to monitor the healing process of surrounding bone and tissues, and to assess the implant status [7–9]. MRI presents a viable approach for the examination of implantation sites due to its superb bone-soft tissue contrast and the use of non-ionizing radiation. Mg-based implants have shown to be compatible with MRI providing good visualization due to their lower metallic artefact production [9]. However, the metallic and electrically conductive nature of Mg-based and other metallic implants constitutes challenges for MRI. Implant and tissue heating due to interactions between conductive implants and electromagnetic (EM) fields may lead to tissue heating and thus compromise patient safety [10].

Implant heating may be induced by exposure to two time-varying

Peer review under responsibility of KeAi Communications Co., Ltd.
* Corresponding author.
E-mail address: espiritu@syntellix.com (J. Espiritu).

https://doi.org/10.1016/j.bioactmat.2023.01.017
Received 23 November 2022; Received in revised form 19 January 2023; Accepted 21 January 2023
Available online 23 January 2023

fields required for MRI: RF field transmission (B_1^+) induced heating and heating caused by switched magnetic field gradients (B_G) [10]. MRI uses radiofrequency (RF) power transmission for signal and image generation. Having base frequencies in the MHz, B_1^+ is provided by a transmit RF coil used for spin excitation. Spatial encoding used for MR image generation is achieved by switched magnetic field gradients B_G, with frequencies found in the kHz range [11,12]. Following Faraday's law, time-varying magnetic fields are inherently accompanied by electric fields (E-fields), generating so called eddy currents. Induced eddy currents can deposit power into implants and further induce secondary EM fields around the implant, which may cause tissue heating. Owing to the material, shape, location, orientation, and degradation state of a conductive implant, the level of RF power deposition induced heating and heating induced by switched magnetic field gradients may vary [13,14].

Due to the geometry of orthopaedic screws, RF heating is of critical concern. The specific absorption rate (SAR) describes the temporal averaged absorbed RF power P_{RF} over time per exposed mass Δm [10]:

$$SAR = \frac{\langle P_{RF} \rangle_t}{\Delta m} = \frac{\sigma \langle |E|^2 \rangle_t}{2\rho}$$

As such, the SAR is governed by tissue parameters and MRI hardware. Electrical conductivity σ and mass density ρ are inherent to the surrounding tissue, while the E-field E is dictated by the imaging hardware. To limit heating and to prevent high SAR, MR techniques and protocols have been modified by reducing the power of RF excitation pulses and by increasing the repetition time between RF excitation pulses. A plethora of reports presents more sophisticated MRI hardware and methodology tailored for mitigation of RF induced implant heating [15–17]. Pioneering approaches include modification of RF transmission fields using RF arrays and parallel transmission with maximum and null current modes [18,19].

The induced eddy currents caused by the effective transmission field B_1^+ are condensed to the surface of the metal due to the "skin effect", a law of electrodynamics. Though the heating of the small implant mass (such as a screw) may be negligible, the secondary (scattered) E-field induced by the eddy currents becomes hazardous at critical locations along the implant [10]. RF currents indirectly induced in the neighbouring tissue by the secondary E-field are thus the major contributor to RF induced heating. Furthermore, thin wires, screws, and other one-dimensional-like geometries may succumb to the "antenna effect". This effect describes intensity peaks when the implant length falls within one-quarter to one-half of the RF wavelength found in tissue [20]. Thus, elevated heating may be observed for thin geometries since the secondary E-field is optimal under these conditions, more predominantly at the implant tip ends.

Prior to market entry, various tests are undertaken to ensure medical devices conform to their respective standards. With support from governmental agencies, international standards have been established to ensure patient safety during MRI studies [10]. Noteworthy standards regarding implant heating in MRI include ASTM F2182 [21], IEC 60601-2-33 [22], and ISO/TS 10974 [23]. To this end, responsibility falls upon manufacturers of medical devices to minimize hazardous risk and uphold patient safety.

Previous studies have documented heating caused by permanent metallic implants in MRI [11,24–26]. Furthermore, particular studies have utilised computational modelling methods to estimate RF-induced heating [27–30]. Mg-based materials have additionally been employed for thermal ablation of tumours utilising the eddy thermal effect [31]. However, the literature does not reveal reports elucidating RF induced heating of biodegradable orthopaedic implants. How the degradation layer can affect potential heating in MRI is of high clinical relevance, still unknown and warrants additional exploration. To close this gap, this study first carefully characterizes the degradation layer of *in vitro* corroded Mg-based biodegradable orthopaedic compression screws (WE43) using micro computed tomography, X-ray diffraction, scanning electron microscopy and energy dispersive X-Ray electron microscopy. This material characterization is followed by an examination of the impact of the degradation layer state on RF-induced heating in MRI of WE43 materials. For evaluation, temperature profiles obtained for WE43 material are benchmarked against temperature profiles derived from a commercial titanium implant screw equivalent. We hypothesise that the degradation layer formed around the base material of a Mg-based biodegradable screw over time disrupts secondary E-field distribution which may lessen RF heating of the surrounding environment, and may benefit MRI aided monitoring of implantation sites.

2. Materials and methods

2.1. Sample preparation

Mg-based (WE43) orthopaedic compression screws (Syntellix AG, Hannover, Germany) 40 mm in length and 3.2 mm in diameter underwent *in vitro* degradation. The WE43 alloy is comprised of magnesium alloyed with Yttrium, Rare Earth Elements, and Zirconium [32]. To compare the heating profile of a non-degraded WE43 sample to alternatives, a titanium commercial equivalent was included (Fig. 1). The WE43 samples were immersed and corroded in a modified ASTM F3268 Standard [33] with Dulbecco's Phosphate Buffered Saline (DPBS). As described by the standard, the temperature of the corrosion medium was kept at 37 ± 1 °C with a pH of approximately 7.4 ± 0.2. A specimen was placed in 2.5 L of the medium which was kept constant and replaced if evaporation were to occur. If a measured pH registered above a pH of 7.6, the corrosion medium was treated with a HCl buffering solution.

24 screws were immersed and degraded in the solution for eight time points (three samples per time point) ranging from one-week to eight-weeks with an increment of one week. Once the specified immersion time elapsed, the samples underwent cleaning with distilled water and were rinsed with ethanol to remove salts and prevent further oxidation. The Ti sample was assumed to have negligible degradation within the time frame of this degradation setup.

2.2. Material characterisation

A randomly selected subset of the degraded screws for each time-period was chosen to be imaged with various techniques to provide qualitative and quantitative data of the degradation layer developed under the chosen corrosion method.

2.2.1. Micro-computed tomography

The *in vitro* degraded screws underwent micro-computed tomography (μCT) to observe changes to the geometry of the screw as corrosion time continued. The samples were first imaged by a laboratory μCT scanner (Phoenix Nanotom by Baker Hughes, Celle, Germany) with scanning parameters described in Table 1. The scans were reconstructed in Datos|x (Baker Hughes, Celle, Germany) where potential movement caused by the rotating stage was corrected using an optimisation function. The raw data was then segmented using Fiji/ImageJ [34] by first applying anisotropic diffusion to reduce noise. Then, a trainable WEKA segmentation [35] was applied to segment the base material, degradation layer, and background. Additionally, the segmented base material was utilised to calculate the mass loss of the degraded samples.

2.2.2. X-ray diffraction

X-ray diffraction (XRD) was performed at P07 side station at the PETRA III storage ring at Deutsches Elektronen-Synchrotron (DESY, Hamburg, DE) [36] to describe the crystalline structure of the degradation layer. An X-ray beam with an energy of 87.1 keV and 0.5 beam size was applied to the top of two-, four-, six-, and eight-week time point screw samples a total of three times each. A Perkin Elmer XRD 1621 Flat Panel Detector (PerkinElmer, Waltham, United States) was placed at

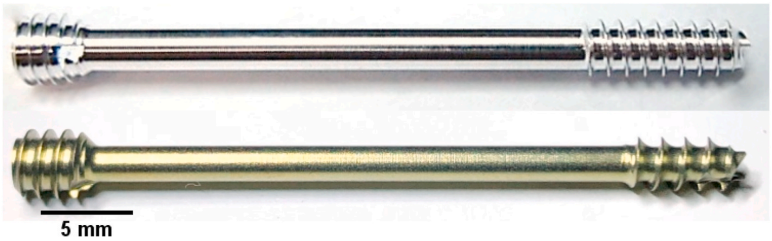

Fig. 1. 40 mm Mg-based orthopaedic compression screw MAGNEZIX® CS ø 3.2 (top) and Ti equivalent (bottom), reproduced under the CC BY-NC-ND 4.0 License [9].

Table 1
μCT measurement parameter details applied to image the degraded WE43 screw samples.

Scanning Parameter	Value
Sample distance [mm]	20
Detector distance [mm]	200
Timing per projection [ms]	2400
Frames per projection	5
Number of images	2000
Voltage [kV]	125
Current [μA]	45
Isotropic voxel size [μm]	5

1.485 m from the samples. The samples were subjected to 0.5 s of exposure time. Lanthanum hexaboride (Lab6) was used as a calibrant. The acquired XRD images were processed using Dawn Science 2.18.0 (Diamond Light Source, Didcot, UK) [37]. Diffractograms were analysed using MATLAB R2018 (The MathWorks Inc., US) and averaged along with a slice in a direction perpendicular to the screw axis. The final plots were normalized according to Mg (101) peak intensity.

2.2.3. Scanning electron microscopy and energy dispersive X-ray spectroscopy

Scanning electron microscopy (SEM) and energy dispersive X-ray spectroscopy (EDX) analysis were employed to characterise the cross section along the longitudinal axis of the degraded screws in terms of qualitative imaging and elemental composition of the degradation layer. Imaging was acquired by a Tescan Vega SB-U III (Tescan, Czech Republic) at Helmholtz-Zentrum Hereon (Geesthacht, Germany). Images were taken in backscattered electron mode (BSE mode) to emphasize the differences between the residual material and the degradation layer. The EDX measurements were performed as mapping of a chosen region of interest. The SEM and EDX measurements details can be found in Table 2. Zero-, Two-, four-, six-, eight-week degraded samples were embedded in methyl methacrylate liquid and powder (Demotec®, Demotec, Germany) before being ground and polished on a Saphir 320/Rubin 520 machine (QATM, Advanced Materialography, Germany). Subsequently, the samples were sputtered with carbon to provide appropriate conductivity for the SEM and EDX measurements.

2.3. Temperature measurements during MRI examination

A 3.0 T (Skyra Fit, Siemens, Erlangen, Germany) MRI scanner was used for *in vitro* measurements. The various degraded samples and titanium equivalent underwent a procedure adapted from ASTM F2182 [21]. The MR scanning parameters used during the heating measurements are summarized in Table 3.

Table 2
SEM and EDX measurement parameter details applied to image the degraded WE43 screw samples.

Parameter	SEM	EDX
Voltage [kV]	15	15
Magnification [x]	50	2000
Beam intensity [–]	10	15

A rectangular case with dimensions defined by the ASTM Standard was constructed from acrylic glass and was filled with a phantom gel. The tissue-mimicking phantom was prepared with 1.32 g/L of NaCl (Sigma Aldrich, Taufkirchen, Germany), 10 g/L of polyacrylic acid (Sigma Aldrich, Taufkirchen, Germany), and 25 L of distilled water. Prior to each specimen heating test, local incident field calibration was performed as described by ASTM F2182 [21].

A non-conducting 3D-printed holder was developed to hold the specimen and to guide fibre-optic probes from the thermometry system (model T1; Neoptix Inc., Québec, Canada) to the tips of the implants which define the highest heating points [38]. A total of three probes were used, two placed at the implant ends, and one control probe placed on the opposite side of the phantom to measure heating sans implant influence. The position of the probes was adjusted between every sample scan to ensure the distance between the probes and the implant was consistent. The holder with a single screw sample was placed centred 2 cm from the phantom wall and aligned to the main magnetic field, as this position has been previously determined as the location with maximum heating [39]. The acrylic case was then placed in a Styrofoam insulation container for scanning as illustrated in Fig. 2.

Prior to heating measurements, the gel phantom was brought to scanning room temperature 24 h beforehand. The temperature was recorded 2 min before and 2 min after the scanning sequence was applied at intervals of 1 s. For each sample, one measurement was taken without the sample, and another measurement was taken with the sample placed in the phantom to assess the increase in temperature due to the device itself. Screw samples from weeks six to eight did not

Table 3
MRI scanning parameters used during heating measurements of the screw samples.

B0 Field strength [T]	3.0
RF coil type (transmission)	Body RF coil
RF coil type (reception)	32 channel spine RF array
Imaging technique	Turbo-spin-echo (TSE)
TR [ms]	5820
Inter-echo time TE [ms]	6.8
Echo train length	8
Imaging Plane	Transversal
Excitation flip angle [°]	120
Pulse Width [ms]	1.28
Transmitter Power [W]	90.7
FOV [mm]	450
Matrix size [pixel]	512
Slice thickness [mm]	3.4
Total slices	24
Whole body-SAR [W/kg]	2
Patient Body Weight [kg]	70
Number of Averages	20
Scan time [s]	939

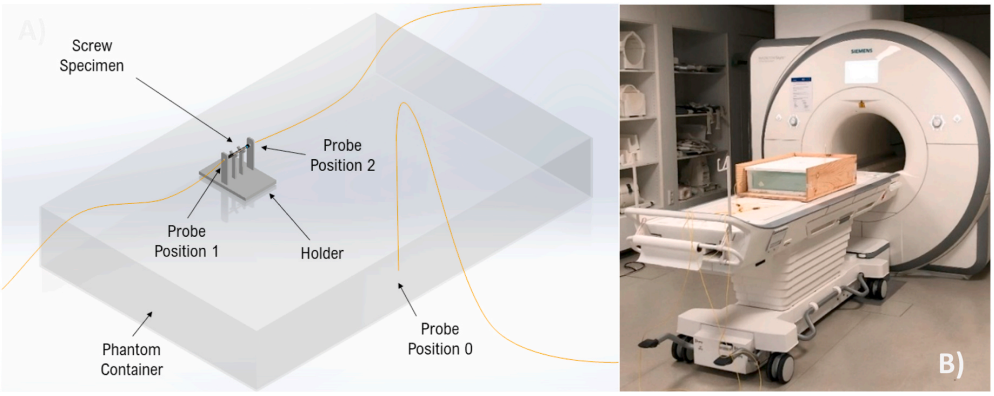

Fig. 2. Heating measurement setup based on ASTM F2182 depicting the MRI scanner (A) and the phantom (B). For the temperature measurements the phantom setup was moved into the isocenter of the MR scanner.

succumb to heating measurements as the samples fractured during the *in vitro* degradation process.

2.4. Statistics

Statistical analyses were performed using RStudio (RStudio, USA). A p-value of <0.05 was chosen to be statistically significant. To compare the increases in temperature and mass loss between the various degraded WE43 time-points, a two-way analysis of variance (ANOVA) was performed. Additionally, the ANOVA test was also applied to determine the differences between the WE43 material and the equivalent titanium implant. If any significant results were determined, a Turkey's post hoc comparison procedure was utilised to perform pairwise comparisons.

3. Results

3.1. Material characterisation

3.1.1. Micro-computed tomography

The degraded specimens were scanned via μCT to capture the physical geometry of both the base material and the degradation products. Time-points after the fifth week were excluded due to specimen breaking during corrosion process. An example is outlined in Fig. 3. Non-uniform pitting corrosion is clearly visible from the μCT images (Fig. 3A). Segmentation applied to the μCT images (Fig. 3B) successfully differentiated base material from the degradation products. From the segmented images, it is evident that the degradation layer unevenly penetrates the base material from the inner canulation and more evidently from the outer surface of the screws. A build-up of degradation product is also visible in the cannulation. A fully realised 3D object file of the base material is visible in Fig. 3C.

The segmented base material was utilised to calculate any significant differences between the mass loss during the selected degradation periods. The statistical tests revealed a significant difference between the degraded timepoints ($p < 0.05$). A summary of the pairwise comparisons are shown in Table 4.

3.1.2. X-ray diffraction

$Mg(OH)_2$, MgO, $MgCO_3$, $CaCO_3$, and $MgHCO_3{\cdot}3H_2O$ degradation products were identified by means of XRD as shown in Fig. 4 (left). The more predominant peaks observed were contributed by $Mg(OH)_2$ and MgO, suggesting the presence of higher crystalline phases of these products. With respect to the time course, the intensity of the $Mg(OH)_2$

Table 4
Post hoc significant differences of paired degradation time points (tp).

Pairwise comparison of degraded tps	p-value
1tp:0tp	<0.05
2tp:0tp	<0.05
3tp:0tp	<0.05
4tp:0tp	<0.05
5tp:0tp	<0.05
2tp:1tp	0.55
3tp:1tp	<0.05
4tp:1tp	<0.05
5tp:1tp	<0.05
3tp:2tp	0.31
4tp:2tp	<0.05
5tp:2tp	<0.05
4tp:3tp	<0.05
5tp:3tp	<0.05
5tp:4tp	0.99

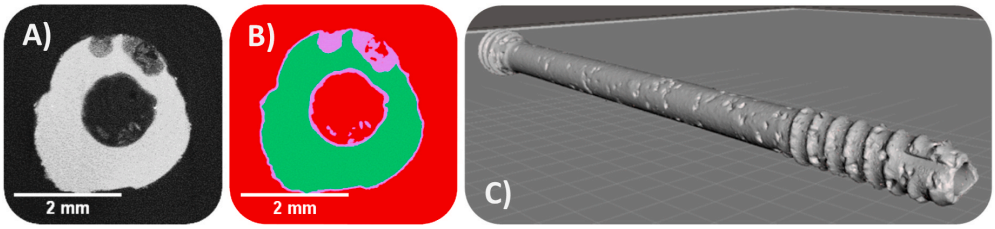

Fig. 3. Exemplary results derived from μCT of degraded specimens. The raw μCT data (A) showing a cross-section approximately 12 mm from the top of the screw is first segmented (B) to create a 3D view (C). The segmented image shows the base metallic material in green, degradation product in purple, and background pixels in red.

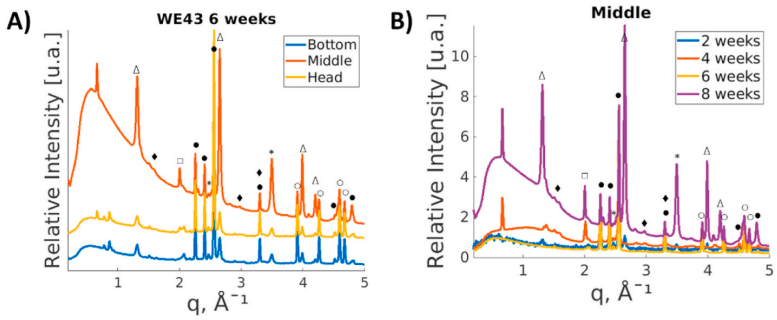

Fig. 4. Diffractograms for the middle section of the screws after two, four, six, and eight weeks in solution (A). Peak assignment is illustrated with the following symbols: ● for Mg, Δ for $Mg(OH)_2$, ○ for MgO, * for $MgCO_3$, ◊ for CaCO3, and □ for $MgHCO_3{\cdot}3H_2O$. Diffractograms of the head, middle, and bottom parts of three averaged samples after eight weeks of immersion time (B). The intensities are normalized with respect to (101) Mg Bragg's peak.

peaks increased with degradation period, while MgO remained at a constant intensity. Additionally, Fig. 4 (right) shows the averaged diffractograms from different locations along the screw. The head, middle, and bottom of the 8-week corroded samples were selected for analysis due to large presence of degradation products. The differences in diffractograms taken at the head and bottom of the screw are negligible. However, there is a significant increase of $Mg(OH)_2$ peaks in the middle section where most degradation products settled within the cannulation. Moreover, most of the diffractograms demonstrated a strong amorphous signal with a peak at 0.55 $Å^{-1}$. Other identified degradation products ($MgCO_3$, $CaCO_3$, $MgHCO_3{\cdot}3H_2O$) did not show significant changes in intensity with time.

3.1.3. Scanning electron microscopy and energy dispersive X-ray

Fig. 5 shows SEM images captured with 50x magnification of the degraded WE43 screw heads of the cannulated screws over the immersion time. For comparison a non-degraded sample (0 weeks) is used as a reference. Material degradation is clearly visible with the loss of screw threads as immersion time persists. The regular and cracked degradation layer develops in the same fashion in the cannulation of the screw as on the exterior surface. A decrease in surface smoothness is noticeable as corrosion continues.

EDX was applied to identify and determine the distribution of elements throughout the degradation layer. The following elements were detected: Mg, Y, Nd, Zr, Na, Cl, K, P, O, and Ca. The elemental composition was measured as maps and is plotted as graphs of weight percentage (Fig. 6). Based on SEM and EDX results, the main composition of the degradation layer at two weeks is made of Mg and O. Y, Zr, and Nd are found to have high concentration near the top of the degradation layer and decreases to expected values near the base material. After four weeks, Mg and O remain the main components of the degradation layer with both contents above 25%. The distribution of the other elements remains constant throughout the whole degradation layer with O significantly decreasing near the base material. Results after six weeks display similar distribution of elements as seen after four weeks. About half of the degradation layer is now comprised of O. The degradation layer is thick with many visible cracks. At eight weeks, the degradation is at the highest and is spread well into the cannulation. The degradation layer consists of mainly Mg and O (25% and 50% respectively) with Mg rapidly growing as a residual material. There are no observations of smooth changes at the interface between the degradation layer and base material of the screw.

3.2. Heating measurements during MRI examination

Results derived from the heating measurements are summarized in Fig. 7. As corrosion time increased, a decline in maximum temperature change ΔT was observed, however, there was no apparent quantifiable correlation. The highest average temperature increase was seen at 0-weeks corrosion at 100% of the screw volume and the lowest temperature increase was observed at 3-weeks of corrosion time. The maximum RF-induced heating was measured to be $\Delta T = 1.20 \pm 0.29$ °C for the non-degraded WE43 screw and $\Delta T = 1.16 \pm 0.18$ °C for the titanium equivalent. However, no significant differences were observed.

4. Discussion

The increasing number of orthopaedic implantations continues to drive the need for post-surgery imaging to monitor bone healing and implant placement. MRI of implantation sites provides excellent bone-tissue contrast that may aid postoperative care of orthopaedic implants. Careful risk assessment of RF induced heating of conducting implants is mandatory before MRI can be applied for monitoring of implantation sites. Recognizing this need and opportunity, this study adds to the literature by examining the material characteristics, corrosion dynamics, and the influence of the degradation layer on RF-induced heating of Mg-based implants.

Unlike standard titanium and stainless-steel material, Mg-based implants degrade over time when exposed to bodily fluid. As a result, the chemical composition of the implant and physical geometry change as healing occurs. Since material composition and implant form influence the RF-heating of metallic implants, our study used various imaging techniques to characterise *in vitro* corroded WE43 screws. It is noted that the *in vitro* degradation technique employed in this investigation

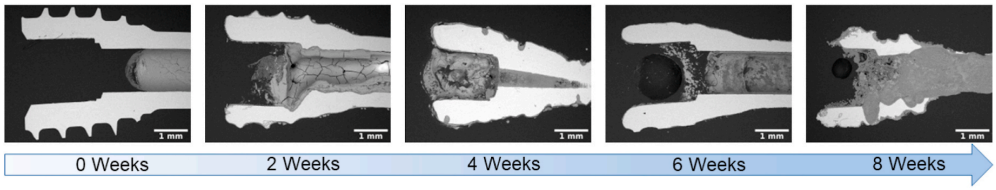

Fig. 5. SEM images of the WE43 screw heads after several time points of *in vitro* immersion.

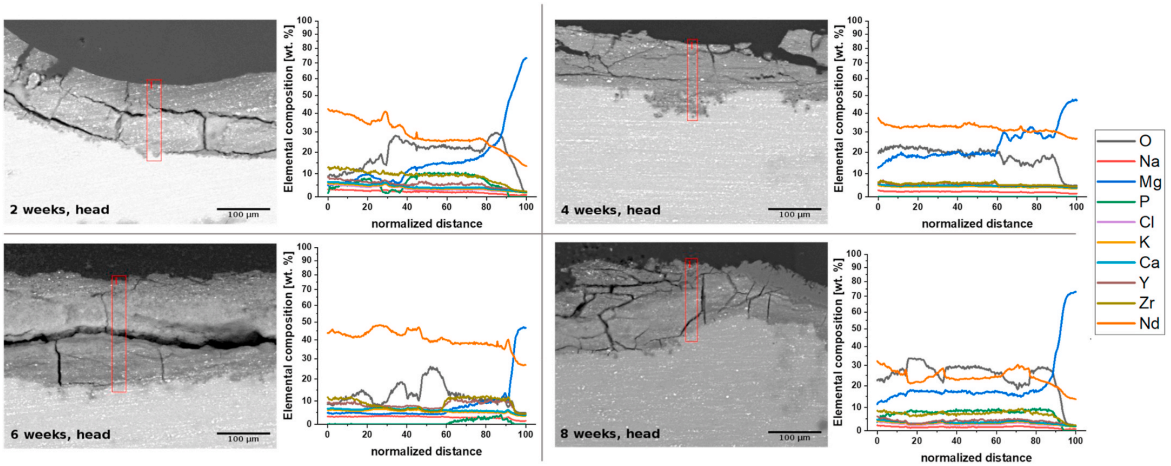

Fig. 6. Regions of interest measured EDX maps and graphs of weight percentage depending on normalized distance where 0 is the sample surface and 100 is the residual metal. Results of samples after 2, 4, 6 and 8 weeks of *in vitro* immersion.

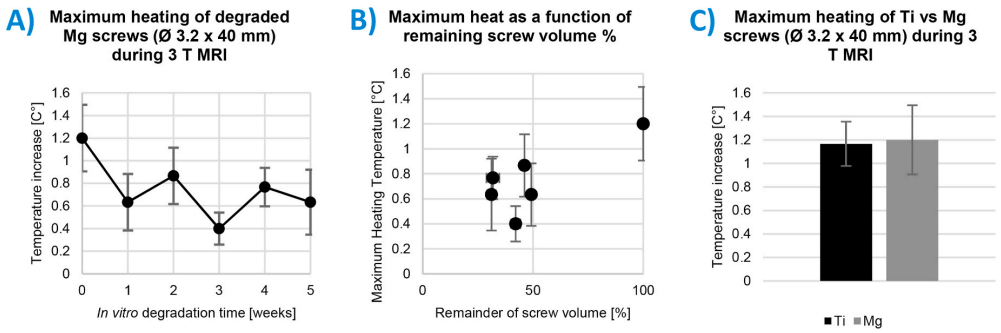

Fig. 7. Maximum RF-induced temperature heating at the tip of the screws of different length. A: influence of corrosion time on heating. B: maximum heating as a function of remainder screw volume. C: Comparison of Mg to commercial Ti equivalent.

provides only a partial impression of the complex processes in which degradation occurs in the human body, because our *in vitro* approach does not factor in the influence of biological material or cell adhesion [40].

The results derived from µCT and SEM provide insight into the physical corrosion of the screw structure *in vitro,* which is supported by previous literature [40]. The segmented µCT images reveal a statistically significant reduction in base metallic WE43 material surrounded by degradation layer as weeks progress. The non-uniformity of degradation is apparent with pit formations of various sizes. SEM images depict surface cracking of the irregular degradation layer. Additionally, the loss of threads is apparent in both µCT and SEM images as the original screw shape begins to lose definition and transforms into a tube-like structure over time. The pitting behaviour seen in Figs. 3 and 5 causes a non-uniform degradation layer and a buildup of degradation product found in the canulation of the screw.

XRD findings identified different crystalline degradation products along various locations of the screw in Fig. 4. The main degradation products were found to be $Mg(OH)_2$ and MgO, which correlates with published papers [41–44]. At eight weeks of degradation, a strong amorphous signal is visible in the middle of the screw, originating from the cannulation which is confirmed by µCT. The presence of this signal suggests the degradation products found in the middle of the screw may possess a non-crystalline amorphous phase, which may be contributed by phosphorus and calcium components [45]. Additionally, a strong Mg $(OH)_2$ signal increases over time and may be the main precipitant in the cannulation of the screw. The lower signals analysed at both ends of the screw suggest a lower presence of degradation material. Thus, the degradation material is mostly composed of $Mg(OH)_2$ in both crystalline and amorphous forms, which is supported by previous works [40].

The EDX analysis revealed high contents of Mg and O as main composition of the degradation layer, confirming degradation products identified in the XRD results. As time persists, O is determined to take further composition of the degradation material. Interestingly, Zr and the rare-earth elements Nd and Y were found to have high concentrations near the surface of the degradation layer, decreasing towards the base material. This "sticking" of rare-earth elements to the surface of the degradation layer is caused by mobility of Yttrium [46]. EDX results suggest compounds consisting of the rare-earth elements are situated near the surface of the samples. Though undetected by XRD in this investigation, previous *in vitro* studies show the identification of Y_2O_3, $Mg_{24}Y_5$, and $Mg_{24}Nd_5$ [47,48].

RF induced heating of conducting implants is influenced by a material's electromagnetic properties and by the physical geometry. Elevated heating is expected at implant lengths half to a quarter of 3.0 T RF wavelengths (13–6.5 cm in tissue) in the body [10], which is not relevant for the 40 mm length implants investigated in this experiment. Since heating is dependent on implant length and main magnetic field

strength, the measured temperatures of the selected 40 mm length screws analysed in this investigation may not be representative for all degradable systems. Moreover, the reported material temperature increases of approximately 1 °C is well under the threshold in which thermal necrosis may occur at 47 °C [49]. Though there were no significant differences between the materials, the non-degraded WE43 implant yielded a minor increase in RF heating over the titanium equivalent (Fig. 7). Winter et al. simulated the secondary E-field distribution of a linear implant while varying the conductivity of the material [10]. The scattered secondary field was found to create hotspots at the implant tips as the conductivity of the material increased. As such, WE43 is reported to have a higher conductivity than titanium [50], which may justify the marginally elevated heating measured. However, Capek et al. have investigated the assumption that current distribution on perfect electric conductors and good conductors (such as copper, aluminum, and silver) are equal [51]. Therefore, similar heating profiles between WE43 materials and titanium are not expected to be significantly different as noted in Fig. 7.

As degradation occurs, not only does the physical geometry of the WE43-based screws change, but the material composition of the implant surface alters as well. As a result, the heating profile of the implant changes as the material corrodes. Our results in Fig. 7 demonstrate that the maximum heating exists at the earliest stage prior to corrosion, more specifically, highest heating at original and largest metallic volume prior to degradation, which is supported by previous work [31]. Although there are no significant differences highlighted, the maximum temperature change found for the degraded implants decreases with degradation time. As corrosion persists two complimentary processes occur, (1) the degradation layer continues to develop as (2) the base metallic material reduces.

The base metallic WE43 material degrades over time transforming the compression screw geometry into a potential one-dimensional or wire-like structure. There is minimal reduction in screw length as the implant degrades. The overall diameter of the base material of WE43 decreases during corrosion. Previous investigations demonstrated that maximum temperature rises caused by RF-heating of thin wires during MRI studies increase as diameter decreases [52]. Armenean et al. describe that the increase in temperature due to the wire diameter reduction is caused by an increased secondary E-field. Subsequently, an increased secondary E-field is developed onto the neighbouring tissue or material. Nonetheless, this finding is not in accordance with the temperature changes observed by our study. This indicates that the developing degradation layer may play a greater influence in the heating profile of Mg-based materials.

As verified by the XRD and EDX results, the $Mg(OH)_2$ layer along with other non-crystalline products continue to develop during degradation and coats the surface of the implant. The physical nature of the degradation layer and its electromagnetic properties influence the heating profile of the corroded screws twofold. First, the induced secondary E-field sensed by the conductive tissue may be dampened by the poorly conductive nature inherent to $Mg(OH)_2$ surrounding the base metallic material. Second, the physical corrosion resulting in a non-smooth surface of the material may disrupt the development of the secondary E-field. Our results demonstrate various sizes of pitting formation and developed surface roughness within the cannulation and on the surface of the screw. The overall surface smoothness is decreased as corrosion persists, which has shown to decrease the “skin effect” of EM fields and therefore reduce current density at the surface of the material [53–55]. Additionally, the secondary E-field may further be hindered by the anisotropic nature of the amorphous degradation material found in the cannulation and the non-uniform sticking of heavier rare-earth metallic elements on the surface of the material. However, the influence of the amorphous material and rare-earth elements on the secondary E-field requires further investigation. As a result, the development of the degradation layer over time may reduce the maximum heating detected by surrounding environment.

The intrinsic degradation capability of Mg-based implants introduces limitations into this investigation. The reactive characteristic of Mg-based alloys prohibits samples from being tested more than once due to the interaction with the water-based phantom medium. As a result, multiple samples must be prepared for each time-point which ultimately differ based on the non-uniform corrosion, which may be the main contributor to the variations in recorded measurements. Additionally, WE43 samples could not be placed in the phantom for extended periods of time, as bubble formation (hydrogen gas) would occur. Although the surrounding area of the temperature probes were verified to be bubble-free prior to measurements, few millimetre-sized bubble formation was seen sparsely formed on the implant due to the corrosion process. This concern justifies an amendment to the ASTM F2182 procedures to include verified and standardised protocols to map RF-induced heating caused by biodegradable materials using MR thermometry [56]. Our investigation focuses on utilising industry *in vitro* standards and testing methodologies as a mandatory precursor to *in vivo* or clinical studies, which would provide further specific information on the impact of the degradation layer on RF induced heating of biodegradable orthopaedic screw implants during MRI. Animal studies would provide further insight on heat dissipation in live tissue and therefor should be investigated in the future. As such, it is important to note that the phantom measurements described by the ASTM standard generally provide an overestimation of the temperature increase due to the lack of blood perfusion, wet tissue convection, and blood vessel conduction effects, all of which would be found *in vivo* and in clinical situations. However, previous studies [57] have shown that although the standard implicitly assumes conservative measurements, the heating responses measured in the ASTM phantom can be greatly underestimated for certain situations which should further caution users of the standardised protocol.

Although RF-induced heating has been investigated for multiple permanent implants, future studies should include heating caused by multiple implants made of biodegradable materials. Additionally, heating profiles of broken Mg-based implants resulting in gaps between the original geometry should be investigated as this may occur *in vivo* [58] which presents further safety risks [10]. Moreover, the effects of degradation products in terms of layer depth and other degradation resultants (hydrogen evolution and pH) should similarly be assessed for influence on implant heating.

5. Conclusion

This is the first study that evaluated RF-induced heating of Mg-based orthopaedic implants during MRI. WE43 screws degraded *in vitro* for various time periods causing decreased RF-induced heating during MRI sessions as corrosion time and the formation of the degradation layer progressed. This reduction in RF-induced heating may be instigated by the decline of the “skin effect” caused by a decrease in surface smoothness during degradation layer formation. To conclude, the non-degraded WE43 sample poses the “worst-case” scenario, suggesting highest heating risk occurs directly after material implantation into the body. RF-induced heating was similar for native WE43 screws and for the titanium equivalent. Though the current ASTM standard was successfully utilised in this investigation, our findings support a revision to industry safety standards to encompass testing of conductive implanted medical devices with verified methodologies which may allow for more optimal evaluations of biodegradable materials.

Conflict of interest

Authors Kuehne and Berangi are employees of MRI.TOOLS GmbH. Author Niendorf is CEO and founder of MRI.TOOLS GmbH. Syntellix AG is a medical technology manufacturer of metallic and bio-absorbable clinical implants. Authors Espiritu and Seitz are employed as Research Associate and Director of Research and Development, respectively.

CRediT authorship contribution statement

Jonathan Espiritu: Conceptualization, Data curation, Formal analysis, Investigation, Methodology, Validation, Visualization, Writing – original draft, Writing – review & editing. **Mostafa Berangi:** Data curation, Formal analysis, Investigation, Methodology. **Hanna Cwieka:** Data curation, Formal analysis, Investigation, Visualization, Writing – original draft. **Kamila Iskhakova:** Data curation, Formal analysis, Investigation, Visualization, Writing – original draft. **Andre Kuehne:** Conceptualization, Methodology, Supervision, Writing – review & editing. **D.C. Florian Wieland:** Data curation, Methodology, Resources, Supervision. **Berit Zeller-Plumhoff:** Data curation, Methodology, Resources, Supervision. **Thoralf Niendorf:** Resources, Supervision, Writing – review & editing. **Regine Willumeit-Römer:** Funding acquisition, Project administration, Resources, Supervision, Writing – review & editing. **Jan-Marten Seitz:** Conceptualization, Funding acquisition, Project administration, Resources, Supervision, Writing – review & editing.

Declaration of Competing interest

Authors Kuehne and Berangi are employees of MRI.TOOLS GmbH. Author Niendorf is CEO and founder of MRI.TOOLS GmbH. Syntellix AG is a medical technology manufacturer of metallic and bio-absorbable clinical implants. Authors Espiritu and Seitz are employed as Research Associate and Director of Research and Development, respectively.

Acknowledgements

We would like to thank Eileen Höltje from Syntellix AG (Hannover, Germany) and Roman Leicht from MRI.TOOLS GmbH (Berlin, Germany) for their assistance with the experiments and preparation of materials. This project has received funding from the European Union's Horizon 2020 Research and Innovation Programme under the Marie Skłodowska-Curie Grant Agreement No 811226.

References

[1] A. Hall, E. Dunstan, Day-case total hip arthroplasty: a safe and sustainable approach to improve satisfaction and productivity, and meet the needs of the orthopaedic population, Orthop. Traumatol. 36 (1) (2022) 14–21.
[2] N. Singh, U. Batra, K. Kumar, N. Ahuja, A. Mahapatro, Progress in bioactive surface coatings on biodegradable Mg alloys: a critical review towards clinical translation, Bioact. Mater. 19 (2023) 717–757.
[3] R.P.S. Krishnan, S. Muthusamy, H. Panchal, M. Alsoufi, A. Ibrahim, A. Elsheikh, Biodegradable magnesium metal matrix composites for biomedical implants: synthesis, mechanical performance, and corrosion behavior -A review, J. Mater. Res. Technol. 20 (2022) 650–670.
[4] Z. Ran, W. Dai, K. Xie, Y. Hao, Advances of Biodegradable Magnesium-Based Implants for," Life Research, vol. 5, 2022, p. 7, 1.
[5] J. Espiritu, M. Meier, J. Seitz, The current performance of biodegradable magnesium-based implants in magnetic resonance imaging: a review, Bioact. Mater. 6 (12) (2021) 4360–4367.
[6] J. Seitz, R. Eifler, F. Bach, H. Maier, Magnesium degradation products: effects on tissue and human metabolism, Jounral of Biomedical Materials Research 102 (10) (2013) 3744–3753.
[7] Z. Mosher, J. Sawyer, D. Kelly, MRI safety with orthopedic implants, Orthopedic Clinics 49 (4) (2018) 455–463.
[8] J. Nzenhuis, S. Park, R. Kamondetdacha, A. Amjad, F. Shellock, A. Rezai, MRI and implanted medical devices: basic interactions with an emphasis on heating, IEEE Trans. Device Mater. Reliab. 5 (3) (2005) 467–480.
[9] J. Espiritu, M. Berangi, C. Yiannakou, E. Silva, R. Francischello, A. Kuehne, T. Niendorf, S. Könneker, R. Willumeit-Romer, J. Seitz, Evaluating metallic artefact of biodegradable magnesium-based implants in magnetic resonance imaging, Bioact. Mater. 15 (2022) 382–391.
[10] L. Winter, F. Seifert, L. Zilberti, M. Murbach, B. Ittermann, MRI-Related heating of implants and devices: a review, J. Magn. Reson. Imag. 53 (6) (2020) 1646–1665.
[11] A. Arduino, U. Zanovello, J. Hand, L. Zilberti, B.R.M. Chiampi, O. Bottauscio, Heating of hip joint implants in MRI: the combined effect of RF and switched-gradient fields, Magn. Reson. Med. 85 (6) (2021) 3447–3462.
[12] R. Brühl, A. Ihlenfeld, B. Ittermann, Gradient heating of bulk metallic implants can be a safety concern in MRI, Magn. Reson. Med. 77 (5) (2017) 1739–1740.
[13] L. Winter, E. Oberacker, C. özerdem, Y. Ji, F. Knobelsdorff-Brenkenhoff, G. Weidemann, B. Ittermann, F. Seifert, T. Niendorf, On the RF heating of coronary stents at 7.0 Tesla MRI, Magn. Reson. Med. 74 (4) (2015) 999–1010.
[14] E. Oberacker, K. Paul, T. Huelnhagen, C. Oezerdem, L. Winter, A. Pohlmann, L. Boehmert, O. Stachs, J. Heufelder, A. Weber, M. Rehak, I. Seibel, T. Niendorf, Magnetic resonance safety and compatibility of tantalum markers used in proton beam therapy for intraocular tumors: a 7.0 Tesla study, Magn. Reson. Med. 78 (4) (2017) 1533–1546.
[15] K. Baker, J. Tkach, J. Nyenhuis, M. Phillips, F. Shellock, J. Gonzalez-Martinez, A. Rezai, Evaluation of specific absorption rate as a dosimeter of MRI-related implant heating, J. Magn. Reson. Imag. 20 (2) (2004) 315–320.
[16] L. Winter, B. Silemek, J. Petzold, H. Pfeiffer, W. Hoffmann, F. Seifert, B. Ittermann, Parallel transmission medical implant safety testbed: real-time mitigation of RF induced tip heating using time-domain E-field sensors, Magn. Reson. Med. 84 (6) (2020) 3468–3484.
[17] Y. Eryaman, E. Turk, C. Oto, O. Algin, E. Atalar, Reduction of the radiofrequency heating of metallic devices using a dual-drive birdcage coil, Magn. Reson. Med. 69 (3) (2012) 845–852.
[18] Y. Eryaman, B. Akin, E. Atalar, Reduction of implant RF heating through modification of transmit coil electric field, Magn. Reson. Med. 65 (5) (2011) 1305–1313.
[19] T. Bachschmidt, M. Köhler, J. Nitsler, C. Geppert, P. Jakob, M. Nittka, Polarized multichannel transmit MRI to reduce shading near metal implants, Magn. Reson. Med. 75 (1) (2016) 217–226.
[20] M. Dempsey, B. Condon, D. Handley, Investigation of the factors responsible for burns during MRI, J. Magn. Reson. Imag. 13 (4) (2001) 627–631.
[21] ASTM International, *ASTM F2182-09 Standard Test Method for Measurement of Radio* Frequency Induced Heating Near Passive Implants during Magnetic Resonance Imaging, 2010. West Conshohocken, PA.
[22] I. E. C. (IEC), EC 60601–2-33:2010+AMD1:2013+AMD2:2015, CSV: Medical Electrical Equipment — Particular Requirements for the Basic Safety and Essential Performance of Magnetic Resonance Equipment for Medical Diagnosis, 2015.
[23] I. O. f. S. (ISO), Assessment of the safety of magnetic resonance imaging for patients with an active implantable medical device, Tech Specif ISOTS (2018), 10974.
[24] R. Buchli, P. Boesiger, D. Meier, Heating effects of metallic implants by MRI examinations, Magn. Reson. Med. 7 (3) (1988) 255–261.
[25] H. Bassen, W. Kainz, G. Mendoza, T. Kellom, MRI-induced heating of selected thin wire metallic implants – laboratory and computational studies – findings and new questions raised, Minim Invasive Ther. Allied Technol. 15 (2) (2006).
[26] S. Tsutsui, T. Matsuda, K. Takeda, M. Sasaki, Y. Kubo, K. Setta, S. Fujiwara, K. Chida, K. Ogasawara, Assessment of heating on titanium alloy cerebral aneurysm clips during 7T MRI, Am. J. Neuroradiol. 43 (7) (2022) 972–977.
[27] Y.C.J. Liu, F. Shellock, W. Kainz, Computational and experimental studies of an orthopedic implant: MRI-related heating at 1.5-T/64-MHz and 3-T/128-MHz, J. Magn. Reson. Imag. 37 (2) (2012) 491–497.
[28] P. Serano, L. Angelone, H. Katnani, E. Eskandar, G. Bonmassar, A novel brain stimulation technology provides compatibility with MRI, Sci. Rep. 5 (9805) (2015).
[29] E. Mattei, M. Triventi, G. Calcagnini, F. Censi, W. Kainz, G. Mendoza, H. Bassen, P. Bartolini, Complexity of MRI induced heating on metallic leads: experimental measurements of 374 configurations, Biomed. Eng. Online 7 (11) (2008).
[30] S. Feng, R. Qiang, W. Kainz, J. Chen, A technique to evaluate MRI-induced electric fields at the ends of practical implanted lead, IEEE Trans. Microw. Theor. Tech. 63 (1) (2014) 305–313.
[31] N. Yang, F. Gong, L. Cheng, H. Lei, W. Li, Z. Sun, C. Ni, Z. Wang, Z. Liu, Biodegradable magnesium alloy with eddy thermal effect for effective and accurate magnetic hyperthermia ablation of tumors, Natl. Sci. Rev. 8 (1) (2021).
[32] AZO Materials, Magnesium elektron WE43 alloy (UNS M18430) [Online]. Available: https://www.azom.com/article.aspx?ArticleID=9279, 2013. (Accessed 7 October 2021).
[33] ASTM International, ASTM standard F3268-18a, in: Standard Guide for in Vitro Degradation Testing of Absorbable Metals, 2018. West Conshohocken, PA.
[34] J. Schindelin, I. Arganda-Carreras, E. Frise, V. Kaynig, M. Longair, T. Pietzsch, S. Preibisch, C. Rueden, S. Saalfeld, B. Schmid, J. Tinevez, D. White, V. Hartenstein, K. Eliceiri, P. Tomancak, A. Cardona, Fiji: an open-source platform for biological-image analysis, Nat. Methods 9 (2012) 676–682.
[35] I. Arganda-Carreras, V. Kaynig, C. Rueden, K. Eliceiri, J. Schindelin, A. Cardona, H. Seung, Trainable Weka Segmentation: a machine learning tool for microscopy pixel classification, Bioinformatics 33 (15) (2017) 2424–2426.
[36] N. Schell, A. King, F. Beckmann, T. Fischer, M. Müller, A. Schreyer, The high energy materials science beamline (HEMS) at PETRA III, Mater. Sci. Forum 772 (2013) 57–61.
[37] M. Basham, J. Filik, M. Wharmby, P. Chang, B. El Kassaby, M. Gerring, J. Aishima, K. Levik, B. Pulford, I. Sikharulidze, D. Sneddon, M. Webber, S. Dhesi, F. Maccherozzi, O. Svensson, S. Brockhauser, G. Naray, A. Ashton, Data analysis WorkbeNch (DAWN), J. Synchrotron Radiat. 22 (2015) 853–858.
[38] W. Nitz, A. Oppelt, W. Renz, C. Manke, M. Lenhart, J. Link, On the heating of linear conductive structures as guide wires and catheters in interventional MRI, J. Magn. Reson. Imag. 13 (1) (2001) 105–114.
[39] P. Nordbeck, F. Fidler, I. Weiss, M. Warmuth, M. Friedrich, P. Ehses, W. Geistert, O. Ritter, P. Jakob, M. Ladd, H. Quick, W. Bauer, Spatial distribution of RF-induced E-fields and implant heating in MRI, Magn. Reson. Med. 60 (2) (2008) 312–319.
[40] R. Willumeit-Römer, The interface between degradable Mg and tissue, Characterization of Biodegradable Medical Materials 71 (4) (2019) 1447–1455.

[41] M. Ascencio, M. Pekguleryuz, S. Omanovic, An investigation of the corrosion mechanisms of WE43 Mg alloy in a modified simulated body fluid solution: the influence of immersion time, Corrosion Sci. 87 (2014) 489–503.
[42] G. Galicia, N. Pebere, B. Tribollet, V. Vivier, Local and global electrochemical impedances applied to the corrosion behaviour of an AZ91 magnesium alloy, Corrosion Sci. 51 (8) (2009) 1789–1794.
[43] N. Mcintyre, C. Chen, Role of impurities on Mg surfaces under ambient exposure conditions, Corrosion Sci. 40 (10) (1998) 1697–1709.
[44] I. Marco, F. Feyerabend, R. Willumeit-Römer, O. Van der Biest, Degradation testing of Mg alloys in Dulbecco's modified eagle medium: influence of medium sterilization, Mater. Sci. Eng. C 62 (2016) 68–78.
[45] B. Zeller-Plumhoff, D. Laipple, H. Slominksa, K. Iskhakova, E. Longo, A. Hermann, S. Flenner, I. Greving, M. Storm, R. Willumeit-Römer, Evaluating the morphology of the degradation layer of pure magnesium via 3D imaging at resolutions below 40 nm, Bioact. Mater. 6 (12) (2021) 4368–4376.
[46] A. Hänzi, P. Gunde, M. Schinhammer, P. Uggowitzer, On the biodegradation performance of an Mg–Y–RE alloy with various surface conditions in simulated body fluid, Acta Biomater. 5 (1) (2009) 162–171.
[47] E. Öcal, Z. Esen, K. Aydinol, A. Dericioglu, Comparison of the short and long-term degradation behaviors of as-cast pure Mg, AZ91 and WE43 alloys, Mater. Chem. Phys. 241 (2020).
[48] D. Liu, Y. Ding, T. Guo, X. Qin, C. Guo, S. Yu, S. Lin, Influence of fine-grain and solid-solution strengthening on mechanical properties and in vitro degradation of WE43 alloy, Biomed. Mater. 9 (2014).
[49] A. Anesi, M. Di Bartolomeo, A. Pellacani, M. Feretti, F. Cavani, R. Salvatori, R. Nocini, C. Palumbo, L. Chiarini, Bone healing evaluation following different osteotomic techniques in animal models: a suitable method for clinical insights, Appl. Sci. 10 (20) (2020) 7165.
[50] MatWeb, LLC, MatWeb: Material Property Data, 1996. -2022. [Online]. Available: https://www.matweb.com/index.aspx. (Accessed 14 July 2022).
[51] M. Capek, J. Eichler, P. Hazdra, Evaluating radiation efficiency from characteristic currents, IET Microw., Antennas Propag. 9 (1) (2015) 10–15.
[52] C. Armenean, E. Perrin, M. Armenean, O. Beuf, F. Pilleul, H. Saint-Jalmes, RF-induced temperature elevation along metallic wires in clinical magnetic resonance imaging: influence of diameter and length, Magn. Reson. Med. 52 (5) (2004) 1200–1206.
[53] S. Seshadri, J. Scott, Enhancing skin-effect using surface roughening and its potential to reduce RF heating from implant leads, in: Electronics New Zealand Conference, 2017.
[54] G. Gold, K. Helmreich, A physical model for skin effect in rough surfaces, in: 7th European Microwave Integrated Circuit Conference, 2012.
[55] A. Horn, J. Reynolds, J. Rautio, Conductor profile effects on the propagation constant of microstrip transmission lines, in: IEEE MTT-S International Microwave Symposium, 2010.
[56] D. Gensler, F. Fidler, P. Ehses, M. Warmuth, R. Reiter, M. Düring, O. Ritter, M. Ladd, H. Quick, P. Jakob, W. Bauer, P. Nordbeck, MR safety: fast T 1 thermometry of the RF-induced heating of medical devices, Magn. Reson. Med. 68 (5) (2012) 1593–1599.
[57] A. Yao, M. Murbach, T. Goren, E. Zastrow, W. Kainz, N. Kuster, Induced radiofrequency fields in patients undergoing MR examinations: insights for risk assessment, Phys. Med. Biol. 66 (2021).
[58] P. Sekar, N. S, V. Desai, Recent progress in in vivo studies and clinical applications of magnesium based biodegradable implants – a review, Journal of Magnesium and Alloys 9 (4) (2021) 1147–1163.

Chapter 9

Discussion

While the research conducted in this dissertation has contributed valuable insights to the field, it is essential to acknowledge its inherent limitations, which present opportunities for future investigations to enhance our understanding. In Chapter 6, it was challenging to conduct in-depth statistical analyses comparing the two materials due to the limited number of animals and bone samples available for study. To provide a more robust and comprehensive assessment, future research should consider expanding the sample size and including a broader range of time points for evaluation. Additionally, a thorough investigation into the surface morphology of the coating would offer a deeper understanding of how PEO-coated WE43 implants influence the lacuno-canalicular network (LCN).

Chapters 7 and 8 of this dissertation utilised *in vitro* methods to induce degradation of the WE43 implants before conducting measurements. While these approaches are informative, it is crucial to acknowledge that *in vitro* degradation mechanisms may not entirely replicate the complex interactions that occur *in vivo*. To address this limitation, future studies should explore alternative sample preparation methods that more accurately simulate *in vivo* degradation conditions. This would contribute to a more comprehensive understanding of the behaviour of these implants within the physiological context. By addressing these limitations and conducting further investigations, the research community can advance our knowledge of implant materials and their impact on bone tissue, ultimately leading to improved clinical outcomes and patient care.

9.1 Outlook

The push for deep learning methodologies has witnessed remarkable growth, challenging conventional image processing techniques across various domains [163, 164, 165]. In the context of TXM imaging analysis, the imperative task of segmentation is required to discern structures within raw images, primarily contingent upon variations in intensity levels. Notably, achieving precise segmentation of voluminous 3D data sets has emerged as a significant challenge. Although conventional segmentation methods are at our disposal, the imperative to refine and enhance automated segmentation techniques persists, driven by the dual objectives of augmenting user convenience and expediting processing time.

In the investigation of the LCN within Chapter 6, a pragmatic approach combining thresholding and manual correction was deployed, adequately fulfilling the

requirements of that particular study. However, ongoing efforts have been dedicated to the refinement of this segmentation methodology through the development of algorithms rooted in machine learning principles. A pertinent illustration of such progress was introduced in the work of Baltruschat *et al.* in 2021, wherein they introduced an automated segmentation framework tailored for the analysis of large volumetric data sets. This framework harnessed the adaptability of neural networks, showcasing superior performance in contrast to semi-automatic segmentation techniques [166]. While this example pertains specifically to the realm of Mg-based implants, the principles and methodologies it embodies hold promise for adaptation and application in contexts akin to those explored in Chapter 6. Consequently, the integration of advanced segmentation methods bears the potential to significantly enhance the efficiency and efficacy of LCN segmentation surrounding biodegradable materials, advancing our capabilities in this critical domain of research.

Furthermore, the realm of structural modelling and simulations opens up new opportunities for conducting functional analyses of the LCN. Following the segmentation of the LCN in Chapter 6, there was a comprehensive endeavour to measure and compute various physical parameters aimed at characterising the LCN surrounding both PEO-coated and uncoated materials. While the discussion primarily centred around transport efficiency as a descriptor of LCN functionality, it is crucial to recognise that the potential for exploring additional parameters remains untapped, offering opportunities for further investigation through computational modelling. In particular, the domain of fluid flow efficiency within the LCN can be investigated by harnessing image-based finite element modelling techniques. Previous applications of finite element analysis have demonstrated their capability to determine critical parameters such as interstitial fluid velocity and pressure distribution within the canaliculi [167]. Hence, in the pursuit of comprehensive insights, future inquiries should contemplate the combination of TXM alongside complementary imaging modalities and integrating fluid flow modelling methodologies. This approach aids in the understanding of how Mg-based implants exert their influence on the intricate architecture of the LCN within bone, potentially uncovering crucial insights with implications for bone health and medical implant design.

Moreover, computational methods and modelling can significantly accelerate and streamline the assessment of the safety of biodegradable Mg-based orthopaedic implants. By employing finite element analysis (FEA) and computational fluid dynamics (CFD) simulations, researchers can predict the implant's degradation rate, mechanical stability, and potential interactions with the patient's body, such as corrosion effects and tissue responses, without the need for extensive and costly *in vivo* or *in vitro* experiments. These simulations can be calibrated and validated using available experimental data and then fine-tuned iteratively. Additionally, machine learning algorithms can help analyse large data sets and identify critical factors affecting implant safety. Overall, leveraging computational tools and models in this manner can expedite the evaluation process, reduce testing expenses, and enhance the understanding of the implant's safety profile, ultimately accelerating its approval for clinical use.

Chapter 10

Conclusion

This research has made significant strides in the field of biodegradable orthopaedic implants, particularly those made of Mg. This work leverages novel imaging techniques to explore Mg-based implants, addressing critical questions related to their behaviour, safety, and impact on bone. From the results of this cumulative work, the following conclusions can be drawn in response to the objectives presented in Chapter 2:

The impact of a biodegradable substance on the LCN was explored using non-invasive 3D imaging for the very first time. In Chapter 6, we concluded that PEO-coated WE43 implants may induce smoother ellipsoidal lacunar shapes near the implant surface. In contrast, uncoated WE43 implants may elicit higher LCN inter-connectivity. Lower degradation rates caused by the PEO coating were shown to promote rounder lacunar shapes which have demonstrated to be more resistant to damage. On the other hand, greater canalicular presence was noticed near the uncoated material which may suggest that material which degrades at higher rates may elicit a more effective connected LCN, better prepared for canalicular interruption. Moreover, the innovative imaging methodology employed here holds the promise of advancing our understanding of the intricate relationship between the LCN and biodegradable materials. Such relationships could have significant implications for the design and development of implants with improved biocompatibility and degradation, ultimately benefiting patients in need of such medical devices.

For the first instance, the artefact behaviour of Mg-based implants has been quantitatively assessed. In Chapter 7, we identified that metallic artefact production during MRI caused by WE43 implants reduces with degradation time. The total artefact volume caused by WE43 implants lessened as corrosion of the implants persisted. The worst-case scenario for viewing the implant and surrounding area with MRI may be directly after initial implantation. WE43 implants produced lower metallic artefact when compared to commercially available titanium equivalents. This conclusion has significant real-life implications as it supports the consideration of Mg-based materials as viable options for medical implants, potentially reducing image distortions and improving the assessment of bone healing through MRI. Reduced artefacts and clearer imaging directly benefits patient assessment and follow-up.

In a crucial endeavour, patient safety considerations were explored associated with the transition of Mg-based implants from the realm of research to clinical application. In Chapter 8, we observed that RF-induced heating of WE43 implants during MRI lessens as degradation continues. The disruption of the "skin effect"

caused by the formation of the degradation layer may hinder an expected increase in implant heating. The highest heating safety risk occurs for non-degraded (newly implanted) samples. Overall, no greater safety risks are introduced when compared to titanium implant materials. By demonstrating that the heating profile of these screws decreases with degradation time, the research provides valuable insights for clinicians and MRI technicians. This information can aid in the development of more informed and vigilant imaging schedules for post-operative patient care, ultimately enhancing patient safety and the quality of clinical follow-up for individuals with such implants.

In conclusion, this research represents remarkable scientific achievements in its innovative methodologies and its pioneering exploration of Mg-based implants. This dissertation sheds light on the imaging of Mg-based implants and their effects on the surrounding environment, offering valuable insights into the morphological alterations of bone, visibility during MRI, and patient safety considerations in the clinical application of these implants. These findings largely contribute to the understanding of Mg-based implant behaviour which guides future research and development in the field, ultimately benefiting patients in need of orthopaedic implants.

Bibliography

[1] N. Walter, T. Stich, D. Docheva, V. Alt, and M. Rupp, "Evolution of implants and advancements for osseointegration: A narrative review," *Injury*, vol. 53, pp. S69–S73, 2022. New Technologies in Orthopaedic Traumatology.

[2] J. Wang, J. Xu, C. Hopkins, D. H. K. Chow, and L. Qin, "Biodegradable magnesium-based implants in orthopedics—a general review and perspectives," *Advanced Science*, 2020.

[3] P. Augat and C. von Rüden, "Evolution of fracture treatment with bone plates," *Injury*, vol. 49, pp. S2–S7, 2018. Plating of Fractures: current treatments and complications.

[4] Y. Xie, L. Cai, Z. Deng, B. Ran, and C. Hu, "Absorbable screws versus metallic screws for distal tibiofibular syndesmosis injuries: A meta-analysis," *The Journal of Foot and Ankle Surgery*, vol. 54, no. 4, pp. 663–670, 2015.

[5] A. Poliakov, V. Pakhaliuk, and V. L. Popov, "Current trends in improving of artificial joints design and technologies for their arthroplasty," *Frontiers in Mechanical Engineering*, vol. 6, p. 4, 2020.

[6] S. S. Pillai, "Current status and future prospects of spinal implants.," *Trends in Biomaterials & Artificial Organs*, vol. 35, no. 5, 2021.

[7] M. Nasr Azadani, A. Zahedi, O. K. Bowoto, and B. I. Oladapo, "A review of current challenges and prospects of magnesium and its alloy for bone implant applications," *Progress in Biomaterials*, vol. 11, no. 1, pp. 1–26, 2022.

[8] H. Waizy, J.-M. Seitz, J. Reifenrath, A. Weizbauer, F.-W. Bach, A. Meyer-Lindenberg, B. Denkena, and H. Windhagen, "Biodegradable magnesium implants for orthopedic applications," *Journal of Materials Science*, vol. 48, pp. 39–50, 2013.

[9] D. F. Williams, *The Williams Dictionary of Biomaterials*. Liverpool: Liverpool University Press, 1999.

[10] M. Vert, Y. Doi, K. Hellwich, M. Heß, P. Hodge, P. Kubisa, M. Rinaudo, and F. Schué, "Terminology for biorelated polymers and applications (iupac recommendations 2012)," *Pure and Applied Chemistry*, 2012.

[11] T. Velnar, G. Bunc, R. Klobucar, and L. Gradišnik, "Biomaterials and host versus graft response: A short review," *Bosnian Journal of Basic Medical Sciences*, 2016.

[12] C. E. Heim, D. Vidlak, T. D. Scherr, J. A. Kozel, M. S. Holzapfel, D. Muirhead, and T. Kielian, "Myeloid-derived suppressor cells contribute to staphylococcus aureus orthopedic biofilm infection," *The Journal of Immunology*, 2014.

[13] J. M. Anderson, A. Rodriguez, and D. T. Chang, "Foreign body reaction to biomaterials," *Seminars in Immunology*, 2008.

[14] V. Wadhawa, C. Doshi, M. Hinduja, P. Garg, K. Patel, A. Mishra, and P. Shah, "Anterior minithoracotomy: A safe approach for surgical asd closure & asd device retrieval," *Brazilian Journal of Cardiovascular Surgery*, 2017.

[15] A. Sicilia, S. Cuesta, G. Coma, I. Arregui, C. Guisasola, E. M. Ruiz, and A. Maestro, "Titanium allergy in dental implant patients: A clinical study on 1500 consecutive patients," *Clinical Oral Implants Research*, 2008.

[16] K. Sadiq, M. Stack, and R. A. Black, "Wear mapping of cocrmo alloy in simulated bio-tribocorrosion conditions of a hip prosthesis bearing in calf serum solution," *Materials Science and Engineering C*, 2015.

[17] Y. Okazaki, "Comparison of fatigue properties and fatigue crack growth rates of various implantable metals," *Materials*, 2012.

[18] K. Hopkins, K. Buno, N. Romick, A. C. Santos, S. L. Tinsley, E. Wakelin, J. Kennedy, M. R. Ladisch, B. L. Allen-Petersen, and L. Solorio, "Sustained degradation of hyaluronic acid using an in situ forming implant," *Pnas Nexus*, 2022.

[19] R. Ohri, S. K. Hahn, A. S. Hoffman, P. S. Stayton, and C. M. Giachelli, "Hyaluronic acid grafting mitigates calcification of glutaraldehyde-fixed bovine pericardium," *Journal of Biomedical Materials Research Part A*, 2004.

[20] N. Eliaz, "Corrosion of metallic biomaterials: A review," *Materials*, 2019.

[21] M. Jäger, C. Zilkens, K. Zanger, and R. Krauspe, "Significance of nano- and microtopography for cell-surface interactions in orthopaedic implants," *Journal of Biomedicine and Biotechnology*, 2007.

[22] W. F. Agnew and D. B. McCreery, "Considerations for safety with chronically implanted nerve electrodes," *Epilepsia*, 1990.

[23] Y. C. Wong, W. Chau, K. O. Kwok, and S. W. Law, "Incidence and risk factors for implant failure in spinal metastasis surgery," *Asian Spine Journal*, 2020.

[24] S. A. Seyedkhani and R. Mohammadpour, *Biocomposites*. IntechOpen, 2023.

[25] L. D. Marestoni, H. d. S. Barud, R. J. Gomes, R. P. F. Catarino, N. N. Y. Hata, J. B. Ressutte, and W. A. Spinosa, "Commercial and potential applications of bacterial cellulose in brazil: Ten years review," *Polímeros*, 2020.

[26] S. Yin, W. Zhang, Y. Tang, G. Yang, X. Wu, S. Lin, X. Liu, H. Cao, and X. Jiang, "Preservation of alveolar ridge height through mechanical memory: A novel dental implant design," *Bioactive Materials*, 2021.

[27] B. Cheruvu, I. Venkatarayappa, and T. Goswami, "Stress shielding in cemented hip implants assessed from computed tomography," *Biomedical Journal of Scientific & Technical Research*, 2019.

[28] S. Oikonomidis, L. Altenrath, L. Westermann, J. Bredow, P. Eysel, and M. J. Scheyerer, "Implant-associated infection of long-segment spinal instrumentation: A retrospective analysis of 46 consecutive patients," *Asian Spine Journal*, 2021.

[29] M. El-Omar, G. Dangas, I. Iakovou, and R. Mehran, "Update on in-stent restenosis," *Current Interventional Cardiology Reports*, vol. 4, pp. 296–305, 2001.

[30] J. Sheen and V. Garla, *StatPearls [Internet].* Treasure Island, Florida: StatPearls Publishing, 2021.

[31] M. I. Rahim, S. Ullah, and P. P. Mueller, "Advances and challenges of biodegradable implant materials with a focus on magnesium-alloys and bacterial infections," *Metals*, 2018.

[32] K. Ceonzo, A. Gaynor, L. Shaffer, K. Kojima, C. Vacanti, and G. Stahl, "Polyglycolic acid-induced inflammation: Role of hydrolysis and resulting complement activation," *Tissue Engineering*, vol. 12, pp. 301–308, 2006.

[33] Y. Zhao, J. Feng, H. Yu, W. Lin, X. Li, Y. Tian, and M. Zhao, "Comparative study on biodegradation of pure iron prepared by microwave sintering and laser melting," *Materials*, vol. 15, 2022.

[34] G. Gasior, J. Szczepański, and A. Radtke, "Biodegradable iron-based materials—what was done and what more can be done?," *Materials*, vol. 14, no. 12, 2021.

[35] D. Pierson, J. Edick, A. Tauscher, E. Pokorney, P. Bowen, J. Gelbaugh, J. Stinson, H. Getty, C. Lee, J. Drelich, and J. Goldman, "A simplified in vivo approach for evaluating the bioabsorbable behavior of candidate stent materials," *Journal of Biomedical Materials Research*, vol. 100B, pp. 58–67, 2011.

[36] D. Vojtech, J. Kubasek, J. Serak, and P. Novak, "Mechanical and corrosion properties of newly developed biodegradable zn-based alloys for bone fixation," *Acta Biomaterialia*, vol. 7, pp. 3515–3522, 2011.

[37] I. of Medicine: Food and N. Board, *Dietary Reference Intakes: Calcium, Phosphorus, Magnesium, Vitamin D and Fluoride.* Washington, DC: National Academy Press, 1997.

[38] R. Rude, *Magnesium*, pp. 527–537. New York, NY: CRC Press, 2010.

[39] R. Rude, *Magnesium*, pp. 159–175. Baltimore, USA: Wolters Kluwer Health Adis, 2012.

[40] S. Volpe, *Magnesium*, pp. 459–474. Ames, USA: John Wiley & Sons, 2012.

[41] R. Elin, "Assessment of magnesium status for diagnosis and therapy," *Magnesium Research*, vol. 23, pp. S194–198, 2010.

[42] E. Huse, "A new ligature?," *Chicago Med J Exam*, pp. 172–2, 1878.

[43] F. Witte, "The history of biodegradable magnesium implants: A review," *Acta Biomaterialia*, vol. 6, pp. 1680–1692, 2010.

[44] A. Lambotte, "Technique et indications de la prothèse perdue dans la traitement des fractures," *Presse Med Belge*, vol. 17, pp. 321–323, 1909.

[45] E. Abed and R. Moreau, "Importance of melastatin-like transient receptor potential 7 and magnesium in the stimulation of osteoblast proliferation and migration by platelet-derived growth factor," *American Journal of Physiology: Cell Physiology*, vol. 297, pp. C360–C368, 2009.

[46] Z. Zhang, J. Xu, Y. Ruan, and e. al., "Implant-derived magnesium induces local neuronal production of cgrp to improve bone-fracture healing in rats," *Nature Medicine*, vol. 22, pp. 1160–1169, 2016.

[47] C. Yang, G. Yuan, J. Zhang, Z. Tang, X. Zhang, and K. Dai, "Effects of magnesium alloys extracts on adult human bone marrow-derived stromal cell viability and osteogenic differentiation," *Biomedical Materials*, vol. 5, 2010.

[48] R. Radha and D. Sreekanth, "Insight of magnesium alloys and composites for orthopedic implant applications–a review," *Jounral of magnesium and alloys*, vol. 5, pp. 286–312, 2017.

[49] I. Johnson and H. Liu, "A study on factors affecting the degradation of magnesium and a magnesium-yttrium alloy for biomedical applications," *Plos One*, 2013.

[50] H. R. Bakhsheshi-Rad, E. Hamzah, W. S. Ying, M. Razzaghi, S. Sharif, A. F. Ismail, and F. Berto, "Improved bacteriostatic and anticorrosion effects of polycaprolactone/chitosan coated magnesium via incorporation of zinc oxide," *Materials*, 2021.

[51] H. S. Brar, M. O. Platt, M. Sarntinoranont, P. I. Martin, and M. V. Manuel, "Magnesium as a biodegradable and bioabsorbable material for medical implants," *Jom*, 2009.

[52] P. Tian and X. Liu, "Surface modification of biodegradable magnesium and its alloys for biomedical applications," *Regenerative Biomaterials*, vol. 2, pp. 135–151, 11 2014.

[53] D. Zhao, F. Witte, F. Lu, J. Wang, J. Li, and L. Qin, "Current status on clinical applications of magnesium-based orthopaedic implants: a review from clinical translational perspective," *Biomaterials*, vol. 112, pp. 287–302, 2017.

[54] G. Song and A. Atrens, "Recent insights into the mechanism of magnesium corrosion and research suggestions," *Advanced Engineering MAterials*, vol. 9, pp. 177–183, 2007.

[55] G. Song and A. Atrens, "Understanding magnesium corrosion—a framework for improved alloy performance," *Advanced Engineering Materials*, vol. 5, pp. 837–858, 2003.

[56] J. Hanawalt, C. Nelson, and J. Peloubet, "Corrosion studeios of magnesium and its alloys," *The American Institute of Mining, Metallurgical, and Petroleum Engineers*, p. 26, 1941.

[57] A. Atrens, M. Liu, A. Zainal, and N. Ishida, "Corrosion mechanism applicable to biodegradable magnesium implants," *2nd Symposium on Biodegradable Metals*, vol. 176, pp. 1609–1636, 2011.

[58] N. Mcintyre and C. Chen, "Role of impurities on mg surfaces under ambient exposure conditions," *Corrosion Science*, vol. 40, pp. 1697–1709, 1998.

[59] C. Fotea, J. Callaway, and M. Alexander, "Characterisation of the surface chemistry of magnesium exposed to the ambient atmosphere," *Surface and Interface Analysis*, vol. 38, pp. 1363–1371, 2006.

[60] J. Nordlien, S. Ono, N. Masuko, and K. Nisancioglu, "A tem investigation of naturally formed oxide films on pure magnesium," *Corrosion Science*, vol. 39, pp. 1397–1414, 1997.

[61] E. Ghali, W. Dietzel, and K. Kainer, "General and localized corrosion of magnesium alloys: A critical review," *Journal of Materials Engineering and Performance*, vol. 13, pp. 7–23, 2004.

[62] L. Fairman and J. West, "Stress corrosion crackinng of a magnesium aluminium alloy," *Corrosion Science*, vol. 5, pp. 711–716, 1965.

[63] P. Schmutz, V. Guillaumin, J. Lillard, and G. Frankel, "Influence of dichromate ions on corrosion processes on pure magnesium," *Journal of The Electrochemical Society*, vol. 150, 2003.

[64] F. Witte, N. Horn, C. Vogt, S. Cohen, K. Kainer, R. Willumeit, and F. Feyerabend, "Degradable biomaterials based on magnesium," *Current Opinion in Solid State and Materials Science*, vol. 12, pp. 63–72, 2008.

[65] G. Song, "Control of biodegradation of biocompatible magnesium alloys," *Corrosion Science*, vol. 49, pp. 1696–1701, 2007.

[66] J. Zhang, N. Kong, Y. Shi, J. Niu, L. Mao, H. Li, M. Xiong, and G. Yuan, "Influence of proteins and cells on in vitro corrosion of mg-nd-zn-zr alloy," *Corrosion Science*, vol. 85, pp. 477–481, 2014.

[67] M. Bornapour, M. Celikin, and M. Pekguleryuz, "Thermal exposure effects on the in vitro degradation and mechanical properties of mg-sr and mg-ca-sr biodegradable implant alloys and the role of the microstructure," *Material Science and Engineering: C*, vol. 46, pp. 16–24, 2015.

[68] A. Atrens and W. Dietzel, "The negative difference effect and unipostive mg+," *Journal of Advanced Engineering Materials*, vol. 9, pp. 292–297, 2007.

[69] N. Kirkland, N. Birbilis, and M. Staiger, "Assessing the corrosion of biodegradable magnesium implants: A critical review of current methodologies and their limitations," *Acta Biomaterialia*, vol. 8, pp. 925–936, 2012.

[70] J. Chen, J. Dai, J. Qian, W. Li, R. Li, D. Pang, G. Wan, P. Li, and S. Xu, "Influence of surface roughness on biodegradability and cytocompatibility of high-purity magnesium," *Materials*, vol. 15, no. 11, 2022.

[71] B. Ullmann, J. Reifenrath, J.-M. Seitz, D. Bormann, and A. Meyer-Lindenberg, "Influence of the grain size on the in vivo degradation behaviour of the magnesium alloy lae442," *Proceedings of the Institution of Mechanical Engineers, Part H: Journal of Engineering in Medicine*, vol. 227, no. 3, pp. 317–326, 2013. PMID: 23662348.

[72] X. Li, Y. Wang, C. Chu, L. Han, J. Bai, and F. Xue, "A study on mg wires/polylactic acid composite degradation under dynamic compression and bending load for implant applications," *Journal of the Mechanical Behavior of Biomedical Materials*, vol. 105, p. 103707, 2020.

[73] M. Bobby Kannan and R. K. R. Singh, "A mechanistic study of in vitro degradation of magnesium alloy using electrochemical techniques," *Journal of Biomedical Materials Research Part A*, vol. 93A, no. 3, pp. 1050–1055, 2010.

[74] C. Ning, L. Zhou, Y. Zhu, Y. Li, P. Yu, S. Wang, T. He, W. Li, G. Tan, Y. Wang, and C. Mao, "Influence of surrounding cations on the surface degradation of magnesium alloy implants under a compressive pressure," *Langmuir*, vol. 31, no. 50, pp. 13561–13570, 2015.

[75] E. L. Silva, S. V. Lamaka, D. Mei, and M. L. Zheludkevich, "The reduction of dissolved oxygen during magnesium corrosion," *ChemistryOpen*, vol. 7, no. 8, pp. 664–668, 2018.

[76] X. Guo, Y. Song, S. Sang, and Y. Qiao, "Study on fretting wear properties of medical mg-2.0zn-1.6ca alloy," *Journal of Physics Conference Series*, 2022.

[77] M. Niinomi, Y. Liu, M. Nakai, H. Liu, and H. Li, "Biomedical titanium alloys with young's moduli close to that of cortical bone," *Regenerative Biomaterials*, 2016.

[78] B. H. B. Kuffner, P. Capellato, L. M. S. Ribeiro, D. Sachs, and G. Silva, "Production and characterization of a 316l stainless steel/ beta-tcp biocomposite using the functionally graded materials (fgms) technique for dental and orthopedic applications," *Metals*, 2021.

[79] A. M. Alsebaie, "Characterisation of alumina-zirconia composites produced by micron-sized powders," in *Materials Science, Engineering*, 2006.

[80] I. El Mahallawi, A. Shash, and A. Amer, "Nanoreinforced cast al-si alloys with al2o3, tio2 and zro2 nanoparticles," *Journal of Metals*, vol. 2015, pp. 802–821, 05 2015.

[81] L.-N. Zhang, Z.-T. Hou, X. Ye, Z.-B. Xu, X.-L. Bai, and P. Shang, "The effect of selected alloying element additions on properties of mg-based alloy as bioimplants: A literature review," *Frontiers of Materials Science*, vol. 7, 09 2013.

[82] B. Luthringer-Feyerabend, F. Feyerabend, and R. Willumeit, "Magnesium-based implants: A mini-review," *Magnesium research : official organ of the International Society for the Development of Research on Magnesium*, vol. 27, pp. 142–54, 11 2014.

[83] S. Fukumoto, K. Sugahara, A. Yamamoto, and H. Tsubakino, "Improvement of corrosion resistance and adhesion of coating layer for magnesium alloy coated with high purity magnesium," *Materials Transactions*, 2003.

[84] K. R and P. Katyal, "Effects of alloying elements on performance of biodegradable magnesium alloy," *Materials Today: Proceedings*, vol. 56, pp. 2443–2450, 2022.

[85] F. Witte, N. Hort, C. Vogt, S. Cohen, K. Kainer, R. Willumeit, and F. Feyerabend, "Degradable biomaterials based on magnesium corrosion," *Current opinion in solid state and materials science*, vol. 12, pp. 63–72, 2008.

[86] G. Song and A. Atrens, "Corrosion mechanisms of magnesium alloys," *Advanced Engineering Materials*, vol. 1, pp. 11–33, 1999.

[87] M. Mokhtarishirazabad, M. Azadi, G. Farrahi, G. Wingert, and W. Eichlseder, "Improvement of high temperature fatigue lifetime in az91 magnesium alloy by heat treatment," *Materials Science and Engineering: A*, vol. 588, pp. 357–365, 2013.

[88] A. Mouritz, *Introduction to Aerospace Materials*. Elsevier, 2012.

[89] L. Calado, M. Carmezim, and M. Montemor, "Rare earth based magnesium alloys—a review on we series," *Frontiers in Materials: Structural Materials*, 2022.

[90] E. Ocal, Z. Esen, K. Aydinol, and A. Dericioglu, "Comparison of the short and long-term degradation behaviors of as-cast pure mg, az91 and we43 alloys," *Materials Chemistry and Physics*, vol. 241, 2020.

[91] C. Liu, J. Jiang, M. Wang, Y. Wang, P. Chu, and W. Huang, "In vitro degradation and biocompatibility of we43, zk60, and az91 biodegradable magnesium alloys," *Advanced Materials Research*, vol. 287, pp. 2008–2014, 2011.

[92] L. Long, M. Zhang, Y. Li, J. Zhao, L. Qin, and Y. Lai, "Corrosion and biocompatibility improvement of magnesium-based alloys as bone implant materials: a review," *Regenerative Biomaterials*, vol. 4, pp. 129–137, 2017.

[93] P. Ferreira, K. Piai, A. Takayanagui, and S. Segura-Munoz, "Aluminum as a risk factor for alzheimer's disease," *Revista Latino-Americana de Enfermagem*, vol. 16, pp. 151–157, 2008.

[94] S. Harandi, M. Mirshahi, S. Koleini, M. Idris, H. Jafari, and M. Kadir, "Effect of calcium content on the microstructure, hardness and in-vitro corrosion behavior of biodegradable mg-ca binary alloy," *Materials Research*, vol. 16, pp. 11–18, 2013.

[95] S. Song, G. Song, W. Shen, and M. Liu, "Corrosion and electrochemical evaluation of coated magnesium alloys," *Corrosion*, vol. 68, 2012.

[96] D. Ding, J. Roth, and R. Salvi, "Manganese is toxic to spiral ganglion neurons and hair cells in vitro," *Neurotoxicology*, vol. 32, pp. 233–241, 2011.

[97] Y. Ding, C. Wen, P. Hodgson, and Y. Li, "Effects of alloying elements on the corrosion behavior and biocompatibility of biodegradable magnesium alloys: a review," *Journal of Materials Chemistry B*, vol. 2, pp. 1912–1933, 2014.

[98] J. Chang, X. Guo, S. He, P. Fu, L. Peng, and W. Ding, "Investigation of the corrosion for mg–xgd–3y–0.4 zr (x= 6, 8, 10, 12 wt%) alloys in a peak-aged condition," *Corrosion Science*, vol. 50, pp. 166–177, 2008.

[99] K. Munir, J. Lin, C. Wen, P. Wright, and Y. Li, "Mechanical, corrosion, and biocompatibility properties of mg-zr-sr-sc alloys for biodegradable implant applications," *Acta Biomaterialia*, vol. 102, pp. 493–507, 2020.

[100] X. Zhang, K. Zhang, X. Deng, L. Hongwei, L. Yongjun, M. Minglong, L. Ning, and Y. Wang, "Corrosion behavior of mg–y alloy in nacl aqueous solution," *Progress in Natural Science: Materials International*, vol. 22, pp. 169–174, 2012.

[101] A. Loos, R. Rohde, A. Haverich, and S. Barlach, "In vitro and in vivo biocompatibility testing of absorbable metal stents," *Macromolecular Symposia*, vol. 253, pp. 103–108, 2007.

[102] Y. He, H. Tao, Y. Zhang, Y. Jiang, S. Zhang, C. Zhao, J. Li, B. Zhang, Y. Song, and X. Zhang, "Biocompatibility of bio-mg-zn alloy within bone with heart, liver, kidney and spleen.," *Chinese Science Bulletin*, vol. 54, pp. 484–491, 2009.

[103] Y. Li, C. Wen, D. Mushahary, R. Sravanthi, N. Harishankar, G. Pande, and P. Hodgson, "Mg–zr–sr alloys as biodegradable implant materials," *Acta Biomaterialia*, vol. 8, pp. 3177–3188, 2012.

[104] Z. Huan, M. Leeflang, J. Zhou, L. Fratila-Apachitei, and J. Duszczyk, "In vitro degradation behavior and cytocompatibility of mg–zn–zr alloys," *Journal of Material Science: Materials in Medicine*, vol. 21, pp. 2623–2635, 2010.

[105] D. Noviana, D. Paramitha, M. F. Ulum, and H. Hermawan, "The effect of hydrogen gas evolution of magnesium implant on the postimplantation mortality of rats," *Journal of Orthopaedic Translation*, vol. 5, pp. 9–15, 2016. Special Issue: Orthopaedic Biomaterials and Devices.

[106] S. A. Salman, K. Kuroda, and M. Okido, "Preparation and characterization of hydroxyapatite coating on az31 mg alloy for implant applications," *Bioinorganic Chemistry and Applications*, 2013.

[107] P. Wang, J. Liu, S. Shu, Q. Li, P. Xiong, S. Gao, J. Yan, Y. Cheng, and T. Xi, "In vitro and in vivo studies on two-step alkali-fluoride-treated mg–zn–y–nd alloy for vascular stent application: Enhancement in corrosion resistance and biocompatibility," *Acs Biomaterials Science & Engineering*, 2019.

[108] M. Horynová, M. Remešová, L. Klakurková, K. Dvořák, I. Ročňáková, S. Yan, L. Čelko, and G. Song, "Design of tailored biodegradable implants: The effect of voltage on electrodeposited calcium phosphate coatings on pure magnesium," *Journal of the American Ceramic Society*, 2018.

[109] F. Simchen, M. Sieber, A. Kopp, and T. Lampke, "Introduction to plasma electrolytic oxidation—an overview of the process and applications," *Coatings*, vol. 10, no. 7, 2020.

[110] X. Zhang, Z. Zhao, F. Wu, Y. Wang, and J. Wu, "Corrosion and wear resistance of az91d magnesium alloy with and without microarc oxidation coating in hank's solution," *Journal of Materials Science*, vol. 42, pp. 8523–8528, 2007.

[111] X. Gu, N. Li, W. Zhou, Y. Zheng, X. Zhao, Q. Cai, and L. Ruan, "Corrosion resistance and surface biocompatibility of a microarc oxidation coating on a mg–ca alloy," *Acta Biomaterialia*, vol. 7, pp. 1880–1889, 2011.

[112] L. Zhao, C. Cui, Q. Wang, and S. Bu, "Growth characteristics and corrosion resistance of micro-arc oxidation coating on pure magnesium for biomedical applications," *Corrosion Science*, vol. 52, pp. 2228–2234, 2010.

[113] R. Arrabal, E. Matykina, P. Skeldon, G. Thompson, and A. Pardo, "Transport of species during plasma electrolytic oxidation of we43-t6 magnesium alloy," *Journal of The Electrochemical Society*, vol. 155, 2008.

[114] B. Schaller, N. Saulacic, T. Imwinkelried, S. Beck, E. Liu, J. Gralla, K. Nakahara, W. Hofstetter, and T. Iizuka, "In vivo degradation of magnesium plate/screw osteosynthesis implant systems: Soft and hard tissue response in a calvarial model in miniature pigs," *Journal of Cranio-Maxillofacial Surgery*, vol. 44, pp. 309–317, 2016.

[115] P. Harjen, N. Wegner, P. Ahmadi, L. Matthies, O. Nada, S. Fuest, M. Yan, C. Knipfer, M. Gosau, F. Walther, and R. Smeets, "Toward tailoring the degradation rate of magnesium-based biomaterials for various medical applications: Assessing corrosion, cytocompatibility and immunological effects," *International Journal of Molecular Sciences*, vol. 22, p. 971, 2021.

[116] C. Rendenbach, H. Fischer, A. Kopp, K. Schmidt-Bleek, H. Kreiker, S. Stumpp, M. Thiele, G. Duda, H. Hanken, B. Beck-Broichsitter, O. Jung, N. Kroger, R. Smeets, and M. Heiland, "Improved in vivo osseointegration and degradation behavior of peo surface-modified we43 magnesium plates and screws after 6 and 12 months," *Materials Science and Engineering: C*, vol. 129, 2021.

[117] M. Sadat-Shojai, M. Khorasani, E. Dinpanah-Khoshdargi, and A. Jamshidi, "Synthesis methods for nanosized hydroxyapatite with diverse structures," *Acta Biomaterialia*, vol. 9, pp. 7591–7621, 2013.

[118] A. Pearce, R. Richards, S. Milz, E. Schneider, and S. Pearce, "Animal models for implant biomaterial research in bone: A review," *European Cells and Materials*, vol. 13, pp. 1–10, 2007.

[119] T. Nakashima, T. Hayashi, M: Fukunaga, K. Kurata, M. Oh-Hora, J. Feng, L. Bonewald, T. Kodama, A. Wutz, E. Wagner, J. Penninger, and H. Takayanagi, "Evidence for osteocyte regulation of bone homeostasis through rankl expression," *Nature Medicine*, vol. 17, pp. 1231–1234, 2011.

[120] F. Rauch, "The brains of the bones: how osteocytes use wnt1 to control bone formation," *The Journal of Clinical Investigation*, vol. 127, pp. 2539–2540, 2017.

[121] N. Wittig, M. Laugesen, M. Birkbak, F. Bach-Gansmo, A. Pacureanu, S. Bruns, M. Wendelboe, A. Bruel, H. Sorensen, J. Thomsen, and H. Birkedal, "Canalicular junctions in the osteocyte lacuno-canalicular," *ACS Nano*, vol. 13, pp. 6421–6430, 2019.

[122] L. Bonewald, "The amazing osteocyte," *Jounral of Bone and Mineral Research*, vol. 26, pp. 229–238, 2010.

[123] P. Kollmannsberger, M. Kerschnitzki, F. Repp, W. Wagermaier, R. Winkamer, and P. Fratzl, "The small world of osteocytes: connectomics of the lacuno-canalicular network in bone," *New Journal of Physics*, vol. 19, 2017.

[124] B. Hesse, P. Varga, M. Langer, A. Pacureanu, S. Schrof, N. Mannicke, H. Suhonen, P. Maurer, P. Cloetens, F. Peyrin, and K. Raum, "Canalicular network morphology is the major determinant of the spatial distribution of mass density in human bone tissue: Evidence by means of synchrotron radiation phase-contrast nano-ct," *Journal of Bone and Mineral Research*, vol. 30, pp. 346–356, 2014.

[125] M. Nascimento, "Brief history of x-ray tube patents," *World Patent Information*, vol. 37, pp. 48–53, 2014.

[126] W. Röntgen, "On a new kind of rays," *Nature*, vol. 53, pp. 274–276, 1896.

[127] G. Cervantes, *The basics of x-rays*, pp. 1–5. IOP Publishing LTD, 2016.

[128] F. Zernike, "Diffraction theory of the knife-edge test and its improved form, the phase-contrast method," *Monthly Notices of the Royal Astronomical Society*, vol. 94, pp. 377–384, 1934.

[129] A. Jakhmola, N. Anton, and T. Vandamme, "Inorganic nanoparticles based contrast agents for x-ray computed tomography," *Advanced Healthcare Materials*, vol. 1, pp. 413–431, 2012.

[130] E. Fredenberg, "Spectral and dual-energy x-ray imaging for medical applications," *Nuclear Instruments and Methods in Physics Research Section A: Accelerators, Spectrometers, Detectors and Associated Equipment*, vol. 878, pp. 74–87, 2018.

[131] T. Bashore, "Fundamentals of x-ray imaging and radiation safety.," *Catheterization & Cardiovascular Interventions*, vol. 54, pp. 126–135, 2001.

[132] A. Edwards and A. Lloyd, "Risks from ionising radiation: deterministic effects," *Journal of Radiological Protection*, vol. 18, pp. 175–183, 1998.

[133] B. Wall and D. Hart, "Revised radiation doses for typical x-ray examinations. report on a recent review of doses to patients from medical x-ray examinations in the uk by nrpb. national radiological protection board.," *The British Institute of Radiology*, vol. 70, pp. 437–547, 1997.

[134] A. Chaparian, A. Kanani, and M. Baghbanian, "Reduction of radiation risks in patients undergoing some x-ray examinations by using optimal projections: A monte carlo program-based mathematical calculation," *Journal of Medical Physics*, vol. 39, pp. 32–39, 2014.

[135] J. Als-Nielsen and D. McMorrow, *Elements of Modern X-Ray Physics*. Wiley & Sons, 2011.

[136] B. Zeller-Plumhoff, D. Tolnai, M. Wolff, I. Greving, N. Hort, and R. Willumeit-Rormer, "Utilizing synchrotron radiation for the characterization of biodegradable magnesium alloys—from alloy development to the application as implant material," *Advanced Engineering Materials*, vol. 23, 2021.

[137] M. Langer and F. Peyrin, "3d x-ray ultra-microscopy of bone tissue," *Osteoporosis International*, vol. 27, pp. 441–455, 2015.

[138] S. Flenner, M. Storm, A. Kubec, E. Longo, F. Döring, D. Pelt, C. David, M. Muller, and I. Greving, "Pushing the temporal resolution in absorption and zernike phase contrast nanotomography: enabling fast in situ experiments," *Journal of Synchrotron Radiation*, vol. 27, pp. 1339–1346, 2020.

[139] P. Lauterbur, "Image formation by induced local interactions: examples employing nuclear magnetic resonance," *Nature*, vol. 242, pp. 190–191, 1973.

[140] Y. Lin and A. Koretsky, "Manganese ion enhances t1-weighted mri during brain activation: An approach to direct imaging of brain function," *Magnetic Resonance in Medicine*, vol. 38, pp. 378–388, 2005.

[141] G. Schmidt, M. Reiser, and A. Baur-Melnyk, "Whole-body imaging of the musculoskeletal system: the value of mr imaging," *Skeletal Radiology*, vol. 36, pp. 1109–1119, 2007.

[142] S. Lev and M. Lev, "Imaging of cystic lesions," *Radiologic Clinics of North America*, vol. 38, pp. 1013–1027, 2000.

[143] P. Schaefer, W. Copen, M. Lev, and R. Gonzalez, "Diffusion-weighted imaging in acute stroke," *Magnetic Resonance Imaging Clinics*, vol. 14, pp. 1411–168, 2006.

[144] M. Silva, A. See, W. Essayed, A. Golby, and Y. Tie, "Challenges and techniques for presurgical brain mapping with functional mri," *NeuroImage: Clinical*, vol. 17, pp. 794–803, 2018.

[145] M. Hartung, T. Grist, and C. Francois, "Magnetic resonance angiography: current status and future directions," *Journal of Cardiovascular Magnetic Resonance*, vol. 13, 2011.

[146] T. Huisman and A. Sorensen, "Perfusion-weighted magnetic resonance imaging of the brain: techniques and application in children," *European Radiology*, vol. 14, pp. 59–72, 2003.

[147] N. van Vucht, R. Santiago, B. Lottmann, I. Pressney, D. Harder, A. Sheikh, and A. Saifuddin, "The dixon technique for mri of the bone marrow," *Skeletal Radiology*, vol. 48, p. 186101874, 2019.

[148] D. Griffiths, *Introduction to quantum mechanics*. Upper Saddle River NJ: Pearson Education, 2005.

[149] S. Odaibo, *Quantum Mechanics and the MRI Machine*. Symmetry Seed Books, 2012.

[150] T. Jhamb, V. Rejathalal, and V. Govindan, "A review on image reconstruction through mri," *I.J. Image, Graphics and Signal Processing*, vol. 7, pp. 42–59, 2015.

[151] J. Schneck, "The role of magnetic susceptibility in magnetic resonance imaging: Mri magnetic compatibility of the first and second kinds," *Medical Physics*, vol. 23, pp. 815–850, 1996.

[152] A. Toms, C. Smith-Bateman, P. Malcolm, P. Cahir, and G. M. Cahir, J, "Optimization of metal artefact reduction (mar) sequences for mri of total hip prostheses," *Clinical Radiology*, vol. 65, pp. 447–452, 2010.

[153] M. Reichert, T. Ai, J. Morelli, M. Nittka, U. Attenberger, and V. Runge, "Metal artefact reduction in mri at both 1.5 and 3.0 t using slice encoding for metal artefact correction and view angle tilting," *The British Journal of Radiology*, vol. 88, 2015.

[154] A. Kofler, M. Dewey, T. Schaeffter, C. Wald, and C. Kolbitsch, "Spatio-temporal deep learning-based undersampling artefact reduction for 2d radial cine mri with limited training data," *IEEE Transactions on Medical Imaging*, vol. 39, pp. 703–717, 2020.

[155] L. B. Gutierrez, B. H. Do, G. E. Gold, B. A. Hargreaves, K. M. Koch, P. W. Worters, and K. J. Stevens, "Mri near metallic implants using mavric sl: Initial clinical experience at 3t," *Academic Radiology*, vol. 22, pp. 370–379, 2014.

[156] L. Winter, F. Seifer, L. Zilberti, M. Murbach, and B. Ittermann, "Mri-related heating of implants and devices: a review," *Journal of Magnetic Resonance Imaging*, vol. 53, pp. 1646–1665, 2020.

[157] A. Arduino, U. Zanovello, J. Hand, L. Zilberti, B. Chiampi, and O. Bottauscio, "Heating of hip joint implants in mri: the combined effect of rf and switched-gradient fields," *Magnetic Resonance in Medicine*, vol. 85, pp. 3447–3462, 2021.

[158] L. Winter, E. Oberacker, C. Ozerdem, Y. Ji, F. Knobelsdorff-Brenkenhoff, G. Weidemann, B. Ittermann, F. Seifert, and T. Niendorf, "On the rf heating of coronary stents at 7.0 tesla mri," *Magnetic Resonance in Medicine*, vol. 74, pp. 999–1010, 2015.

[159] K. Baker, J. Tkach, J. Nyenhuis, M. Phillips, F. Shellock, J. Gonzalez-Martinez, and A. Rezai, "Evaluation of specific absorption rate as a dosimeter of mri-related implant heating," *Journal of Magnetic Resonance Imaging*, vol. 20, pp. 315–320, 2004.

[160] Y. Eryaman, B. Akin, and E. Atalar, "Reduction of implant rf heating through modification of transmit coil electric field," *Magnetic Resonance in Medicine*, vol. 65, pp. 1305–1313, 2011.

[161] T. Bachschmidt, M. Kohler, J. Nitsler, C. Geppert, P. Jakob, and M. Nittka, "Polarized multichannel transmit mri to reduce shading near metal implants," *Magnetic Resonance in Medicine*, vol. 75, pp. 217–226, 2016.

[162] M. Dempsey, B. Condon, and D. Handley, "Investigation of the factors responsible for burns during mri," *Jounral of Magnetic Resonance Imaging*, vol. 13, pp. 627–631, 2001.

[163] P. Bian, Z. Xi-yu, R. Liu, H. Li, Q. Zhang, and B. Dai, "Deep-learning-based color doppler ultrasound image feature in the diagnosis of elderly patients with chronic heart failure complicated with sarcopenia," *Journal of Healthcare Engineering*, 2021.

[164] G. Chen, S. Huang, L. Cao, H. Chen, X. Wang, and Y. Lu, "Application of plant phenotype extraction using virtual data with deep learning," *Journal of Physics Conference Series*, 2022.

[165] A. S. Lundervold and A. Lundervold, "An overview of deep learning in medical imaging focusing on mri," *Zeitschrift Für Medizinische Physik*, 2019.

[166] I. Baltuschat, H. Cwieka, D. Kruger, B. Zeller-Plumhoff, F. Schlunzen, R. Willumeit-Romer, J. Moosmann, and P. Heuser, "Scaling the u-net: segmentation of biodegradable bone implants in high-resolution synchrotron radiation microtomograms," *Science Reports*, vol. 11, 2021.

[167] S. Sefa, J. Espiritu, H. Cwieka, I. Greving, S. Flenner, O. Will, S. Beuer, D. Wieland, R. Willumeit-Romer, and B. Zeller-Plumhoff, "Multiscale morphological analysis of bone microarchitecture around mg-10gd implants," *Bioactive Materials*, vol. 30, pp. 154–168, 2023.

Appendix A

List of Abbreviations

AP	Anterior/posterior
ANOVA	Analysis of variance
ASTM	American Society of Testing and Materials
B_0	Main magnetic field
B_1^+	RF field transmission
B_G	Switching magnetic field gradients
BSE	Backscattered electron mode
BV	Bone volume
Ca.TV	Canicular total volume
Ca.TV/BV	Canicular porosity
CFRP	Carbon-fibre reinforced polymers
CJ	Canicular junctions
CJ.N/BV	Canicular junction density
CT	Computed tomography
Cu	Copper
d_{LC}	Distance between a matrix voxel and an LCN voxel
d_{net}	Average distance of a canalicular point to nearest lacunae
DCE	Dynamic contrast-enhanced
DICOM	Digital imaging and communications in medicine
DPBS	Dulbecco's Phosphate Buffered Saline
DX	Digital radiography
E-fields	Electric fields
ECM	Extracellular matrix
ECF	Extracellular fluid
EDX	Energy dispersive X-ray spectroscopy
EM	Electro-magnetic
FOV	Field of view
FPCT	Flat panel computed tomography
GRE	Gradient echo
HF	Head/foot
Lc.N	Number of lacunae found in the sample
Lc.N/BV	Lacunae density
Lc.TV	Total volume of the lacunae
Lc.TV/BV	Lacunar porosity
LCN	Lacuno-canalicular network

LCN.TV	Total volume of the lacuno-canalicular network
LCN.TV/BV	Porosity of the lacuno-canalicular network
LR	Left/right
MDCT	Multidetector computed tomography
ME	Maximum ehnancement
Mg	Magneisum
MRI	Magnetic resonance imaging
MRSA	Methicillin-resistant Staphyloccus aureus
ORTH	Orthogonal
PAR	Parallel
PEO	Plasma electrolytic oxidation
PGLA	Polylactide-co-glycolide
PTM	PGLA/TCP/Mg
RF	Radio frequency
SAG	Sagittal
SAR	Specific absorption rate
SEM	Scanning electron microscopy
TAV	Total artefact volume
TE	Echo time
Ti	Titanium
Tp	Time point
TR	Repetition time
TRA	Transverse
TSE	Turbo spin echo
TXM	Transmission X-ray microscopy
w	Weighted
XRD	X-ray diffraction
β-TCP	β-tricalcium phosphate
μCT	micro-computed tomography

Appendix B

Publications & Conference Presentations

1. **Espiritu J**, Sefa S, Cwieka H, et al. (2023). Detailing the influence of PEO-coated biodegradable Mg-based implants on the lacuno-canalicular network in sheep bone: A pilot study. *Bioactive Materials, Volume 26,* 14-23.

2. **Espiritu J**, Berangi M, Cwieka H, et al. (2023). Radiofrequency induced heating of biodegradable orthopaedic screw implants during magnetic resonance imaging. *Bioactive Materials, Volume 25,* 86-94.

3. Sefa S, **Espiritu J**, Cwieka H, et al. (2023). Multiscale morphological analysis of bone microarchitecture around Mg-10Gd implants. *Bioactive Materials, Volume 30,* 154-168.

4. **Espiritu J**, Berangi M, Cwieka H, et al. (2022). RF-induced heating of biodegradable orthopaedic implants during MRI. *Biodegradable Metals Conference, Alicante, Spain.* Oral Presentation.

5. **Espiritu J**, Berangi M, Yiannakou C, et al. (2022). Evaluating metallic artefact of biodegradable magnesium-based implants in magnetic resonance imaging. *Bioactive Materials, Volume 15,* 382-391.

6. **Espiritu J**, Berangi M, Seitz J-M, et al. (2021). Evaluation of metallic artefact distortions of biodegradable magnesium-based implants in magnetic resonance imaging. *Biodegradable Metals Conference, Alicante, Spain.* Oral Presentation.

7. **Espiritu J**, Berangi M, Seitz J-M, et al. (2021). Evaluation of metallic artefact distortions of biodegradable magnesium-based implants in magnetic resonance imaging. *BBioMedEng21 Conference, Sheffield, United Kingdom.* Oral Presentation.

8. **Espiritu J**, Meier M, Seitz J-M. (2021). The current performance of biodegradable magnesium-based implants in magnetic resonance imaging: A review. *Bioactive Materials, Volume 6 (Issue 12),* 4360-4367.

9. **Espiritu J**, Meier M, Seitz J-M. (2020). The performance of Mg-based implants in MRI: a systematic review. *Biodegradable Metals Conference, Alicante, Spain.* Oral Presentation.

Appendix C

Acknowledgements

Embarking on the journey of a Ph.D. is not unlike navigating uncharted waters, and I am grateful for the support and guidance I have received along this transformative path. The completion of this doctoral journey would not have been possible without the unwavering encouragement and assistance of many individuals and organisations, both near and far. It is with deep gratitude and a sense of profound indebtedness that I extend my heartfelt acknowledgements to those who have been instrumental in shaping this intellectual and personal journey.

First and foremost, I wish to express my sincerest appreciation to Dr. Jan-Marten Seitz from Syntellix AG (Hannover, Germany), who served as my Principal Investigator. Your guidance, stemming from your extensive experience in the industry, has been invaluable. Your belief in the synergy between industry and academia has not only enriched my research but also allowed me the privilege of exploring new cities and countries for work. Additionally, I extend my thanks to Prof. Dr. Regine Willumeit-Römer (Geesthacht, Germany) for providing me with the opportunity to delve into the captivating world of magnesium research. Your mentorship and wealth of knowledge have been pivotal in shaping my academic journey.

I would also like to acknowledge Dr. Katrin Nagel from Syntellix AG, who served as one of my supervisors. Your commitment to supporting my research and your consistent provision of valuable feedback and encouragement have contributed to my success. Moreover, to the rest of the staff at Syntellix AG, your camaraderie and shared laughter have not only lightened the workload but also made my time in Hannover immensely enjoyable.

Through this research endeavour, I had the opportunity to engage in extensive travel to various esteemed institutions, cities, and countries, affording me the privilege of learning from leading experts in the field. Dr. Berit Zeller-Plumhoff from Helmholtz-Zentrum Hereon (Hamburg, Germany), your collaborative spirit challenged me to produce my best scientific work. Your guidance in refining my scientific writing skills has been invaluable. Many thanks go to Dr. Thoralf Niendorf and Dr. Andre Kuhne from MRI.TOOLS (Berlin, Germany). Your support, provision of resources, and expertise in MRI studies have enriched my research immeasurably. Dr. Luca Menichetti from Consiglio Nazionale delle Richerce Pisa (Pisa, Italy), your support, resources, and warm Italian hospitality have made our collaboration a rewarding and enriching experience. To Dr. Martin Meier from Medizinische Hochschule Hannover (Hannover, Germany), thank you for your support and MRI knowledge.

I would like to extend my heartfelt thanks to Christina Yiannakou, Kamila

Iskhakova, Mostafa Berangi, Eduarda Silva, and Hanna Ćwieka for your collaborative efforts in publishing impactful scientific papers. Your dedication to excellence has been inspiring. My gratitude also extends to my colleagues at MgSafe within the ITN framework. Your diverse backgrounds and perspectives have emphasised the importance of international collaboration and have expanded my horizons.

To my friends and family, your support from afar, all the way from Canada while I was in Germany, has been a source of strength and motivation. Your belief in my journey has been a constant reminder of the importance of pursuing one's passions.

In conclusion, this doctoral journey has been a remarkable and rewarding experience, largely due to the contributions and support of the individuals and organisations mentioned above. As I step into the next chapter of my professional life, I carry with me the lessons, friendships, and memories forged during this journey. Each one of you has played a unique role in shaping my academic and personal growth, and for that, I am eternally grateful.

Appendix D

Contribution to Publications

I hereby confirm the contribution to the publications that are part of the dissertation text. The amount of subjectively estimated contribution to the conceptual design, planning, implementation, and preparation of each manuscript is disseminated on the following page.

Place, Date	Researcher Signature
Place, Date	Supervisor Signature

Table of individual contributions to publications mentioned in this dissertation (out of 100%).

Publication title	Conceptual design	Planning	Implement-ation	Manuscript preparation
The current performance of biodegradable magnesium-based implants in magnetic resonance imaging: A review	90%	95%	95%	85%
Detailing the influence of PEO-coated biodegradable Mg-based implants on the lacuno-canalicular network in sheep bone: A pilot study	60%	85%	70%	80%
Evaluating metallic artefact of biodegradable magnesium-based implants in magnetic resonance imaging	80%	85%	75%	85%
Radiofrequency induced heating of biodegradable orthopaedic screw implants during magnetic resonance imaging	85%	85%	80%	85%

Appendix E

Declaration

Hiermit erkläre ich an Eides statt, diese Dissertation eigenständig, d.h. insbesondere selbständig und ohne Hilfe eines kommerziellen Promotionsberaters, angefertigt und keine anderen als die von mir angegebenen Quellen und Hilfsmittel verwendet zu haben. Ich erkläre außerdem, dass die Dissertation weder in gleicher noch in ähnlicher Form bereits in einem anderen Prüfungsverfahren vorgelegen hat und unter Einhaltung der Regeln guter wissenschaftlicher Praxis der Deutschen Forschungsgemeinschaft entstanden ist. Es wurde kein akademischer Grad entzogen.

Ort, Datum	Unterschrift

I hereby confirm that this dissertation is the result of my own work. I did not receive any help or support from commercial consultants. All sources and/or materials applied here are listed and specified in the thesis. Furthermore, I confirm that this thesis has not yet been submitted as part of another examination process, neither in identical nor in similar form, and has been prepared subject to the Rules of Good Scientific Practice of the German Research Foundation. No academic degree has been withdrawn.

Place, Date	Signature